UNIVERSITY OF CALIFORNIA, SAN DIEGO

Phytoplankton in Surface Ocean Fronts: Resolving Biological Dynamics and Spatial Structure

A dissertation submitted in partial satisfaction of the requirements for the degree Doctor of Philosophy

in

Oceanography

by

Alain Joseph de Verneil

Committee in charge:

Professor Peter J.S. Franks, Chair
Professor Jorge Cortés
Professor Michael R. Landry
Professor Mark D. Ohman
Professor Daniel L. Rudnick

2015

The Dissertation of Alain Joseph de Verneil is approved, and it is acceptable in quality and form for publication on microfilm and electronically:

_____

_____

_____

_____

_____

Chair

University of California, San Diego

2015

DEDICATION

To my family, Mama, Papa and Mary-Pat, Christine and Matt, Mamy and Papy, Paul Dano, and Claude duVerlie

TABLE OF CONTENTS

LIST OF FIGURES

ACKNOWLEDGEMENTS

First and foremost, I want to thank my advisor, Peter Franks. I have to admit, I'm extremely lucky to have ended up in his lab at Scripps. Fresh out of college, I had no clue what it meant to be a real scientist, much less a biological oceanographer. The intellectual intensity here at Scripps can be quite daunting, and I wasn't sure how I could make the best use of my talents. This is where, among his many qualities as an advisor, both Peter's patience and experience in dealing with people, come into play. From moments when I thought, "Hey, I should be a virologist!" to those weeks when I'd show up to our meetings with nothing to show for myself, I have to imagine there must have been a good deal of reigning in of exasperation. Even though Peter knew what would be the most natural use of my talents, he encouraged me to find my own dead-ends until, naturally, I ran myself up against an immediate need to find a not-dead-end.

This brings me to our mutual realization that I often find myself working under stressful situations. Whatever anxiety I might experience, and the hours of work that I've put in, I know it was visited tenfold upon Peter. I want to thank you, Peter, for somehow weathering these storms from pre-qualifying up to the last. What's more, the science side of advising is just a part of the care Peter takes in his students. For encouraging all of us in the lab to remain well balanced and sane, and for collecting and encouraging such a wonderful group of people who I'm going to constantly miss, I thank you again.

The work in this thesis, and plenty that is elsewhere or is currently maturing *in cranio*, would not be possible without the support of my committee members. I'd like to thank Mike Landry for taking me on my first research cruise. I got an appreciation for

how hard oceanographers work at sea, how to think on your feet as conditions (and Navy testing grounds) change, and how to piece together a scientific story worth telling. Mike is also an excellent role model for how a Chief Scientist should run a cruise; I don't look forward to my next cruise without him as Chief.

I can't think of anybody who embodies a scientist better than Mark Ohman. Of course, as all great scientists, Mark has a remarkable attention to detail, razor-sharp logical focus, and a way to formulate questions that can drive research into exciting and productive areas. What I truly appreciate, however, is his breadth of interest. In a world where the name of the game is specialization, Mark routinely upholds the mantle of an interdisciplinary perspective, the way any cultivated intellectual should. In addition to all this, he can pepper in some classical references, to boot. Thanks, Mark, for both being an example of a true scientist and helping me start on my path.

I'd like to acknowledge Dan Rudnick, for providing me with both the bedrock skills for the analysis I'll use for the rest of my career, as well as a healthy skepticism. Between taking your class in my first-year that gave me a running start, meeting in your office to find out where I was headed in the wrong direction, and exposing me to the Red Noise paper that made me re-think how to look at a signal, I have you to thank for the quantitative path ahead of me.

Also, I'd like to thank Jorge Cortés. While I'll admit I haven't gotten to know you as well as I'd like, your easy-going nature and positive attitude were a most welcome addition in my endeavor to complete this thesis.

Personal scientific development aside, this thesis would not be possible without my friends and family. Just making it to graduate school is a testament to how both

Mama and Papa have invested in my education and nurtured my interest in the natural world. Without your sacrifices, I wouldn't have the security and ability to pursue academic interests. I hope to do you both proud. Also, whatever I end up contributing in my career, I have my sister to thank. She was the model student and hard worker that set the bar as an older sibling. Any academic achievement has been an indirect result of her efforts, which forced me to do more than I would ever think possible of myself.

At the beginning of these acknowledgements, I mentioned the daunting intellectual intensity here at Scripps. Fortunately, this intensity softened in the warmth of the many wonderful people I've gotten to know here at Scripps. In particular, I must acknowledge the many (all-SIO) roommates I've had over the years: Ashley Corrigan, Diego Melgar, Riley Gannon, Mike DeFlorio, and Angel Ruacho. Having a place to rest my head, laughing in carpools on the way to Scripps, exploring non sequitur conversations about the Austrian School of Economics and Noam Chomsky, and relaxing over good meals: all these wonderful times are thanks to you guys. Included in these good times, of course, are my many friends here in my lab, at Scripps, and in San Diego: Andrew Taylor, Christian Briseño-Avena, Shane Hogle, James Connors, James Fischer, Fanny Chenillat, Stephanie Snyder, Bryce Inman, Jessica Carriere-Garwood, Amanda Netburn, Sam Mascuch, Alan Foreman, Emily Trentacoste, Ethan Deyle, Nick Pizzo, Nick Cavanaugh, Sam Billheimer, Timmy Myers, Val-gal, Megan Bettilyon, John Wokuluk, Liz Vu, Ruth Musgrave, Sam Wilson, Samer Naif, the list goes on… Leaving San Diego will be bittersweet, but I wouldn't trade our time together. Thank you!

Chapter 2, in full, is a reprint of previously published material in Journal of Geophysical Research: Oceans, de Verneil, A., Franks, P.J.S. Copyright (2015) by the

American Geophysical Union, Inc. The dissertation author was the primary investigator and author of this paper.

Chapter 3, in part, is currently being prepared for submission for publication of the material. de Verneil, A., Franks, P.J.S., Ohman, M.D. The dissertation author was the primary investigator and author of this paper.

Chapter 4, in part, is currently being prepared for submission for publication of the material. de Verneil, A., Franks, P.J.S. The dissertation author was the primary investigator and author of this paper.

VITA

2009	Bachelor of Science, Marine Biology, University of Miami
2009	Bachelor of Science, Physics, University of Miami
2009-2010	Regents Fellow, University of California, San Diego
2015	Doctor of Philosophy, Oceanography, University of California, San Diego

PUBLICATIONS

de Verneil, A., Franks, P.J.S., 2015. A pseudo-Lagrangian method for remapping ocean biogeochemical tracer data: Calculation of net Chl-a growth rates. Journal of Geophysical Research: Oceans 120, doi:10.1002/2015JC010898.

de Verneil, A., Franks, P.J.S., Ohman, M.D., 2015. Fine-scale Vertical and Horizontal layers of Salinity and Chlorophyll-a Fluorescence at a Front: Formation by Cross-Frontal Vertical Shear. (For *Geophysical Research Letters*).

de Verneil, A., Franks, P.J.S., 2015. Submesoscale Mixed Layer and Symmetric Instabilities: Physical Dynamics and Biological Responses. (For *Progress in Oceanography*)

ABSTRACT OF THE DISSERTATION

Phytoplankton in Surface Ocean Fronts: Resolving Biological Dynamics and Spatial Structure

by

Alain Joseph de Verneil

Doctor of Philosophy in Oceanography

University of California, San Diego, 2015

Professor Peter J. S. Franks, Chair

Phytoplankton at fronts are subjected to physical forcing at multiple spatiotemporal scales. To better understand why phytoplankton are distributed where they are in a front, and determine whether phytoplankton undergo net growth or decay, my dissertation focuses on characterizing the physical motions at fronts and the rates of change of phytoplankton. To quantify the rate of change of phytoplankton, I developed a "pseudo-Lagrangian" method that tracks biological tracers, allowing the calculation of net specific rates of growth. The method increases the number and spatial coverage of rate estimates relative to traditional methods. I also derived error estimates for these rates.

Applying this method to other tracers will significantly increase the number of rate estimates that can be used, for example, as constraints in biogeochemical budgets.

Using high-resolution hydrographic data from a front, I identified fine-scale features in the phytoplankton distribution. I diagnosed cross-frontal vertical velocity shear as the responsible mechanism. A plausible source for this shear was ageostrophic forcing from frontogenesis upstream. Using remote sensing and scaling arguments, I calculated the timescale of the relevant forcing. This shearing mechanism converts existing horizontal gradients into vertical gradients, with consequences for phytoplankton and for zooplankton grazers. Future phytoplankton studies at fronts will have to consider this mechanism and the structures it produces.

I also surveyed two submesoscale instabilities at fronts, and diagnosed their impacts on phytoplankton communities. The short timescales of the instabilities have precluded field observation until recently, and modeling studies have only recently resolved their dynamics. Exploration of the biological impacts of these specific instabilities via models or observations remains to be conducted. Therefore, by characterizing the motion, prerequisite conditions, and biological impacts of instabilities, I communicated their dynamics to the community of biological oceanographers in order to stimulate research to address this gap in knowledge.

The results from this dissertation can thus be applied in future observational and modeling studies of phytoplankton at fronts: markedly increasing the number of *in situ* growth rate measurements, aiding in the identification of mechanisms structuring phytoplankton distributions, and providing a guide for investigating the rapid changes of phytoplankton within regions of flow instabilities.

Chapter 1.

Introduction

Marine phytoplankton mediate many of the key processes in ocean carbon cycling and biogeochemistry: primary production, new production, inorganic nutrient limitation, and carbon export from the euphotic zone [*Eppley and Peterson*, 1979; *Longhurst*, 1991; *Falkowski*, 1993; *Falkowski et al.*, 2000; *Behrenfeld et al.*, 2006; *Turner*, 2002]. The rate at which phytoplankton communities perform these functions depends upon *in situ* bottom-up (nutrient and light requirements) and top-down (grazing, viral lysing, trophic interactions) forcing [*Tilman et al.*, 1982; *Porter*, 1977; *Calbet and Landry*, 2004].

Phytoplankton are, by definition, unable to swim against prevailing surface currents. As a result, in addition to resolving the complex interactions within marine planktonic ecosystems, biological oceanographers also need to take into account the dynamics of a fluid environment. Pragmatically, investigators usually consider spatiotemporal regimes where either the biological interactions or physical complexity can be studied in isolation.

One important spatiotemporal regime, the submesoscale, unfortunately lies within a range where both physical flows and biological interactions must be taken into account. The relevant timeframe is O(1 day-weeks), a range spanning the generation time of a single phytoplankton cell up to the typical time for a phytoplankton bloom to develop. Submesoscale flows that evolve on this timescale spatially cover regions of O(1-10's km) in the ocean [*Thomas et al.*, 2008; *Lévy et al.*, 2012], much larger than phytoplankton cells but similar in size to plankton patches [*Strass*, 1992; *Abraham*, 1998]. The dominant

surface ocean physical features at the submesoscale are fronts, regions of enhanced horizontal density gradients. Fronts have been known for decades to be regions of locally enhanced biomass and productivity [*Franks*, 1992; *Owen*, 1981; *Olson*, 2002; *Sournia*, 1994; *Powell and Ohman*, 2015]. Therefore, due to the potentially disproportionate importance of fronts in contributing to overall phytoplankton productivity, the physical flows associated with them must be taken into account [*Garçon et al.*, 2001; *Guidi et al.*, 2012; *Denman and Gargett*, 1995; *Oschlies*, 2002].

In this introduction, I provide a brief overview of the mesoscale and submesoscale motions present at fronts relevant for phytoplankton. A hierarchical approach is used in describing these motions, starting with the most slowly evolving flows followed by the fastest. These considerations will motivate the subsequent chapters, which are outlined at the end of this chapter.

1.1. Flows at a Front

Geostrophic Currents

The majority of currents in the ocean exist in an equilibrium state called geostrophic balance [*Niiler et al.*, 2003]. The definition of this balance is between two forces: the horizontal pressure gradient and the Coriolis force. By definition, a surface ocean front has a horizontal density gradient separating less-dense water from denser water. At a given depth, the pressure on the less-dense side is greater than the more-dense side, leading to a horizontal pressure gradient force oriented from the less-dense toward the more-dense side. The non-inertial Coriolis force opposes the horizontal pressure gradient force, resulting in a force balance. The geostrophic contribution to the velocity at

a given depth is perpendicular to these two forces, directed along lines of constant density, or isopycnals. Upon application of the hydrostatic assumption, the horizontal pressure gradient can be transformed into a horizontal density gradient, with a corresponding change in the Coriolis term into a relation for the vertical shear in the horizontal current. In other words, at a given depth the horizontal density gradient produces a perpendicular, along-isopycnal vertical shear contribution to the velocity. If water positioned at a depth below the density gradient is assumed to have low or zero velocity, with corresponding small pressure gradients, a front's density gradient can lead to a surface maximum in velocity magnitude.

A few features of geostrophic currents are important to consider when discussing phytoplankton. First, the geostrophic current itself can transport phytoplankton from far away, and the fact that a front exists between two different water masses with different properties and biogeochemical histories means fronts are regions of enhanced diversity [*Barton et al*., 2010] (Figure 1.1a). The arrangement of geostrophic velocities at the edge of enclosed, coherent vortices such as eddies also contributes to diversity [*d'Ovidio et al.*, 2010; *Bracco et al.*, 2000], providing a source of non-equilibrium biological conditions à la *Hutchinson* [1961]. Additionally, the vertical shear associated with geostrophic currents deforms phytoplankton patches advected along with it, allowing for the creation of layers of enhanced gradients, schematically shown in Figure 1.1b [*Johnston et al.*, 2009]. Enhanced gradient regions are biologically important for processes such as resource competition and predation [*Legendre et al., 1986; Durham and Stocker*, 2012; *Sommer*, 1989; *Huisman et al.*, 1999; *Boucher* et al., 1987].

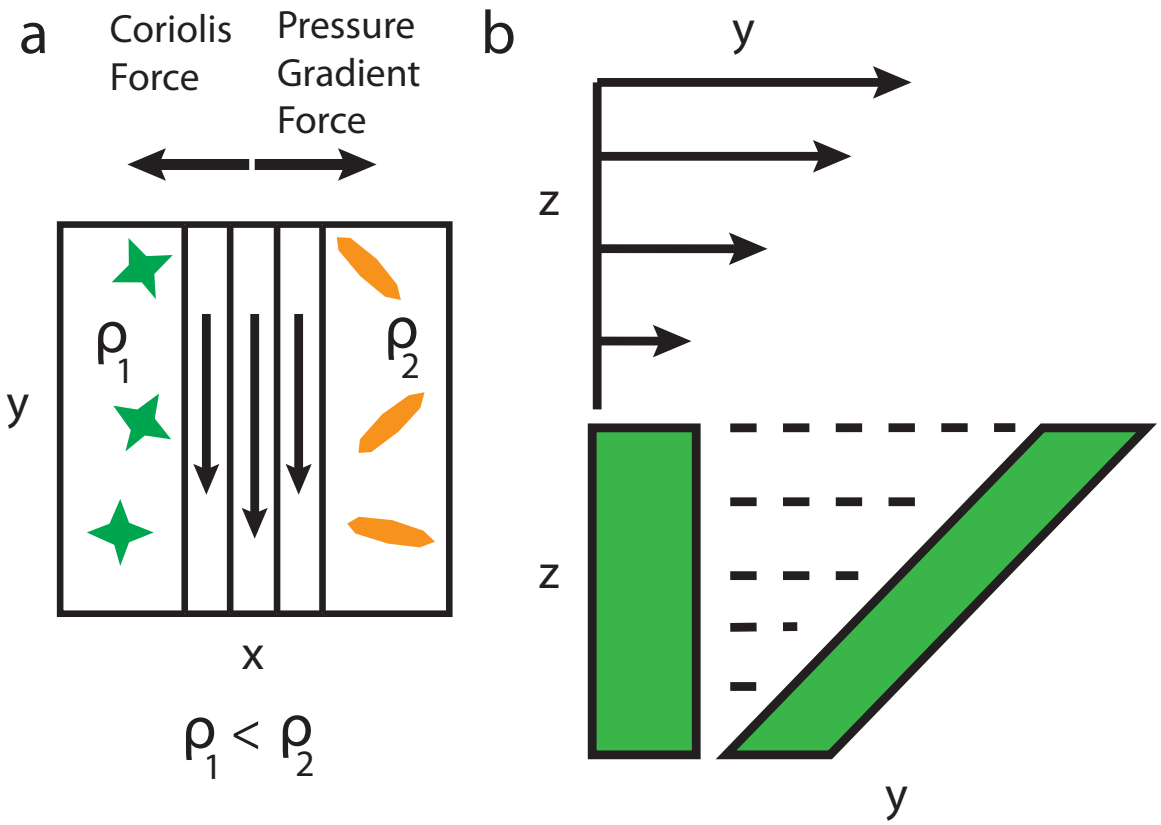

Figure 1.1. (a) A geostrophic flow arises between water masses with two different densities, separating two phytoplankton assemblages. (b) A geostrophic current has a maximum magnitude at the surface, and decreases with depth. This creates shear, which alters the horizontal and vertical distribution of an initially uniform phytoplankton patch.

At fronts, usually the strongest contributor to total velocity will be the geostrophic velocity. While the magnitude of geostrophic currents can vary considerably, at fronts in the ocean, these will typically be on the order of 10's of cm s^{-1}. Since geostrophic currents are stable and persistent, a current of 25 cm s^{-1} can advect water 26 km in a day. Thus, when sampling phytoplankton at a front from a research vessel, one must keep in mind that the same patch of phytoplankton will travel large distances, and efforts must be made in order to continue sampling the same population, such as the quasi-Lagrangian scheme in *Landry et al.* [2009].

Ageostrophic Secondary Circulation (ASC)

Fronts are not generally straight lines in the ocean. As water in fronts traverses large distances, the front may undergo a number of alterations. The two we consider here are an intensification of the front and meanders. When the horizontal density gradient of a front intensifies or deviates from a straight path, it induces an associated horizontal and vertical cross-frontal flow, known as ageostrophic secondary circulations, or ASCs [*Sawyer*, 1956; *Hoskins and Bretherton*, 1972; *Pollard and Regier*, 1992].

Vertical velocities have a strong potential to alter phytoplankton growth. Upward velocities transport phytoplankton closer to the surface, with increased light exposure. Due to the exponential decay of light intensity from the surface with depth, any vertical displacement in depth will have a nonlinear impact upon phytoplankton's light exposure, and subsequent primary productivity. Additionally, since nutrients are largely located below the euphotic zone, any upward motion will tend to bring these limiting chemical species necessary for growth closer to the surface where they can be incorporated into phytoplankton and used for cell growth [*Woods*, 1988; Lévy *et al*., 2001; *Spall and Richards*, 2000]. Thus, upward motion has a doubly positive effect upon phytoplankton growth. Conversely, downward motion has a doubly negative effect on phytoplankton growth. Subduction of phytoplankton, however, can efficiently export carbon out of the surface away from the atmosphere. Both upwelling and subduction processes, and their phytoplankton responses, have been observed in field and modeling studies (Washburn et al., 1991; Strass, 1992; Tintoré et al., 1986; Fielding et al., 2001; Li et al., 2012; Nagai et al., 2008; Thibault et al., 1994; Zakardjian and Prieur, 1998; Oguz et al., 2014;). Since

vertical velocities can have such an important impact upon phytoplankton, it is worthwhile determining where in a front they occur and why.

The vertical velocities for the two case scenarios we will consider can be diagnosed from the quasigeostrophic omega equation [*Hoskins* 1978]:

$$\nabla_h^2(N^2 w) + f^2 \frac{\partial^2 w}{\partial^2 z} = 2\nabla \cdot Q_g \tag{1}$$

where N^2 is the stratification, w the vertical velocity, f the Coriolis parameter, and Q_g the quasigeostrophic Q-vector, defined as

$$Q_g = \frac{g}{\rho_0}\left(\frac{\partial u_g}{\partial x}\frac{\partial \rho}{\partial x} + \frac{\partial v_g}{\partial x}\frac{\partial \rho}{\partial y}, \frac{\partial u_g}{\partial y}\frac{\partial \rho}{\partial x} + \frac{\partial v_g}{\partial y}\frac{\partial \rho}{\partial y}\right) \tag{2}$$

with g being gravitational acceleration, ρ_0 a reference density, ρ density, and u_g, v_g being the horizontal geostrophic currents. Generally speaking, the vertical velocity w is of opposite sign of $\nabla \cdot Q_g$ on the right hand side of (1).

In our first scenario, a front's horizontal density gradient intensifies going down the front along with the geostrophic velocity, which begins to move faster due to the enhanced gradient (Figure 1.2). As the density gradient intensifies, there is positive (negative) $\nabla \cdot Q_g$ on the more (less) dense side of the front, leading to downwelling (upwelling). For continuity of flow, horizontal ageostrophic currents close a circulation cell that is oriented perpendicular to the front (Figure 1.2b). Hence, when a front intensifies, additional velocities are created oriented across the change in density. This is also true of the reverse situation, albeit pointed in different directions, when a density gradient weakens.

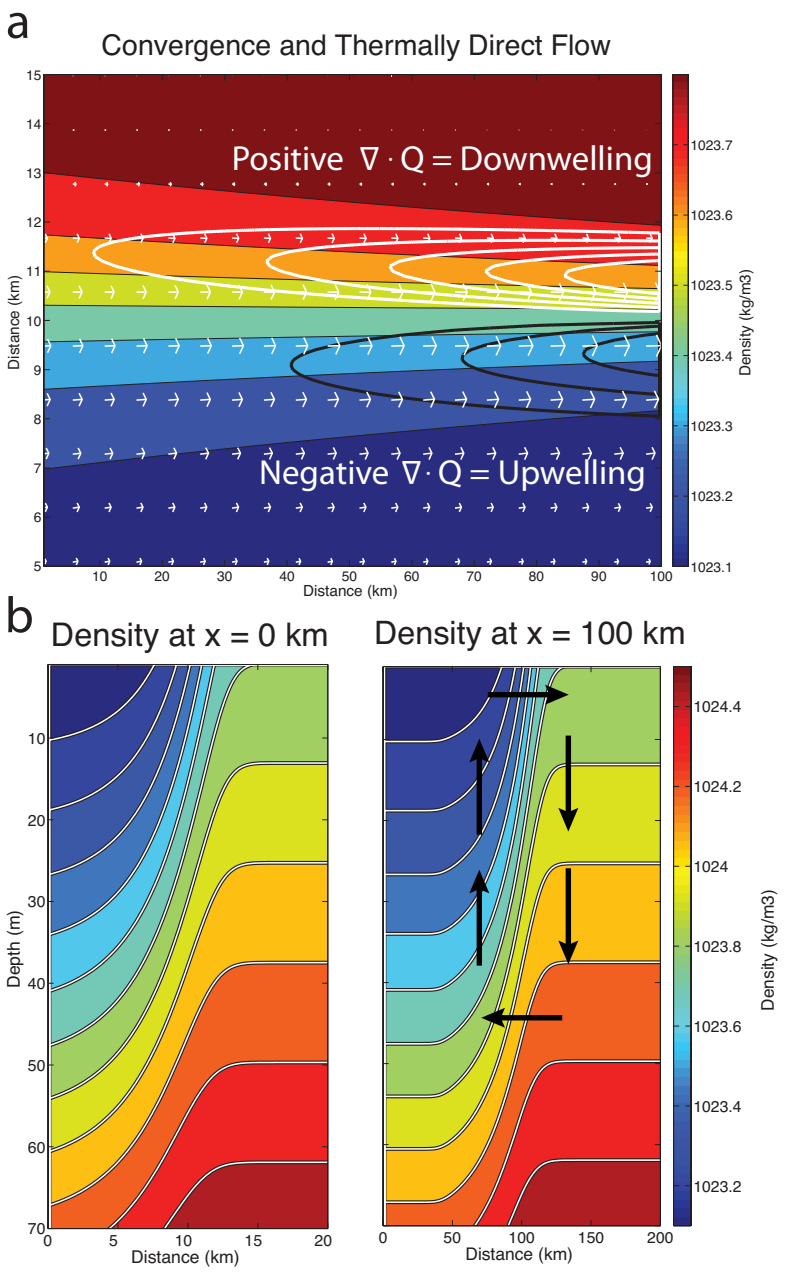

Figure 1.2. (a) Plan view of an intensifying front. Geostrophic currents (white arrows) advect water in the *x* direction. The density gradient sharpens in the *x* direction, causing the geostrophic currents to accelerate. Regions of positive and negative divergence of the Q_g are shown in white and black contours, respectively. (b) Side views of the front at the initial and final *x* positions. The sharpening density gradient induces an ageostrophic secondary circulation (ASC) which downwells (upwells) more (less) dense water. To ensure conservation of mass, horizontal currents complete a circulation cell, advecting less (more) dense water at the surface (at depth) in a positive (negative) *y* direction.

The second scenario, wherein a front meanders, also creates ageostrophic currents perpendicular to the front and creates circulation cells. Since the geostrophic current is largely not accelerating and the horizontal density gradient is not increasing in strength, the terms that dominate $\nabla\cdot Q_g$ can be rewritten using a streamfunction, defined as

$$u_g = -\frac{\partial\psi}{\partial y}, v_g = \frac{\partial\psi}{\partial x} \tag{3}$$

to substitute for the geostrophic velocities, which produces

$$\frac{\rho_0}{g}\nabla\cdot Q_g = -\nabla\rho\times\nabla(\nabla^2\psi). \tag{4}$$

This manipulation is in the same vein as Keyser et al. [1988] and Sanders and Hoskins, [1990], though here we drop terms and do not have the full Q_g vector. The right hand side of (4) states that $\nabla\cdot Q_g$ can be related to the density gradient's vector cross product with the horizontal gradient of $\nabla^2\psi$, otherwise known as relative vorticity, v_x-u_y. As shown in figure 1.3a, the density gradient always points across the front towards the more dense side. Following a front, meandering to the left means a positive vorticity change (cyclonic), and an associated downwelling. Meandering to the right means the opposite: negative vorticity and associated upwelling. Figure 1.3b shows another interesting feature: the maximum vertical velocities are in the regions between the maximum curvature of the meanders, as seen in *Onken* [1992]. For phytoplankton moving along with the front, integrating velocity along the way, it will reach maximal upward displacement at the region of maximum curvature, where $\nabla^2\psi$ is most negative. The particle will similarly be displaced the deepest where $\nabla^2\psi$ is most positive.

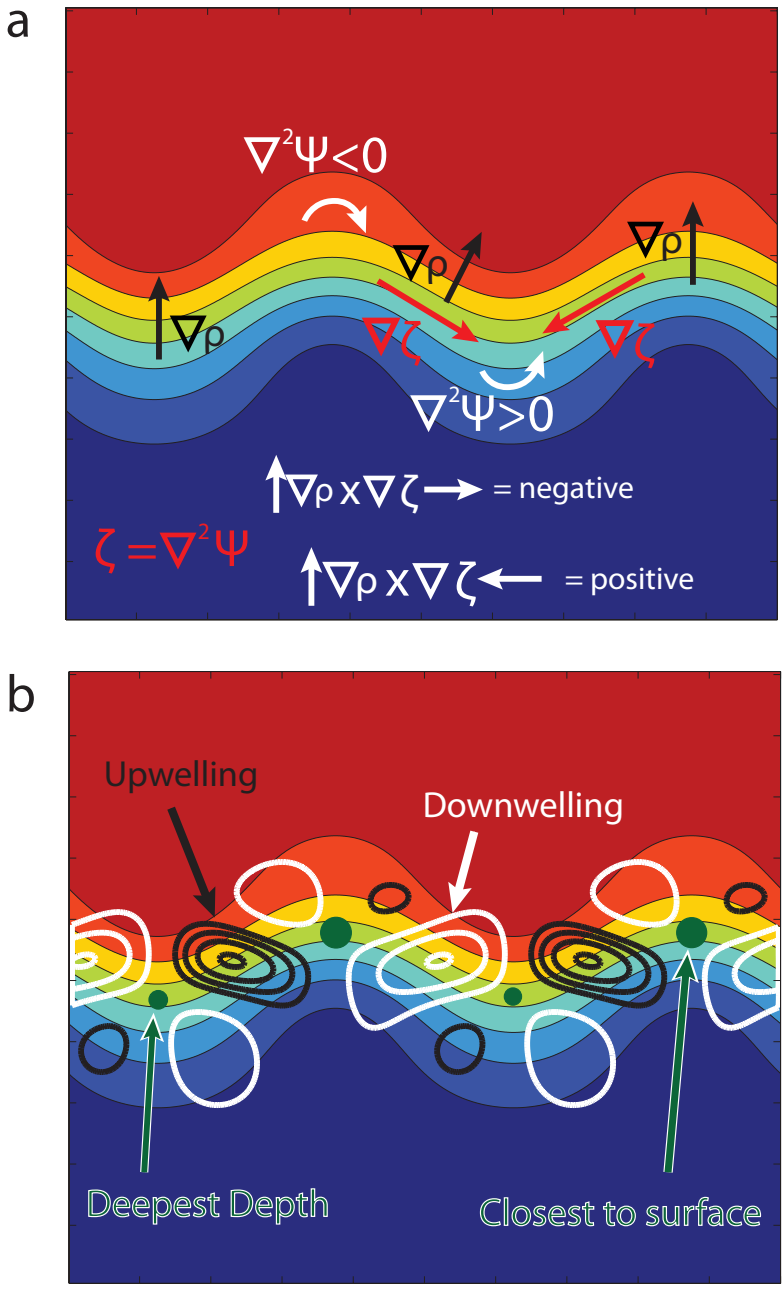

Figure 1.3. Plan views of a meandering front. (a) The horizontal density gradient (black arrows) points to the dense side of the front. Regions of positive and negative $\nabla^2\psi$ are indicated in white. The horizontal gradient of $\nabla^2\psi$ is denoted in red. (b) Regions of downwelling and upwelling, shown in white and black contours, respectively. These regions are located between the meander's maximum excursions. Integrating along a phytoplankton's trajectory in the front, however, shows that the maxima in vertical position end up being at the maximum bend of a meander (green circles).

As a final note, the ageostrophic forcing considered here is ultimately reversible. This is most clearly visible for the meandering case: the motion created by a meander in one direction can be reversed by a meander back. Likewise, if an intensifying front later spread out to its original density gradient, the ageostrophic circulation will reverse. Therefore, the phytoplankton response to ageostrophic forcing will depend upon the magnitude and duration of the vertical displacement.

Instabilities

Instability in a flow field refers to the exponential growth of an initially small perturbation. Because of this exponential growth, instabilities can be some of the fastest-evolving kinds of motion at a front. Typically, the conditions for instability are diagnosed by mathematical analysis of perturbations to linearized equations of motion [*Eady*, 1949; *Charney*, 1947; *Stone*, 1966]. Once instability forms, however, the linear approximations to the equations of motion begin to fail, and explicit numerical modeling is necessary to gauge an instability's temporal evolution. Instabilities grow using energy in the preexisting flow. For fronts, the two main pools of energy available are the potential energy in the horizontal density gradient, and the kinetic energy present in the geostrophic current. Removing energy from either of these energy pools produces similar results: a weakening of the horizontal density gradient and the geostrophic current. Diagnosing the impact of instabilities on phytoplankton, however, requires explicit consideration of the motions involved in each instability and the possible biological scenarios.

1.2. Thesis Outline

Given the diversity of flows possible at surface ocean fronts, consideration of their impact upon phytoplankton requires combining the relevant spatiotemporal scales of motion with those of the endogenous ecological dynamics. Therefore, in my thesis each chapter focuses on a particular aspect of physical circulation at a front and its potential effects on the phytoplankton.

In Chapter 2, I focus on the geostrophic flow of a front. As alluded to previously in this introduction, geostrophic currents can rapidly advect phytoplankton large distances over several days. Normally, advection makes it difficult to sample a phytoplankton population multiple times in order to assess its temporal evolution. However, in this chapter I utilize the fact that the geostrophic current is a large and relatively static velocity field during a hydrographic survey, in order to follow a biological tracer (chlorophyll-*a*) and calculate its rate of change. What is usually considered a disadvantage in these surveys (*i.e.*, its non-synoptic nature) becomes a valuable tool in calculating net rates of change. I also derive a methodology to assess the uncertainty associated with these rate measurements.

In Chapter 3, I turn my attention to the secondary circulation present at a front. Close inspection of hydrographic data taken during a cruise demonstrates small-scale variability – layering – within a front in both an active tracer, salinity, and in chlorophyll-*a* fluorescence. After consideration of the layer characteristics, I show that they must have formed through vertical cross-frontal shear of existing patches. The source of this shear, as demonstrated earlier in the introduction, is forcing of the front due to the Q_g-vector. In most studies, the vertical motion in ASCs is emphasized due to its biological

importance. In this study, I argue that the horizontal motion is also integral to shaping phytoplankton patches, especially in the presence of pre-existing horizontal gradients. Through this mechanism, horizontal gradients at a front become vertical gradients, altering the light exposure of phytoplankton, and impacting the potential prey field for metazoan herbivores migrating into these phytoplankton layers.

Chapter 4 considers the fast-evolving instabilities present at ocean fronts. The literature for this field is growing quickly, but the potential impacts of these motions upon phytoplankton are largely unknown. In this chapter, I consider two submesoscale instabilities at fronts, mixed layer instability (MLI) and symmetric instability (SI). After characterizing their nature and describing the conditions necessary for them to occur, I summarize the relevant motions and hypothesize their impact upon nutrient- and light-limited phytoplankton.

Chapter 5 summarizes the findings from this thesis regarding phytoplankton at surface ocean fronts. It also considers the areas of future research needed in this field.

References

Abraham, E.R., 1998. The generation of plankton patchiness by turbulent stirring. Nature 391 (6667), 577-580.

Barton, A., Dutkiewicz, S., Flierl, G., Bragg, J., Follows, M.J., 2010. Patterns of diversity in marine phytoplankton. Science 327, 1843-1846.

Behrenfeld, M.J., O'Malley, R.T., Siegel, D.A., McClain, C.R., Sarmiento, J.L., Feldman, G.C., Milligran, A.J., Falkowski, P.G., Letelier, R.M., Boss, E.S., 2006. Climate-driven trends in contemporary ocean productivity. Nature 444, 752-755.

Bracco, A., Provenzale, A., Scheuring, I., 2000. Mesoscale vortices and the paradox of the plankton. Proceedings of the Royal Society of London B: Biological Sciences 267 (1454), 1795-1800.

Boucher, J., Ibanez, F., Prieur, L, 1987. Daily and seasonal variations in the spatial distribution of zooplankton populations in relation to the physical structure in the Ligurian Sea Front. Journal of Marine Research 45 (1), 133-173.

Calbet, A., Landry, M.R., 2004. Phytoplankton growth, microzooplankton grazing, and carbon cycling in marine systems. Limnology and Oceanography 49, 51-57.

Charney, J.G., 1947. The dynamics of long waves in a baroclinic westerly current. Journal of Meteorology 4 (5), 136-162.

Denman, K.L., Gargett, A.E., 1995. Biological-physical interaction in the upper ocean: the role of vertical and small scale transport processes. Annual Reviews in Fluid Mechanics 27, 225-55.

D'Ovidio, F., De Monte, S., Alvain, S., Dandonneau, Y., Lévy, M., 2010. Fluid dynamical niches of phytoplankton types. Proceedings of the National Academy of Sciences 107 (43), 18366-18370, doi: 10.1073/pnas.1004620107.

Durham, W.M., Stocker, R., 2012. Thin plankton layers: Characteristics, mechanisms, and consequences. Annual Review of Marine Science 4, 177-207.

Eady, E.T., 1949. Long waves and Cyclonne Waves. Tellus 1, 33-52.

Eppley, R.W., Peterson, B.J., 1979. Particulate organic matter flux and planktonic new production in the deep ocean. Nature 282, 677-680.

Falkowski, P.G., 1993. The role of phytoplankton photosynthesis in global biogeochemical cycles. Photosynthesis Research, 39, 235-258.

Falkowski, P.G., Scholes, R.J., Boyle, E., Candall, J., Canfield, D., Elser, J., Gruber, N., Hibbard, K., Hogberg, P., Linder, S., Mackenzie, F.T., Morre III, B., Pedersen, T., Rosenthall, Y., Seitzinger, S., Smetacek, V., Steffan, W., 2000. The global carbon cycle: a test of our knowledge of earth as a system. Science 290, 235-258.

Fielding, S., Crisp, N., Allen, J.T., Hartman, M.C, Rabe, B., Roe, H.S.J., 2001. Mesoscale subduction at the Almeria-Oran front Part 2. Biophysical interactions. Journal of Marine Systems 30, 287-304.

Franks, P.J.S., 1992. Phytoplankton blooms at fronts: patterns, scales, and physical forcing mechanisms. Reviews in Aquatic Sciences 6 (2), 121-137.

Garçon, V.C., Oschlies, A., Doney, S.C., McGillicuddy, D., Waniek, J., 2001. The role of mesoscale variability on plankton dynamics in the North Atlantic. Deep-Sea Research II 48, 2199-2226.

Guidi, L., Calil, P.H.R., Duhamel, S., Björkman, K.M., Doney, S.C., Jackson, G.A., Li, B., Church, M.J., Tozzi, S., Kolber, Z.S., Richard, K.J., Fong, A.A., Letelier, R.M., Gorsky, G., Stemmann, L., Karl, D.M., 2012. Does eddy-eddy interaction control surface phytoplankton distribution and carbon export in the North Pacific Subtropical Gyre? Journal of Geophysical Research: Biogeoscience 117, G2.

Hoskins, B.J., Bretherton, F.P., 1972. Atmospheric frontogenesis models: Mathematical formulation and solution. Journal of Atmospheric Science 29, 11-37.

Hoskins, B.J., Draghici, I., Davies, H.C., 1978. A new look at the ω-equation. Quarterly Journal of the Royal Meteorological Society 104, 31-38.

Huisman, J., Jonker, R.R., Zonneveld, C., Weissing, F.J., 1999. Competition for light between phytoplankton species: experimental tests of mechanistic theory. Ecology 80 (1), 211-222.

Hutchinson, G.E., 1961. The paradox of the plankton. American Naturalist, 137-145.

Johnston, T.S., Cheriton, O.M., Pennington, J.T., Chavez, F.P., 2009. Thin phytoplankton layer formation at eddies, filaments, and fronts in a coastal upwelling zone. Deep Sea Research II 56 (3), 246-259.

Keyser, D., Reeder, M.J., Reed, R.J., 1988. A generalization of Petterssen's Frontogenesis Function and its relation to the forcing of vertical motion. Monthly Weather Review 116, 762-780.

Landry, M.R., Ohman, M.D., Goericke, R., Stukel, M.R., Tsyrklevich, K., 2009. Lagrangian studies of phytoplankton growth and grazing relationships in a coastal upwelling ecosystem off southern California. Progress in Oceanography 83, 208-216.

Legendre, L., Demers, S., Lefaivre, D., 1986. Biological production at marine ergoclines. Elsevier oceanography series 42, 1-29.

Lévy, M., Klein, P., Tréguier, A.M., 2001. Impact of sub-mesoscale physics on production and subduction of phytoplankton in an oligotrophic regime. Journal of Marine Research 59, 535-565.

Lévy, M., Ferrari, R., Franks, P.J.S., Martin, A.P., Rivière, P., 2012. Bringing physics to life at the submesoscale. Geophysical Research Letters 39.

Li, Q.P., Franks, P.J.S., Ohman, M.D., Landry, M.R., 2012. Enhanced nitrate fluxes and biological processes at a frontal zone in the southern California current system. Journal of Plankton Research 34, 790-801.

Longhurst, A.R., 1991. Role of the marine biosphere in the global carbon cycle. Limnology and Oceanography 36, 1507-1526.

Nagai, T., Tandon, A., Gruber, N., McWilliams, J.C., 2008. Biological and physical impacts of ageostrophic frontal circulations driven by confluent flow and vertical mixing. Dynamics of Atmospheres and Oceans 45 (3-4), 229-251.

Niiler, P.P., Maximenko, N.A., McWilliams, J.C., 2003. Dynamically balanced absolute sea level of the global ocean derived from near-surface velocity observations. Geophysical Research Letters 30(22), 2164, doi:10.1029/2003GL018628

Oguz, T., Macias, D., Garcia-Lafuente, J., Pascual, A., Tintoré, J., 2014. Fueling Plankton production by a meandering frontal jet: A case study for the Alboran Sea (Western Mediterranean). PLoS ONE 9 (11): e111482.

Olson, D.B., 2002. Biophysical dynamics of ocean fronts. Pages 187-218, in Robinson, A.R., et al. (eds). Biological-physical interactions in the sea (The Sea, 12). John Wiley and Son, New York. ISBN: 9780674017429

Onken, R., 1992. Mesoscale upwelling and density finestructure in the seasonal thermocline – A dynamical model. Journal of Physical Oceanography 22 (11), 1257-1273.

Oschlies, A., 2002. Can eddies make ocean deserts bloom? Global Biogeochemical Cycles 16 (4), 53-1.

Owen, R.W., 1981. Fronts and eddies in the sea: mechanisms, interactions and biological effects. Analysis of marine ecosystems, 197-233.

Pollard, R.T., Regier, L.A., 1992. Vorticity and vertical circulation at an ocean front. Journal of Physical Oceanography 22, 609-625.

Porter, K.G., 1977. The Plant-Animal interface in Freshwater Ecosystems: Microscopic grazers feed differentially on planktonic algage and can influence their community structure and succession in ways that are analogous to the effects of herbivores on terrestrial plant communities. American Scientist, 159-170.

Powell, J.R., Ohman, M.D., 2015. Covariability of zooplankton gradients with glider-detected density fronts in the Southern California Current System. Deep-Sea Research II 112, 79-90.

Sanders, F., Hoskins, B.J., 1990. An easy method for estimation of Q-vectors from weather maps. Weather and Forecasting 5 (2), 346-353.

Sawyer, J.S., 1956. The vertical circulation at meteorological fronts and its relation to frontogenesis. Proceedings of the Royal Society of London A: Mathematical, physical and engineering sciences 234 (1198), 346-362.

Sournia, A., 1994. Pelagic biogeography and fronts. Progress in Oceanography 34(2), 109-120, doi: 10.1016/0079-6611(94)90004-3

Spall, S.A., Richards, K.J., 2000. A numerical model of mesoscale frontal instabilities and plankton dynamics – I. Model formulation and initial experiments. Deep Sea Research Part I: Oceanographic Research Papers 47(7), 1261-1301, doi: 10.1016/S0967-0637(99)00081-3

Stone, P.H., 1966. On non-geostrophic baroclinic stability. Journal of the Atmospheric Sciences 23(4), 390-400, doi: 10.1175/1520-0469(1966)023<0390:ONGBS>2.0.CO;2

Strass, V.H., 1992. Chlorophyll patchiness caused by mesoscale upwelling at fronts. Deep-Sea Research 39 (1), 77-96.

Sommer, U., 1989. The role of competition for resources in phytoplankton succession. Pages 57-106. In Plankton ecology. Springer Berlin Heidelberg.

Thibault, D., Gaudy, R., Le Fèvre, J., 1994. Zooplankton biomass, feeding and metabolism in a geostrophic frontal area (Almeria-Oran Front, western Mediterranean). Significance to pelagic food webs. Journal of Marine Systems 5 (3), 297-311.

Thomas, L.N., Tandon, A., Mahadevan, A., 2008. Submesoscale processes and dynamics. In Ocean Modeling in an Eddying Regime. Geophysical Monograph Series 177, 17-38.

Tilman, D., Kilham, S.S., Kilham, P., 1982. Phytoplankton community ecology: the role of limiting nutrients. Ann. Rev. Ecol. Syst. 13, 349-372.

Tintoré, J., La Violette, P.E., Blade, I., Cruzado, A., 1988. A Study of an Intense Density Front in the Eastern Alboran Sea: The Almeria-Oran Front. Journal of Physical Oceanography 18, 1384-1397.

Turner, J.T., 2002. Zooplankton fecal pellets, marine snow and sinking phytoplankton blooms. Aquatic Microbial Ecology 27, 57-102.

Washburn, L., Kadko, D.C., Jones, B.H., Hayward, T., Kosro, P.M., Stanton, T.P., Ramp, S., Cowles, T., 1991. Water mass subduction and the transport of phytoplankton in a coastal upwelling system. Journal of Geophysical Research 97, 14,927-14,945.

Woods, J., 1988. Scale upwelling and primary production. In Toward a Theory on biological-physical interactions in the world ocean, 7-38. Springer, Netherlands.

Zakardjian, B., Prieur, L, 1998. Biological and chemical signs of upward motions in permanent geostrophic fronts of the Western Meidterranean. Journal of Geophysical Research: Oceans 103 (C12) 27849-27866.

Chapter 2.

A pseudo-Lagrangian method for remapping ocean biogeochemical tracer data: calculation of net Chl-a growth rates.

Abstract

A key goal in understanding the ocean's biogeochemical state is estimation of rates of change of critical tracers, particularly components of the planktonic ecosystem. Unfortunately, because ship survey data are not synoptic, it is difficult to obtain spatially resolved estimates of the rates of change of tracers sampled in a moving fluid. Here we present a pseudo-Lagrangian transformation to re-map data from underway surveys to a pseudo-synoptic view. The method utilizes geostrophic velocities to back-advect and relocate sampling positions, removing advection aliasing. This algorithm produces a map of true relative sampling locations, and allows for determination of the relative locations of observations acquired along streamlines, as well as a corrected view of the tracer's spatial gradients. We then use a forward advection scheme to estimate the tracer's relative change along streamlines, and use these to calculate spatially resolved, net specific rates of change. Application of this technique to chlorophyll-*a* (Chl-*a*) fluorescence data around an ocean front is presented. We obtain 156 individual estimates of Chl-*a* fluorescence net specific rate of change, covering ~1200 km^2. After incorporating a diffusion-like model to estimate error, the method shows the majority of observations (64%) were significantly negative. This pseudo-Lagrangian approach generates more accurate spatial maps than raw survey data, and allows spatially resolved

estimates of net rates of tracer change. Such estimates can be used as a rate budget constraint that, in conjunction with standard rate measurements, will better determine biogeochemical fluxes.

2.1. Introduction

The concentrations of biogeochemical properties in the ocean emerge from an ever-changing balance of the local rates of production and loss. For example, phytoplankton concentration is controlled by its growth rate, which is a function of nutrients and light, and loss rates, which include such processes as grazing, viral lysis, and natural mortality. In addition to these physiological and trophic rates, local phytoplankton concentrations are affected by dynamics such as sinking and active swimming. Unfortunately, all these rates are difficult to measure. Furthermore, these dynamics all occur within the context of a moving medium, making the study of planktonic ecosystems and associated biogeochemical fluxes a discipline that must necessarily resolve complex biological interactions within physical flows.

A general equation to describe the time evolution of concentration C of a biogeochemical property at a fixed location is:

$$\frac{\partial C}{\partial t} + \mathbf{u} \cdot \nabla C = Diffusion + Swimming + Sources - Sinks \qquad (1)$$

The advection term $\mathbf{u} \cdot \nabla C$ on the left hand side (LHS) of (1) appears as a result of taking the full time derivative of C: in a fixed, Eulerian coordinate frame, the quantity C and its spatial gradients move with the flow. If one transforms to a Lagrangian frame that moves

with the flow, the advection term disappears since water velocity relative to the coordinate is now zero:

$$\frac{dC}{dt} = Diffusion + Swimming + Sources - Sinks \qquad (2)$$

Transforming to a Lagrangian frame (2) therefore simplifies (1) by removing the effects of advection on the LHS, leaving *in situ* biological rates, diffusion, and swimming on the right hand side (RHS) to determine the local rate of change of concentration (note now that the partial derivative of *C* has become full in eqn. 2). Many studies make use of this fact in their sampling strategy: they measure both rates and tracer concentrations in particular water masses by following drifters or adding conservative inert tracers [e.g., *Wilkerson and Dugdale*, 1987; *Abbott et al.*, 1990; *Law et al.*, 1998 and all FeAX's noted in *Boyd et al.*, 2007; *Li et al.*, 2008; *Jickells et al.*, 2008; *Landry et al.*, 2009]. Indeed, various algorithms, tools, and software have been developed to optimize a ship's ability to follow a water mass during biogeochemical experiments [*Dogliogli et al.*, 2013 and references within]. However, most biological rate measurements in the ocean are difficult to obtain, often coming from isolated observations that are necessarily extrapolated to be representative of dynamics within larger scale features.

Here we present a "pseudo-Lagrangian" data analysis technique that transforms underway survey data from an Eulerian to a Lagrangian frame, allowing for explicit quantification of the RHS of (1), and thus calculation of *in situ* net rates of tracer concentration change. The approach begins with the construction of a spatial map of the Eulerian velocity field in the survey region. Then, we find multiple streamlines of the Eulerian flow that allow us to remove the effects of advection along these trajectories.

We use these trajectories with measured tracer concentrations of (in this case) chlorophyll-*a* (Chl-*a*) fluorescence to create a Lagrangian field by back-advecting the tracer along the trajectories, similar to reverse domain filling techniques [*Dragani et al.*, 2002; *Methven et al.*, 2003]. We then analyze this Lagrangian field to quantify the net rates of change due to the RHS of (1). Creating Lagrangian trajectories from Eulerian data is not a novel concept: similar approaches have been applied to create better estimates of atmospheric tracer fields and modeling of rates [*Sutton et al.*, 1994; *Nilsson and Leck*, 2002; *Dragani et al.*, 2002; *Taylor*, 1992; *Bowman et al.*, 2013], and many ocean studies analyze Lagrangian trajectories derived from Eulerian output of satellite data or ocean models [*Blanke and Raynaud*, 1997; *d'Ovidio et al.*, 2004; *Doglioli et al.*, 2006; *Lehahn et al.* 2007; *Lett et al.* 2008; *d'Ovidio et al.*, 2010]. Indeed, SeaSoar data similar to ours have been advected using a comparable methodology to this study, but with the objective of evaluating sampling biases of dynamical variables [*Allen et al.*, 2001; *Rixen et al.*, 2001; *Rixen et al.*, 2003]. However, limited physical datasets and the general difficulty of measuring biological tracers have precluded application of this technique to the evolution of actual *in situ* tracer data in the ocean (though for a satellite-derived estimation of phytoplankton net growth rate, see *Abbott and Zion* [1985]). Our method is not truly Lagrangian because there are details of the flow that are not resolved at small scales, and its applicability relies upon the presence of a dominant, stationary velocity field. The term "pseudo-Lagrangian" is chosen to reflect use of *in situ* data in calculating rates, similar to *Nilsson and Leck* [2002], though it should not be confused with the "pseudo-Lagrangian" data assimilation technique [*Molcard et al.* 2003].

Lagrangian drifters designed to follow water masses typically only approximate Lagrangian measurements, and must factor in "slippage" (though see *D'Asaro* [2003] and *D'Asaro et al.* [2011]). Still, floats and drifters with telemetry have become relatively inexpensive for physical Lagrangian studies, allowing for synoptic coverage over large spatial regions. These studies, over multiple deployments, have yielded estimates of flow structure and other physical quantities of interest, and have created an entire field of Lagrangian statistics (see *LaCasce* [2008] for a recent review). By contrast, the instruments and techniques for measuring biological variables usually require more intense and continued effort, limiting both the spatial and temporal scales at which these observations are made. Without an environmental context, many biological data are collected in a relative vacuum, creating problems for the analysis of the dynamics underlying patchiness of plankton communities and their associated biogeochemical fluxes [*Powell and Okubo*, 1994; *Martin* 2003; *Bracco et al.,* 2000; *Kozalska et al.*, 2007]. With the pseudo-Lagrangian approach, we hope to begin to address this contextual issue in field data.

In this study, we develop the pseudo-Lagrangian methodology within the context of an ocean front. We diagnose the physical flow field from underway SeaSoar vertical profiles and acoustic Doppler current profiler (ADCP) currents, outlined in section 2. Then, with use of an Eulerian-Lagrangian coordinate transformation in section 3, we create a pseudo-Lagrangian tracer field using Chl-*a* fluorescence. In section 4, we describe how the tracer field can be used to estimate large-scale, spatially resolved rates, which would be difficult to obtain in any other way. Section 5 discusses the results and

conclusions of this rate application, and section 6 concludes with suggestions of future uses of this approach.

2.2. Data

2.2.1 Sampling plan and context

Data for this study derive from the 2012 process cruise (P1208), dubbed "E-Front", of the NSF-funded California Current Ecosystem (CCE) Long Term Ecological Research (LTER) program conducted from July to August 2012 aboard *R/V Melville*. The purpose of the cruise was to identify regions of enhanced horizontal physical and biological gradients (i.e., fronts) and quantify their role in the pelagic ecosystems of the CCE. The study region spans a roughly rectangular area with (123.8° W, 33.5° N) and (121.5° W, 35° N) delineating diagonal corners. As indicated by Aviso satellite sea level anomaly data (Figure 2.1), a frontal region existed in the vicinity of two mesoscale features: cyclonic to the southeast, and anticyclonic to the west. The altimeter products were produced by Ssalto/Duacs and distributed by Aviso, with support from CNES (http://www.aviso.altimetry.fr/duacs/). At the onset of the cruise, E-Front's hydrographic structure was surveyed in a radiator pattern by SeaSoar from 30 July to 3 August going south to north, moving upstream relative to the geostrophic jet. Subsequent to this survey, biological measurements and process experiments were conducted at various locations in relation to the frontal region (similar to Landry et al. [2009]). After these biological measurements, another SeaSoar survey was performed from 21 August to 25 August moving downstream relative to the geostrophic jet to ascertain the final position of the feature.

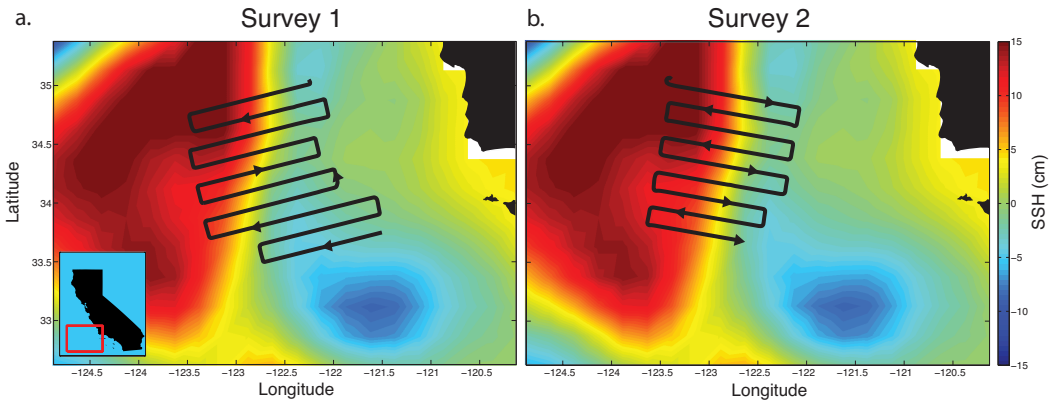

Figure 2.1. E-front. Aviso Sea surface height anomaly average for (a) Survey 1 (July 29-August 3) and (b) Survey 2 (August 21-25, 2012). Black line shows the location and direction of the survey relative to the frontal feature.

2.2.2 SeaSoar and Alf-A Data

During both hydrographic surveys, the SeaSoar conducted profiles in a tow-yo fashion. Data were acquired by two onboard SeaBird SBE-9Plus CTDs (Sea-Bird Electronics, www.seabird.com), a Seapoint SCF Chl-*a* fluorometer (Seapoint Sensors, Inc., www.seapoint.com), Wet Labs C-Star transmissometer (Western Environmental Technologies, www.wetlabs.com), and Rinko-III oxygen sensor (Rockland Oceanographic Services, Inc., www.rocklandocean.com). All data were sampled at 24 Hz. Temperature and conductivity data were lag-corrected to minimize salinity spiking, though thermal inertia lag [*Lueck and Picklo*, 1990] was ignored due to the flushing rate of the SeaSoar (see *Rudnick and Luyten* [1996]). These data were then averaged into a 1 Hz time series, followed by a 6 m resolution vertical binning to give single up- and down-casts, approximately 8 minutes apart with ~2 km horizontal displacement. Density data were then constrained to obey static stability [*Rudnick*, 1996] using a constrained

linear least squares algorithm (MATLAB and Optimization Toolbox Release 2012a, The Mathworks, Inc., Natick, Massachusetts, United States).

SeaSoar-derived Chl-*a* fluorescence measurements were matched with surface measurements concurrently from an Advanced Laser Fluorometer (ALF-A) developed by A. Chekalyuk (Lamont Doherty Earth Observatory, www.ldeo.columbia.edu). The ALF-A measures laser-stimulated excitation (LSE) of fluorescence at multiple wavelengths in flow-through sampling [*Chekalyuk and Hafez*, 2008]. Data collected during E-Front were compared with and calibrated by *in situ* chlorophyll-*a* extractions. The correlation between SeaSoar fluorescence and ALF-A chlorophyll-*a* is high, with a linear relationship explaining 98% of the variance in nighttime measurements and 95% overall. In general, the ratio of fluorescence to chlorophyll-*a* is not constant. However, after accounting for non-photochemical quenching, the skill in predicting chlorophyll-*a* improves [*Chekalyuk and Hafez,* 2011]. Based on the ALF-A data, the largest non-photochemical quenching (NPQ) effect at the surface amounted to at most 23% of the surface signal, and presumably decreased exponentially with depth [*Krause and Weis*, 1991; *Müller et al.*, 2001]. This NPQ effect was found to be a minor contribution to the variability in the Chl-*a* and rate estimates used later, so the estimate of Chl-*a* is reliable (Section 4). Weak NPQ is not surprising, as satellite coverage during E-Front suffered from strong cloud cover, indicative of reduced overall insolation. Thus, variability in the fluorescence-derived Chl-*a* due to NPQ has been ignored in this study.

2.2.3 ADCP currents

Vertical profiles of horizontal velocity were obtained from the shipboard-mounted 75 kHz Ocean Surveyor ADCP on the *R/V Melville*. The UHDAS pre-processed data were averaged into 15 minute ensembles with a 16 m vertical bin resolution [*Firing and Hummon*, 2010]. Subsequently, the angle of misalignment was re-calculated from the total measured and ship velocities in a linear variance minimization scheme to provide estimates of the water velocities [*Rudnick and Luyten*, 1996].

2.2.4 Objective maps

Density, Chl-*a*, and ADCP currents were objectively mapped onto matching horizontal grids at specific depths using the methodology of *Le Traon* [1990]. The signal distribution was assumed Gaussian, with correlation length scales determined from the observed autocovariance calculated from binned data. These lengths are 25, 55, 25, 15 km in x and 45, 25, 55, 30 km in y directions for density, ADCP u velocity, ADCP v velocity, and Chl-*a* fluorescence, respectively. In determining error, a noise-to-signal ratio of ≤ 0.05 is assumed, and all values used in subsequent calculations were restricted to an error threshold of 0.1 [*Rudnick and Luyten*, 1996]. Objective fits for density assume a planar mean and a single valued mean for currents, in concordance with geostrophy. Chl-*a* fluorescence was not assumed to conform to any particular functional form and by default is assigned a single mean value (Figure 2.2). The objective map grids have a resolution of ~4 km on each side, to reduce over-interpolation between adjacent sampling locations, and to include sufficient resolution between survey lines.

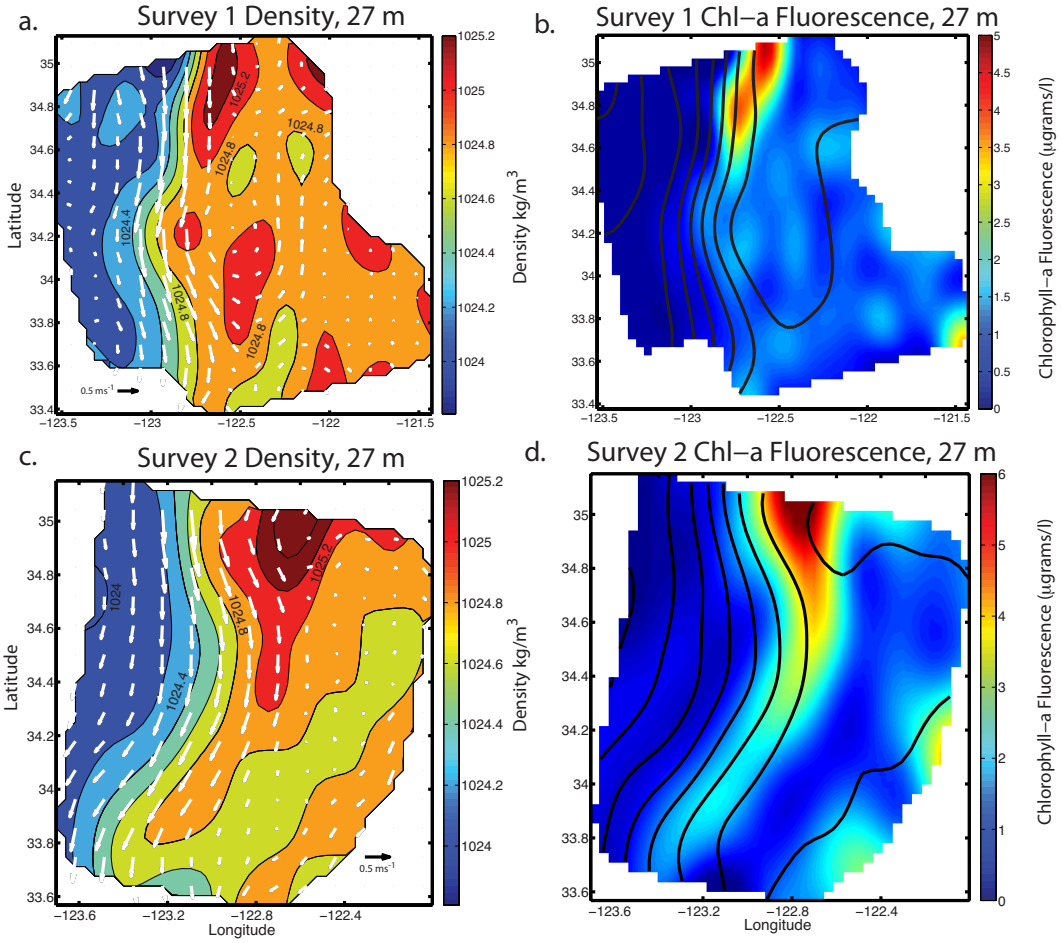

Figure 2.2. Objective maps of Density (a,c) and chlorophyll-*a* fluorescence (b,d) for Surveys 1 and 2, at 27 m depth. White arrows in (a,c) indicate the horizontal currents, displayed at one-fourth resolution. Black contours in (b,d) show the streamlines of the flow. Note the strong, stationary frontal feature in both density and Chl-*a*.

2.2.5 Geostrophic currents

All velocity fields used in this study are geostrophic currents fit to the objectively mapped density and ADCP data through a L_2 norm misfit minimization scheme. After application of a static stability criterion to the three-dimensional density field, geostrophic currents are found via a relaxation method [*Rudnick*, 1996] solving:

$$\nabla^2\psi = H^{-1}(\nabla^2 R + \zeta) \qquad (3)$$

where ψ is the streamfunction, a depth-integrated scalar for the water volume under consideration. H is defined by

$$H = \int_{z_1}^{z_2} w_u dz \tag{4}$$

where w_u is a weighting parameter reflecting confidence in the velocity observation, and is here kept equal to one, essentially making H the depth. R is the quantity

$$R = \frac{g}{f\rho_0} \int_{z_0}^{z} \rho dz \tag{5}$$

Finally, ζ is the relative vorticity found from the ADCP objective map. All these quantities are depth-integrated from the shallowest ADCP depth at 27 m to a 300 m reference level. Geostrophic velocities are found from the relations

$$u_g = -\frac{\partial \psi}{\partial y} + \frac{\partial R}{\partial y} \tag{6}$$

$$v_g = \frac{\partial \psi}{\partial x} - \frac{\partial R}{\partial x} \tag{7}$$

The geostrophic currents account for the majority of the variance in the objectively fit ADCP currents, with a vector complex correlation of 0.84 (Figure 2.2). As noted in *Rudnick* [1996], the vertical velocity shear, and not the geostrophic current, is constrained to be isopycnal; even so, the geostrophic current largely follows isopycnals.

Following *Viúdez et al.* [2000], we can determine the relative error in our currents as the divergent portion of the ADCP objective map, reflecting aliased phenomena not removed by objective analysis. After solving for these components via a similar relaxation method, we arrive at a divergent velocity error distribution that is approximately log-normal, similar to theory and observations of turbulent motion in the ocean [*Kolmogorov*, 1962; *Gurvich and Yaglom*, 1967; *Yamazaki and Lueck*, 1990]. As

might be expected [*Pallas-Sanz et al.*, 2010], introducing these errors randomly into (3) produces little change in the streamfunction. The resulting displacements lead to equivalent eddy diffusivities of O(1-10) $m^2 s^{-1}$, which are an order of magnitude lower than the "diffusivity" used for error in Section 4. We thus forego including variance of the advective geostrophic velocity field for this analysis.

Given that this study was conducted around a front, we chose the balanced geostrophic currents as the leading order contribution to the dynamics of the flow field. We could include ageostrophic vertical motions in our analysis. Vertical velocities are inferred via the omega equation through adoption of quasi-geostrophic dynamics [*Hoskins et al.*, 1978]. After solving this equation, however, the magnitudes of vertical velocities in the region have maxima at ~3 m/day, with most areas producing displacements within the bin size of our data at the time scales used for our analyses O(1-3 days). We therefore ignore vertical velocities in this study, and only use the horizontal, geostrophic currents.

2.3. Pseudo-Lagrangian Method

One difficulty in analyzing data acquired during underway surveys is that during the survey, the tracer will move along streamlines. Subsequent spatial maps of the tracer necessarily include this advection along streamlines, thus confounding the quantification of the true spatial gradients. The pseudo-Lagrangian approach takes the spatial maps of the tracer and back-advects the tracer along the streamlines to their original positions when the survey began. To do this it is necessary to have a well-resolved, stationary flow field with which to define the streamlines. Each tracer sample is advected back along the

streamline for the amount of time between the start of the survey and the given observation, using the velocities along the streamline. The resulting pseudo-Lagrangian spatial map shows the spatial distribution of the tracer as it would have appeared synoptically at the start of the survey. This pseudo-Lagrangian map can then be used to calculate net rates of change of the tracer, as we show below.

2.3.1 Assumptions

The pseudo-Lagrangian transformation entails application of Eulerian velocity fields to convert a surveyed tracer distribution into a pseudo-Lagrangian distribution by removing the effects of advection. Assumptions implicit to this methodology are: a) the physical flow field is known and stationary for the length of time under consideration, and b) the structure of the tracer field moving with the flow is larger than the minimum sampling resolution, i.e. the tracer spatial autocovariance length scale is larger than spacing between observations.

In this study, the first assumption is met: both SeaSoar surveys, spaced a month apart, yield leading-order balanced geostrophic currents that explain the majority of observed velocity field variance (Figure 2.2). The two velocity fields display similar magnitudes and spatial patterns, making the temporal window of a ~3-4 day survey synoptic relative to dynamic changes in the physical flow field. We note that objective mapping was applied to smooth over high-frequency phenomena inevitably aliased within the dataset, such as internal waves, surface gravity wave-induced Stokes drift, and tidal flow [*Kunze and Sanford*, 1984; *Whitt and Thomas*, 2013; *McWilliams and Fox-Kemper*, 2013]. In a sense, then, the maps represent a spatial and temporal averaging.

Generally speaking, time-averaged Eulerian and Lagrangian fields do not produce equivalent velocities [*Andrews and McIntyre*, 1978] and yield different trajectories. Here we assume that the geostrophic current field at this front is leading order and stationary, and we ignore higher-order nonlinear contributions to the flow. In a further attempt to justify geostrophy, we performed our forward advection algorithm (described in Section 4) on a tracer that should be conserved: salinity. Comparing the abilities of the raw ADCP data, objectively mapped ADCP data, and fit geostrophic velocities in conserving salinity, they all performed in a qualitatively similar manner (not shown), though the geostrophic velocities did marginally better. As an additional note, the geostrophic currents also produced the most successful survey line crossings, the necessary condition to calculate net rates of change in the tracer field in our subsequent analysis. This *post hoc* method of validating one's chosen velocity may be useful in future applications of the pseudo-Lagrangian method.

Regarding the second assumption, here we use Chl-*a* fluorescence as the tracer of interest. The observed spatial autocovariance length scales across the front (15 km) are larger than the distance between successive vertical profiles (~2 km), while along-front autocovariance length scales (30 km) are again larger than spacing between SeaSoar survey lines (~20 km). Given this result, we assume that the tracer field between survey locations varies continuously and monotonically, and that finer-scale features are relatively unimportant.

2.3.2 Procedure

Having satisfied the assumptions, we apply the pseudo-Lagrangian transformation (Figure 2.3). Initially, we start with the tracer distribution as surveyed, namely with concentration values at discrete locations on streamlines generated from the geostrophic flow (Figure 2.3a). Discrete sampling locations can be considered to be the Lagrangian position at the time of observation, $\mathbf{X}_{obs} = \mathbf{X}(x,y,t_{obs})$. To calculate Lagrangian positions via integration of the velocity field, we set the reference time $t = 0$ to be at the start of the survey, with $\mathbf{X}_{init} = \mathbf{X}(x,y,0)$. Knowing the time elapsed between the survey start and each observed tracer profile, t_{obs}, we now can solve for each tracer's initial location (at the start of the survey) using the Eulerian velocity field. In this notation, the equation for the time-dependent tracer location $\mathbf{X}_{obs}$ is

$$\mathbf{X}_{obs} = \mathbf{X}_{init} + \int_0^{t_{obs}} \mathbf{U}(x,y,t)\Big|_{(x,y)=\mathbf{X}(x,y,t)} dt \tag{8}$$

We seek $\mathbf{X}_{init}$, which we find by subtracting the particle's trajectory from its observed location $\mathbf{X}_{obs}$. This equates to a backwards advection of the observed position $\mathbf{X}_{obs}$ along its streamline to $\mathbf{X}_{init}$ over a time t_{obs} (Figure 2.3b, c). While simple in form, note that the velocity value in (8) is evaluated at time-varying positions along the streamline that depend on the velocity, complicating its analytical solution. We overcome this problem by approximating the integral as a discrete sum:

$$\mathbf{X}_{init} = \mathbf{X}_{obs} - \sum_{n=0}^{t_{obs}/\Delta t} \mathbf{U}(x,y,t = n\Delta t)\cdot \Delta t \tag{9}$$

where the velocity becomes the value at the recursively calculated position. We implemented this integration with a simple first-order Euler numerical scheme, with $\Delta t \approx$

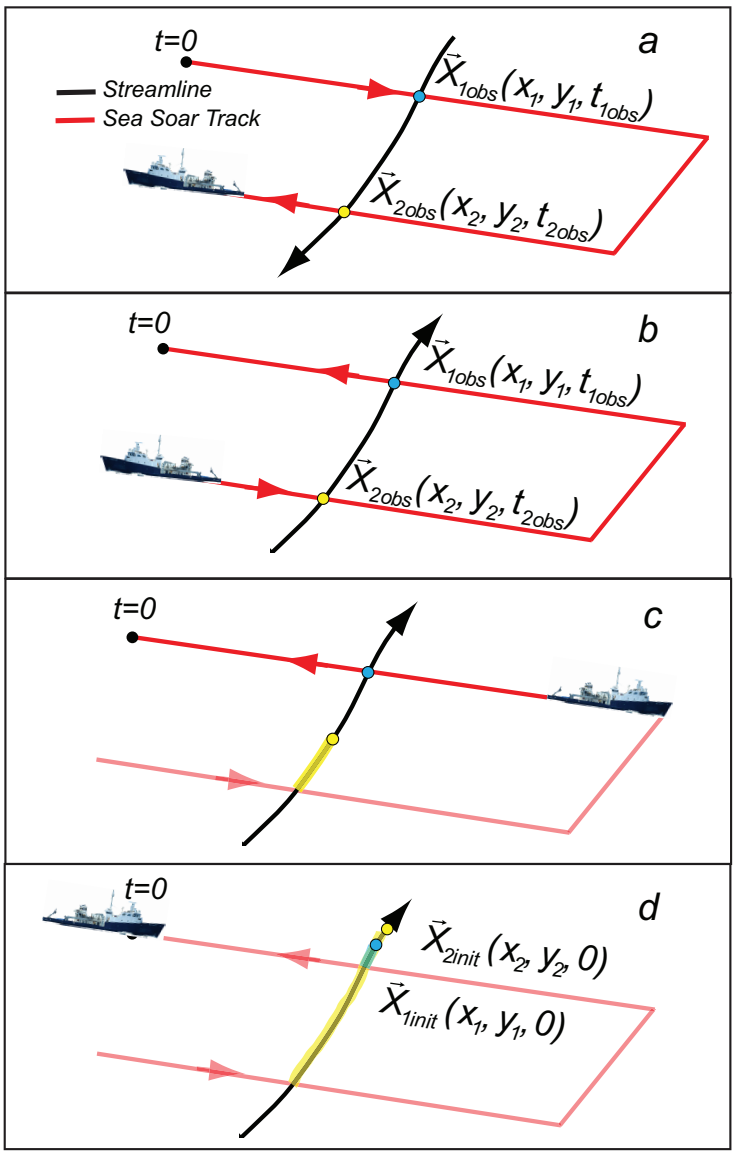

Figure 2.3. Pseudo-Lagrangian procedure. (a) Streamlines of flow are calculated from the survey data. Observations on the same streamline are identified. (b) Flow direction is reversed, and the survey time is reversed. (c) Positions are back-advected for a time t_{obs} from their sampling, to arrive at their inferred initial location (d). Note that a particle sampled later along a streamline can arrive at an initial position upstream of a particle sampled earlier, depending on the flow and the ship's survey speed.

5 min, well within the CFL stability criterion. Velocity values were interpolated from the objectively mapped velocity using inverse-square distance weighting [*Shepard*, 1968].

The accuracy of the method was tested using sequential back- and forward time-integration, yielding locations nearly identical to the profile locations.

The results of this procedure are the data positions where they would have been at the beginning of the survey, $t = 0$ (Figure 2.3d). This is the pseudo-Lagrangian transformation, removing the aliasing due to advection, to present the true, synoptic relative positions of neighboring data profiles at the start of the survey. Note that samples acquired later in the survey could potentially have initially been *upstream* of samples acquired earlier, if the water velocities moved the sampled water downstream faster than the ship surveyed the current (Figure 2.3d). In this situation, the pseudo-Lagrangian-reconstructed ship track will cross itself, giving multiple samplings of the same water parcel.

2.3.3 Analysis of transformed map

Having produced the transformed pseudo-Lagrangian positions of the sample data, we can now interpret the "corrected" distribution of our tracer. A sequence of back-advected positions for SeaSoar Survey 2 Chl-*a* fluorescence data (Figure 2.4) shows that while the velocity field is geostrophic and non-divergent, and should not allow for adjacent water masses to cross over each other, the differential timing of sampling produces regions where certain water positions are sampled twice (labeled as crosses in Figure 2.4d), or where a later sample reflects water "upstream" relative to an earlier sample. Our pseudo-Lagrangian transformation makes it possible to know what regions of sampling are a) connected in a Lagrangian sense to each other through streamlines, and b) whether or not samples acquired later in the survey actually represent samples that

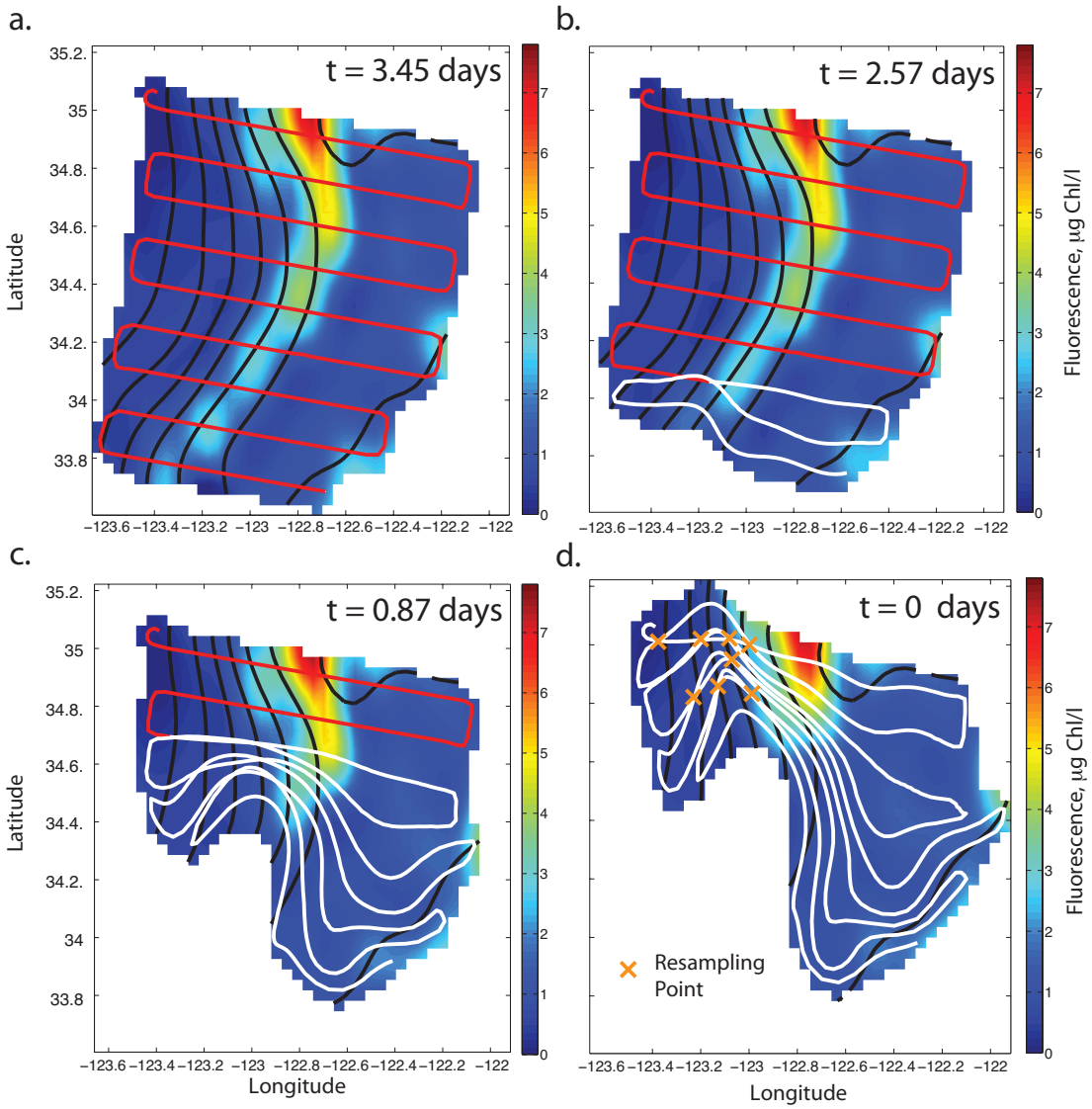

Figure 2.4. Sequential steps in the pseudo-Lagrangian transformation, showing objectively mapped Chl-*a* fluorescence with the initial survey distribution completed after 3.45 days (a), moving back in time to (b) 2.57, (c) 0.87, and (d) 0 days after the survey began. Black lines are the streamlines; red line is the ship track; white line is the pseudo-Lagrangian re-mapped ship track moving backward in time. Panel (d) shows a pseudo-synoptic map of Chl-*a* fluorescence at the start of the survey. Note the enhanced spatial gradients of Chl-*a* fluorescence compared to panel (a). Orange crosses indicate water masses that were sampled twice during the survey.

were downstream of samples acquired earlier in the survey.

Note that resampling of the same water parcel can only occur when the ship is moving in the direction of the flow; Survey 1 was made opposing the flow of the

geostrophic jet, while Survey 2 was made in the direction of the jet. Therefore, resampling only occurs during Survey 2. Given our interest in estimating rates of change of a tracer (requiring multiple samples of the same water at different times), from now on we will focus on the high Chl-*a* feature located in the front during Survey 2.

The pseudo-Lagrangian map of the Chl-*a* fluorescence (Figure 2.4d) shows the distribution *given no local change in Chl-a fluorescence* during the survey. In regions where a water mass was sampled twice during the survey (i.e., the survey lines cross in the pseudo-Lagrangian map) we can make a direct comparison, thus creating some two-point time series to calculate the RHS of (1). For the majority of the survey region, however, Lagrangian resampling did not occur. Instead, a physical distance remains between the pseudo-Lagrangian-transformed water parcels, even though they share a trajectory. Given a stationary velocity field, the physical distance between two profiles that share a streamline amounts to a separation in time. From this perspective, $\mathbf{X}_2$ in figure 2.3 comes from an earlier time in $\mathbf{X}_1$'s trajectory. We can use this information to calculate rates of change of the tracer along a streamline.

If the regions sampled twice have significantly different concentrations, then there must be temporal evolution of the tracer. The pseudo-Lagrangian distribution can thus be used to qualitatively gauge whether or not the RHS of (1) is different from zero. For the Chl-*a* fluorescence distribution (Figure 2.4d), the resampling points are unfortunately in regions of low fluorescence, and it is difficult to estimate net changes in Chl-*a*. The region of high Chl-*a* fluorescence near E-front shrinks in the along-front direction in the pseudo-Lagrangian transformation, indicating that these observations are both close together and part of a continuous Chl-*a* feature. Furthermore, the highest Chl-*a*

observations seen in both Survey 1 and Survey 2 (Figure 2.2b) are found to the north, even though the surveys were done a month apart and in the opposite directions relative to the geostrophic flow. This result suggests a similar source of high Chl-*a* water, which can then be followed to calculate rates of change. The along-front decrease in Chl-*a* in the presence of an along-front flow implies that there must be a sink of Chl-*a* along the front. This observation of decreasing concentrations of Chl-*a* in cold filaments has been previously reported in the region [*Abbott et al.,* 1990; *Hood et al.*, 1991; *MacIsaac et al.*, 1985; *Jones et al.*, 1988; *Strub et al.*, 1991], supporting our contention that Chl-*a* is decreasing. Therefore, we are now in a position to use the velocity flow field to quantify the rates of change of our tracer.

2.4. Calculation of Net Rates of Change of Chl-a

To diagnose how the RHS of (1) evolves during a survey, we need to address the fact that few locations are sampled twice in pseudo-Lagrangian space. To accommodate this, we introduce a simple interpolation scheme to estimate the temporal changes in concentration. Subsequently, we explore sources of variability and error in the rate estimates.

2.4.1 Net Chl-a Growth Rate

Given the variability of biological processes, we want to maximize our use of observed data values at the location and time of collection. To do this, we start with the data locations $\mathbf{X}_{obs}$, i.e., the untransformed tracer field as it was sampled. Rather than integrating backwards as in Section 3, we move a water parcel $\mathbf{X}_{\psi}$ from the location and

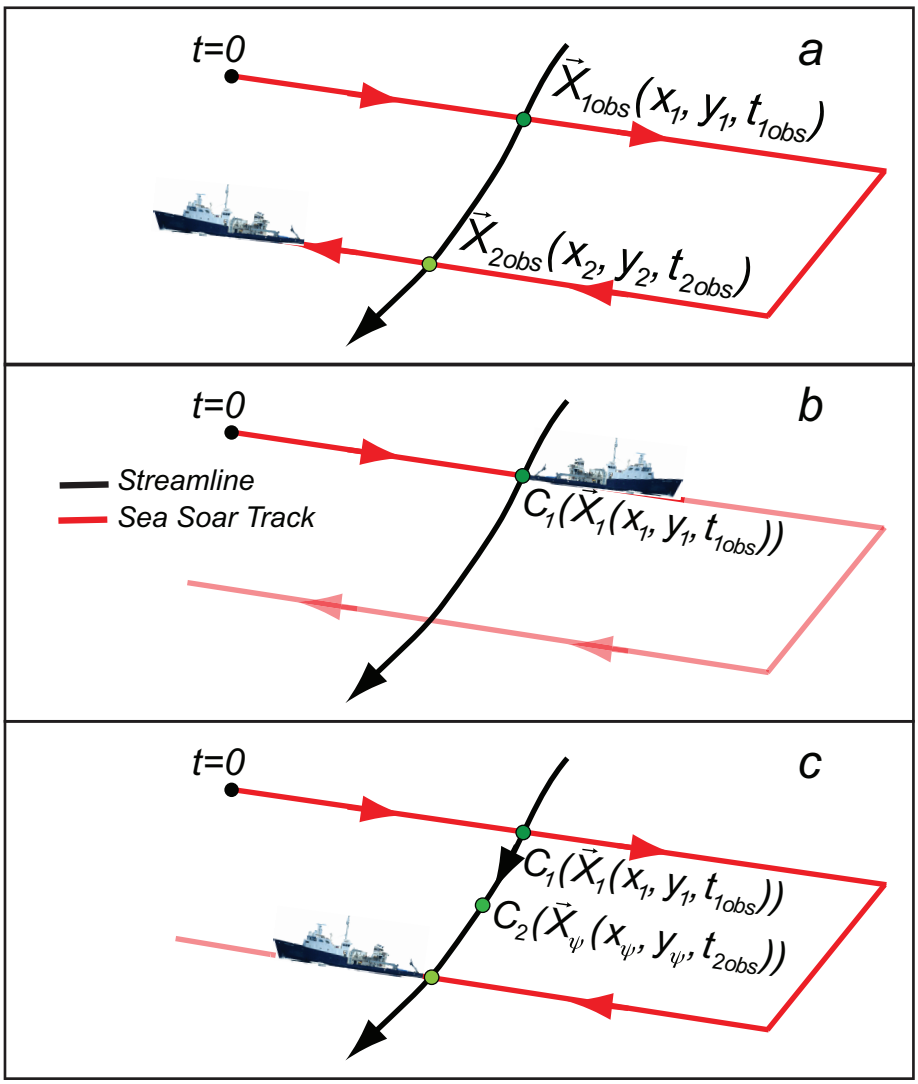

Figure 2.5. Rate calculation method. Starting with two observations connected by a streamline (a), we forward-advect the first observation (b) along its streamline until the ship collects the second observation on the same streamline (c). The first water parcel's new position $\mathbf{X}_\psi$ is used with the objective map of tracer concentration to calculate the second concentration, C_2, for the rate measurement.

time of its initial observation $\mathbf{X}_{1obs}(x_1, y_1, t_{1obs})$ forward in time along its streamline. We advect $\mathbf{X}_\psi$ along its streamline for the amount of time it takes until we obtain the next observation along that same streamline, $\mathbf{X}_{2obs}(x_2, y_2, t_{2obs})$. Note that $\mathbf{X}_\psi$ may not have reached the location of $\mathbf{X}_{2obs}$ during this time (Figure 2.5).

To calculate a net rate we need two Chl-*a* estimates from the same water parcel, and the time between samples. The time between samples for our rate measurement is the time elapsed between the two observations on the same streamline, namely $\Delta t = t_{2obs}\text{-}t_{1obs}$. For the initial Chl-*a*, we use the objectively mapped value at $\mathbf{X}_{1obs}$, which we call $C_1 = C(\mathbf{X}_{1obs})$. The final Chl-*a* value, C_2, is interpolated to the location $\mathbf{X}_{\psi}(x_{\psi}, y_{\psi}, t_{1obs} + \Delta t)$, otherwise known as $\mathbf{X}_{\psi}(x_{\psi}, y_{\psi}, t_{2obs})$. We now calculate a net specific growth rate, using the equation

$$r = \frac{1}{C_1[\mathbf{X}_1(x_1, y_1, t_{1obs})]} \cdot \frac{C_2[\mathbf{X}_{\psi}(x_{\psi}, y_{\psi}, t_{2obs})] - C_1[\mathbf{X}_1(x_1, y_1, t_{1obs})]}{\Delta t} \qquad (10)$$

To estimate the rate of change of Chl-*a* fluorescence in the high-fluorescence feature seen at the front in the survey (Figure 2.4), we limit our present analyses to trajectories with initial fluorescence values ≥3 μg Chl-*a* l^{-1}. For Survey 2 this results in 156 independent estimates of the net specific growth rate (Figure 2.6). The calculations provide unusually high-resolution rate estimates over a large spatial region of ~1200 km^2 (Figure 2.7), with a mean value of -0.167 day^{-1}. Given the overall decrease in observed Chl-*a* fluorescence along the geostrophic jet, the negative value of the mean net growth rate is not surprising. The utility of this analysis lies in the fact that what was previously a qualitative intuition (*i.e.*, that Chl-*a* fluorescence decreased) has now been quantitatively estimated.

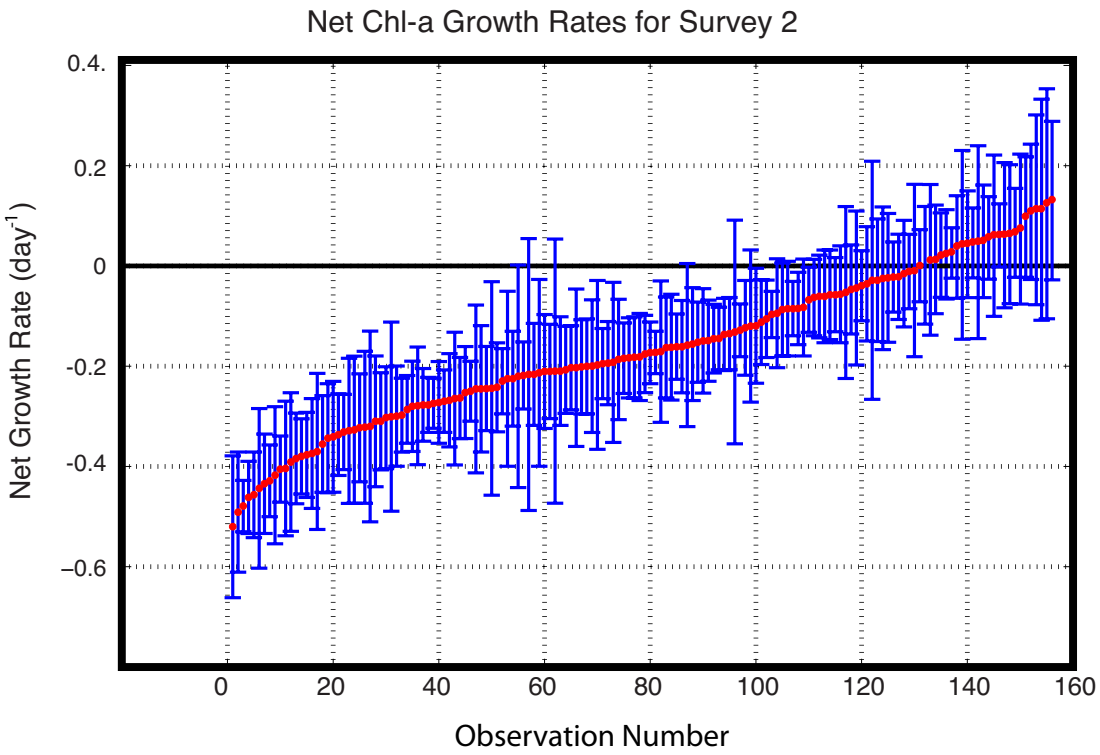

Figure 2.6. Calculated net Chl-*a* growth rates for Survey 2. Red dots indicate the rate estimate, and blue error bars are 95% confidence intervals as determined by eqn. (14).

2.4.2. Error in the rate measurement

The previous section's calculation of net Chl-*a* growth rates is not very useful without some quantification of the error associated with the result. In order to achieve this, here we diagnose in (10) each source of error in turn. There are three pieces of information are required to calculated r: the initial Chl-*a*, C_1, the final Chl-*a*, C_2, and the elapsed time Δt.

Since we chose the elapsed time to be based upon the times of our sampling locations, we do not assign an error to this term. The initial Chl-*a* value is determined from the relative error in the objective map, which has an assumed noise-to-signal ratio of ≤0.05. This value is indeed reflective of the proportion of the power spectrum selected with the 1 Hz smoothing and binning of the raw 24 Hz fluorescence time series. In using

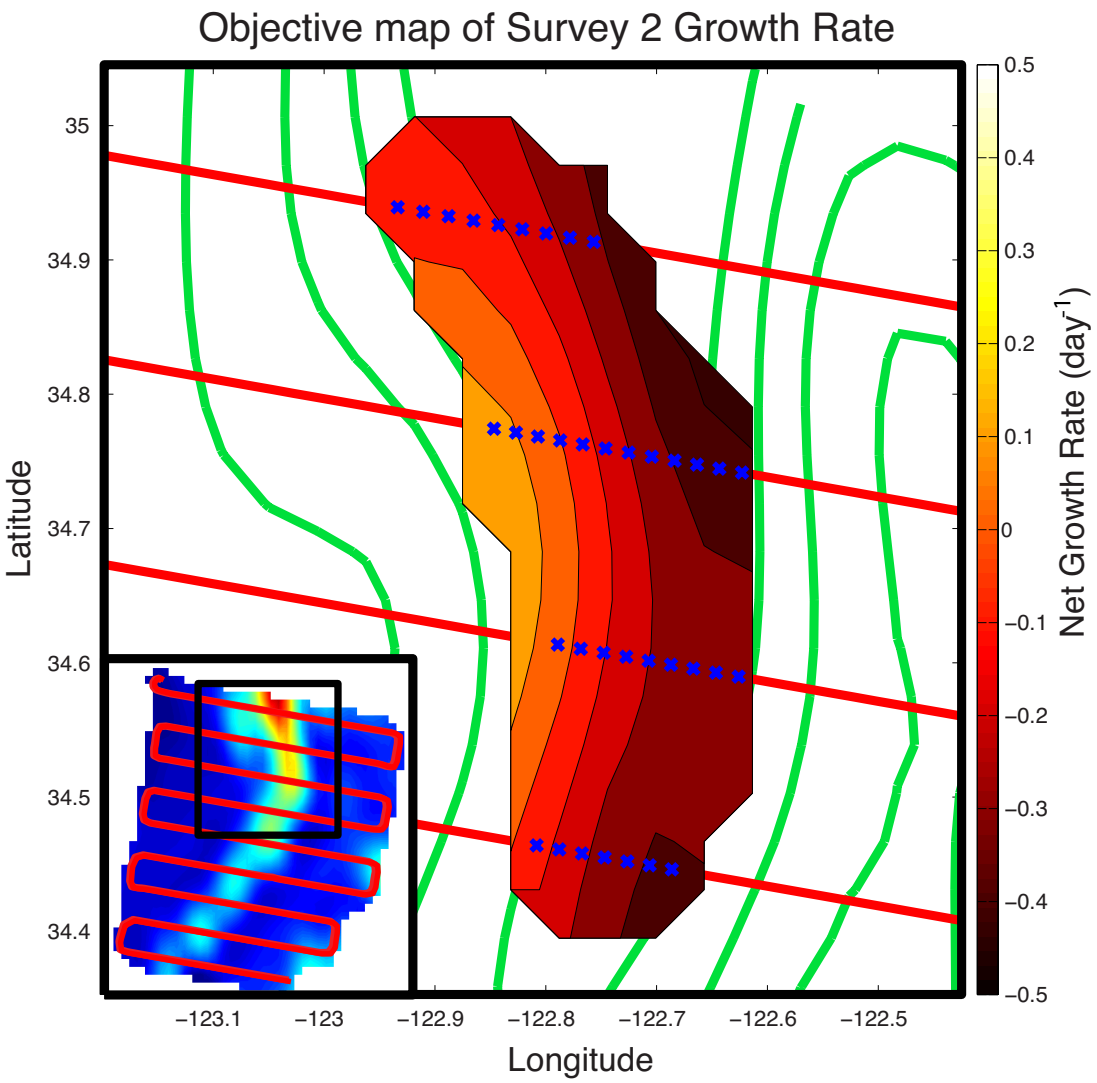

Figure 2.7. Objective map of estimated net growth rates at 27 meters. Red line is the Survey 2 ship path. Green contours indicate Chl-*a* fluorescence. Blue crosses indicate rate observation locations, totaling 37 at this depth. Inset is the survey path, with a black box indicating the zoomed-in region.

Le Traon's method [1990], anisotropic fluctuations to the assumed mean are added to the error due to the autocovariance of the tracer field in along and cross-front directions. We therefore get a standardized mean square error for each position in the tracer field, which is directly applied to the initial Chl-*a* value C_1.

The final Chl-*a* value, C_2, will have not only the error assigned by the objective map, but also an error in the advection scheme in arriving at the correct position. To quantify this effect, we model the spatial misfit with a diffusion-like process. The validity in using a diffusion process to model misfit can be argued for by analyzing conservation of salinity. After conducting the pseudo-Lagrangian transformation from section 3 (and shown in figure 2.4) on salinity, we use the difference between new mapped salinity and original salinity as a misfit metric. This difference is squared and summed over the map, then normalized by the number of observations. The time series of this misfit (not shown) grows over time in a qualitatively quadratic fashion, similar to particle dispersion at short timescales [*La Casce*, 2008]. In the context of E-front, where salinity gradients should be mostly perpendicular to the geostrophic velocities, and salinity is assumed to be conserved, the misfits of salinity should correlate with misfits of position due to error in the velocity field. Therefore, a diffusion model is chosen in determining the velocity error.

A diffusion model requires a determination of the diffusivity, which we do by advecting salinity forward in time. For each rate measurement, there is an associated salinity difference between the observations connected by streamlines. The time T necessary for advection is known. The relevant distance scale, L, is determined moving along the survey line and subsequently identifying the position that matches the original salinity. The apparent diffusivity, κ, can be found by the following relation:

$$\kappa = \frac{L^2}{4T} \tag{11}$$

The estimates of κ arrived at by advection of salinity has a fat-tailed distribution, and we choose the median value of 120 m^2/s to represent the velocity misfit.

Taking the observation C_1 at the point $\mathbf{X}_{1obs}$ as a discrete point whose position is known with certainty, we represent the probability distribution of its initial location as the Dirac delta function. This distribution has many useful properties, including the fact that its integral over all space is one, making it appropriate to use as a pdf. Using the Dirac delta function as the initial condition at $\mathbf{X}_{1obs}$, the subsequent probability distribution of position as a function of time Δt is

$$\Phi(x,\Delta t) = \frac{1}{\sqrt{4\pi\kappa\Delta t}} \exp\left(-\frac{x^2}{4\kappa\Delta t}\right). \tag{12}$$

Equation (12) gives the probability distribution for the cross-streamline location of a water parcel starting at $\mathbf{X}_{1obs}$ that is advecting along a streamline assuming a velocity error modeled by diffusion. Given the elapsed time Δt, one can calculate a probability density function for positions on either side of the water parcel centered at $\mathbf{X}_{1obs}$ (Figure 2.8), and we here select the distances corresponding to 95% confidence intervals.

Inclusion of the diffusion-like model produces two displacements representative of velocity error. Evaluating Chl-*a* at these two locations, their relative difference from C_2 produces a similar 95% confidence interval in the variability of C_2. Normally, the error from the objective map would be included in the range of these Chl-*a* values, but in practice for our application, the modeled diffusion variance was an order of magnitude larger than the objective map's, and so the objective map error is ignored for C_2.

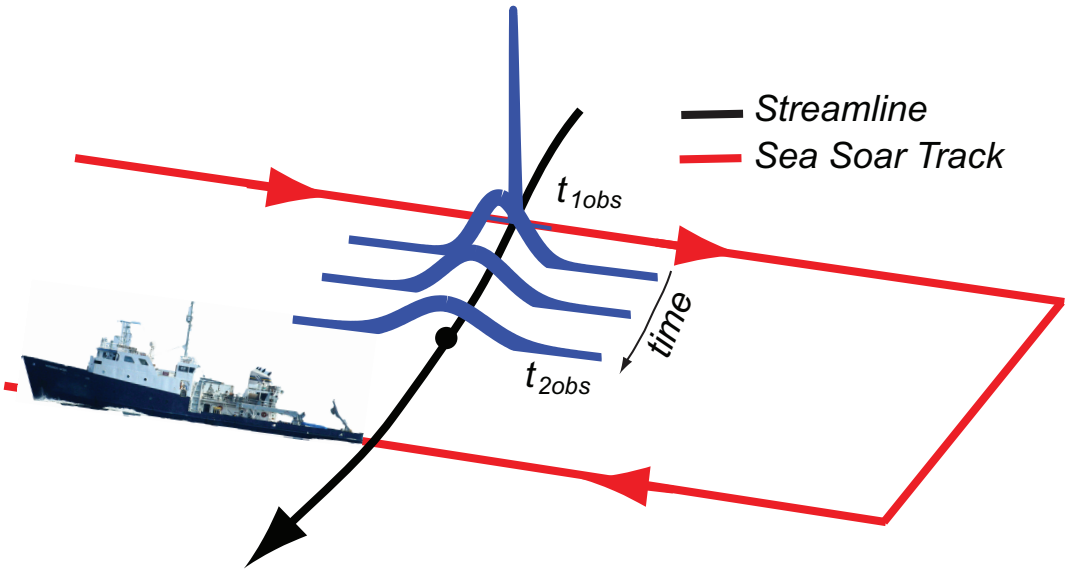

Figure 2.8. Diffusion-like model used for rate measurement error. The location probability distribution begins as a delta function at t_{1obs}, and sequentially spreads according to eq. 12 until t_{2obs}.

Armed with the variances for both C_1 and C_2, we now return to the rate calculation. Multiplying (10) by Δt, which we assume to be known, and splitting the numerator, we arrive at

$$r\Delta t = \frac{C_2}{C_1} - \frac{C_1}{C_1} \Rightarrow r\Delta t = \frac{C_2}{C_1} - 1 \tag{13}$$

Through this manipulation, the only portion with error is the ratio C_2/C_1, since by definition C_1/C_1 will be equal to 1. The probability distribution for ratios of Gaussian variables is provided by *Hinkley* [1996] and becomes

$$P(z) = \frac{b(z)d(z)}{\sqrt{2\pi}\sigma_2\sigma_1 a^3(z)}\left[\Lambda\left\{\frac{b(z)}{\sqrt{1-\rho^2}a(z)}\right\} - \Lambda\left\{-\frac{b(z)}{\sqrt{1-\rho^2}a(z)}\right\}\right] + \frac{\sqrt{1-\rho^2}}{\pi\sigma_2\sigma_1 a^2(z)}\exp\left\{-\frac{c}{2(1-\rho^2)}\right\} \tag{14}$$

with z being C_2/C_1, standard errors σ_1,σ_2, means μ_1, μ_2, and correlation ρ, with the definitions

$$a(z) = \left(\frac{z^2}{\sigma_2^{\,2}} - \frac{2\rho z}{\sigma_2 \sigma_1} + \frac{1}{\sigma_1^{\,2}} \right)^{\frac{1}{2}} \tag{15}$$

$$b(z) = \frac{\mu_2 z}{\sigma_2^{\,2}} - \frac{\rho(\mu_2 + \mu_1 z)}{\sigma_2 \sigma_1} + \frac{\mu_1}{\sigma_1^{\,2}} \tag{16}$$

$$c = \frac{\mu_2^{\,2}}{\sigma_2^{\,2}} - \frac{2\rho\mu_2\mu_1}{\sigma_2\sigma_1} + \frac{\mu_1^{\,2}}{\sigma_1^{\,2}} \tag{17}$$

$$d(z) = \exp\left\{ \frac{b^2(z) - c a^2(z)}{2(1-\rho^2)a^2(z)} \right\} \tag{18}$$

$$\Lambda(y) = \int_{-\infty}^{y} \phi(u)du, \text{ where } \phi(u) = \frac{1}{\sqrt{2\pi}} \exp\left\{ -\frac{1}{2}u^2 \right\}. \tag{19}$$

The standard error and means change with each rate measurement, and the correlation was found for the 156 measurements to be 0.91. With the ratio pdf calculated, we finally arrive at the ability to find 95% confidence intervals for our ratio measurements. Taking these values, subtracting one and multiplying by the observation's Δt gets the confidence interval for each rate, which we display in figure 2.6, with the rates presented in increasing order for visual comparison. Out of 156 points, 64% are found to be significantly less than zero, with none found to be significantly greater than zero.

Through the adoption of a diffusion-like model to account for error in the velocity field, it is thus possible to quantify to what extent the pseudo-Lagrangian method produces meaningful rates for a given application.

2.4.3 Comparison to traditional rate measurements

The pseudo-Lagrangian approach to estimating net rates from tracer data will be a valuable tool in evaluating tracer evolution in conjunction with other, more traditional

methods. Since measured tracer concentration reflects all the processes that occur in a water parcel, the net rates derived from our described method provide a rate ostensibly comparable with a total budget of rate measurements based on individual mechanisms. Examples of traditional rate measurements affecting phytoplankton include: dilution experiments to quantify phytoplankton growth and microzooplankton grazing [*Landry and Hassett*, 1982], mesozooplankton gut fluorescence data to determine mesozooplankton grazing [*Mackas and Bohrer*, 1976; *Kiørboe et al.*, 1985], and sediment traps to estimate vertical flux of particulates [*Knauer et al.*, 1979]. Apart from the growth measured in dilution experiments, most of these observations quantify loss terms in the RHS of (1). Therefore, rate estimates from any of these traditional methods, which inevitably leave out some loss processes, should be slightly more positive than the rate found by the pseudo-Lagrangian method, which implicitly includes them all.

Additionally, careful attention must be paid to confounding effects of these individual rate measurements. For example, the bottle incubations used in dilution experiments exclude mesozooplankton grazers, and so the estimated net growth rate includes a possible predation release from mesozooplankton. Further problems arise comparing biological data from localized water parcels to data reflecting integrated quantities, for example, comparing bottle dilution rates with vertical plankton tows for mesozooplankton grazing. While these different methods lead to biological rates of similar units (*e.g.* day^{-1}), it is impossible to assume *a priori* that these rates should be comparable such that they can be linearly added and subtracted to match up to a total net rate as calculated in the pseudo-Lagrangian method.

In our present use of the pseudo-Lagrangian technique, we use an ensemble approach wherein all observations of sufficient Chl-*a* are used to estimate net changes of tracer concentration. Therefore, values from various depths but belonging to the same high Chl-*a* feature are used. In this case, vertically integrated rate measurements, such as mesozooplankton gut fluorescence tows, should be comparable with the pseudo-Lagrangian rate, assuming that grazing can be equally applied across the feature. Localized measurements, such as dilution rates, should be compared with pseudo-Lagrangian rates measured from observations at the same depth. Calculating the relative variance of net growth rates from both constant-depth and integrated perspectives can provide an avenue to account for the bias of methodology in traditional rate measurements.

Due to the experimental layout of the E-Front cruise, the only experimental rate estimates that were spatiotemporally close to the second SeaSoar survey were the mesozooplankton gut fluorescence data. These data were collected and processed as described in *Landry et al.* [2009]. The mesozooplankton grazing rate for our feature averages to –0.3 day^{-1} (Mark Ohman, personal communication). These values compare well with some of the pseudo-Lagrangian observations, though the majority are significantly more positive than -0.3 (56%). While strong grazing provides a mechanism for the overall decrease in Chl-*a*, the magnitude suggests that some positive contribution to the RHS of (1) is present, such as *in situ* growth of Chl-*a*. A rigorous and quantitative comparison of pseudo-Lagrangian and experimentally derived rates, however, is beyond the scope of this study.

2.5. Discussion

The methods outlined above provide two results: 1) a transformed pseudo-Lagrangian map of sampled data that reflects more accurate relative positioning of samples obtained in a moving fluid, and 2) a distribution of estimated rates of change of tracer concentration to quantify the RHS of (1). The most significant assumption necessary in our analysis is the presence of a stationary, geostrophic velocity field. We quantified the possible contribution of ageostrophic vertical upwelling or subduction through the omega equation and determined that it was small enough to ignore for our present analysis. However, incorporating these effects with others, such as wind forcing or Stokes drift, would help to assess their contribution to the observed decrease in Chl-*a*. Without direct measurements, some of these effects are difficult to incorporate into our velocity field in a consistent manner. Progress is being made on understanding the impact of these phenomena upon ocean fronts [*McWilliams and Fox-Kemper*, 2013], and we plan to address this issue in the future. Given these dynamical omissions, our present use of the geostrophic velocity field still yields useful insights.

The pseudo-Lagrangian transformation allows for a better interpretation of a given sampling distribution, and is a useful way to reorganize survey locations into a single, consistent snapshot (Figure 2.4d). Without the transformation, we would not know the extent of resampling that occurred in the western portion of Survey 2. Generally speaking, this remapping of the survey conducted in the direction of the dominant flow produces regions that allow point-to-point comparisons for quantifying the RHS of (1). Unfortunately in our dataset this was not possible due to the very low Chl-*a* concentrations there. We also used the pseudo-Lagrangian map to interpret whether the

Chl-*a* concentrations were static over time. A differencing of the transformed map with the original distribution, though of possible use qualitatively, cannot be used directly for rate estimates due to the overlapping of measurements from different times. We therefore use our forward-advecting methodology to estimate rates.

The application of our rate estimation methodology to E-Front yields spatially resolved rates of change of our chosen tracer, Chl-*a* fluorescence. What is at first visually obvious from figure 2.2d – a general decrease in Chl-*a* along the front – has now been quantitatively estimated from ensemble observations. The usual field methods for estimating such rates (e.g., *in situ* dilution methods or primary productivity measurements) requires first identifying the feature, returning to it, and incubating experimental flasks on a platform that follows the flow. The result is a single point measurement, obtained through a great deal of effort both on the ship and subsequently in the lab. By selectively choosing our Chl-*a* threshold and focusing on the high-fluorescence region, we obtained 156 estimates of net growth rate within this feature. Together, these estimates yield a range of rates comparable to those estimated from gut fluorescence, and well within the range of rates observed in other studies of our region [*Landry et al.*, 2009; *Li et al.*, 2010; *Li et al.*, 2011].

One practical consequence of our analyses is that the survey direction relative to the flow matters. As previously mentioned, sampling in the direction of the geostrophic jet allows for identification of resampled water parcels. Though these regions were not used in our analysis, the fact remains that resampling of water parcels would not occur in a survey conducted upstream, where all later observations would always come from water parcels located farther upstream. Thus, in light of the pseudo-Lagrangian

transformation, planning a ship track designed for biogeochemical tracer rate analysis would dictate a downstream sampling strategy.

Another consequence of sampling direction is the sharpening and weakening of observed tracer gradients. *Rixen et al.* [2001] note this in their numerical study replicating asynoptic data collection: upstream (downstream) sampling sharpens (weakens) estimated tracer gradients. For our rate measurements, this would imply that our results from Survey 2, conducted downstream, underestimate the true gradients in Chl-*a* (as is clear from the pseudo-Lagrangian remapped data, Figure 2.4), and hence produce reduced magnitudes of the net growth rate. Our conclusion of a non-zero rate of change is thus conservative. *Rixen et al.* [2001] pursued an approach whereby dynamically active tracers (temperature, salinity, and density) were advected and used in a new calculation of geostrophic velocity and tracer fields. This was done iteratively until convergence was reached. While this approach is useful for creating a self-consistent density and geostrophic velocity field, there is no equivalent way to sequentially alter and correct data from biogeochemical tracers, which do not impact the physical dynamics.

Throughout this study, we have made reference to calculating net tracer growth rates. This nomenclature requires some clarification. Firstly, our use of Chl-*a* fluorescence means that the calculated rates are exactly that: the rate of change of Chl-*a*. Chlorophyll-*a* is not directly useful in quantifying phytoplankton biomass or carbon [*Kruskopf and Flynn*, 2006], and so the change in chlorophyll-*a* does not translate into a change in the population or organic carbon *per se*. However, many of the rate measurements mentioned in section 4.3 measure chlorophyll-*a*, and so measureable ecological rates, such as grazing, can be expressed as the rate of removal of Chl-*a*. The

ability to compare this methodology with other traditional methods by using the same tracer is of primary importance; if one wishes to express changes in biomass or carbon, then direct measurements are necessary. Secondly, the word "net" in net tracer growth reflects how this method measures the change due to all the biological processes on the RHS of (1) acting at once, i.e. growth, grazing, sinking, swimming, etc. Other *in situ* measurements of rates isolate and resolve only certain ecosystem processes. As a result, our method produces a quantitative rate budget constraint that must be satisfied when compared to all other ecosystem processes affecting Chl-*a*.

Looking at the spatial map of net growth rates as determined by advection only (Figure 2.7), there are visible gradients in the rate measurements, with rates located in the western part of the feature having higher absolute values than those to the east. If the high Chl-*a* feature was indeed evolving as a whole, one might expect zero spatial gradient. This gradient may arise from errors in our geostrophic velocities following the true trajectory of the feature, where values near the edge may erroneously wander in and out of the distribution. There is no immediate way to remedy this situation, apart from including more complicated and accurate physical processes. Regardless, the range of rate values found in our spatial map are reasonable and the possible variability due to advective error equivalent to other *in situ* observations [*Landry et al.*, 2009; *Li et al.*, 2010; *Li et al.*, 2011].

2.6. Conclusions

The pseudo-Lagrangian approach described here provides a powerful tool for analyzing biogeochemical tracer fields from spatial surveys. Though the notion of

utilizing Eulerian velocity fields to advect Lagrangian positions is not novel, here we take advantage of what is usually considered a limitation: the non-synopticity of ship sampling. A ship can be only in one place at one time, while the fluid is simultaneously moving, and advecting tracers with it. Thus, ship surveys always alias the spatial distributions of properties. Here, in a situation where the physical dynamics can be considered quasi-stationary, we utilize these time-aliased observations to systematically produce estimates of short-term tracer dynamics.

The tracer transformation in section 3 allows for reanalysis of observations to determine whether the RHS of (1) is non-zero, that is, whether there are local rates of change of the tracer not driven by advection. In phytoplankton communities where large rates of growth and mortality often cancel to create a near-balance of the RHS of (1), determining its sign and difference from zero is often non-trivial [*Jickells et al.*, 2008]. By removing the effects of advection, an investigator can now determine whether certain observations are replicates of the same water parcel, and where temporally distinct observations originated relative to each other in space.

The applicability of the pseudo-Lagrangian transformation requires satisfying several conditions. In regions where high-frequency water movements dominate local flow and create essentially stochastic noise overlying a weaker mean circulation, such as near-shore coastal regions, the lack of deterministic knowledge of the flow field makes pseudo-Lagrangian advection impossible to implement. Considering the size and speed of research vessels, the physical features most amenable to pseudo-Lagrangian analyses would be mesoscale regions, such as fronts and eddies, that are largely in geostrophic balance and are relatively stationary during the survey period.

A further limitation of the method is that the biogeochemical tracers of interest must be able to be rapidly sensed by a towed platform to create the objectively mapped field. For example, the SeaSoar deployment in this study contained a fluorometer, transmissometer, and oxygen sensor. While some measurements can be used as proxies for other desired variables (such as dissolved oxygen in calculating aragonite saturation; **[***Alin et al.*, 2012; *Bednaršek and Ohman*, 2015]), other quantities still require intense sampling and possible post-processing in the lab. Recent development of remote sensing equipment for difficult biogeochemical measurements such as pH [*Martz et al.*, 2010] and alkalinity [*Spaulding et al.,* 2014] will allow for their eventual inclusion in more ambitious deployments. Currently, large-scale programs, such as Argo [*Freeland et al.*, 2010], are driving instrument development toward autonomous and low-power miniaturized devices. Towed instruments do not have such a power limitation, providing a deployment platform for new instruments before they are optimized for autonomous vehicles. Data acquired by these new technologies on platforms such as SeaSoar could benefit from the methodology outlined here to provide spatially resolved rate estimates not currently available.

The tracer rate analysis method presented here also allows for quantifying the dynamics underlying observed tracer distributions. Still, the analyses must be carefully interpreted. First, the limitations of a given tracer must be recognized. Though Chl-*a* fluorescence is often used as a proxy for phytoplankton biomass, we strictly discourage interpreting our Chl-*a* net growth rates as a change in biomass or carbon, and limit conclusions to factors directly affecting Chl-*a*. Additionally, the separate terms on the RHS of (1) cannot be distinguished from each other using our technique: we obtain a *net*

rate resulting from all the possible processes in (1). The *net* rate calculated from these *in situ* observations complement the traditional, difficult biogeochemical rate measurements that can separate the various processes on the RHS of (1) (e.g., growth and grazing rate measurements, sinking fluxes from sediment traps, etc.) by providing estimates for the overall rate balance.

In conclusion, our pseudo-Lagrangian scheme provides a method to re-map observational data to remove aliasing due to advection, and produces high-resolution estimates of net rates over spatial scales that are not achievable using traditional methods of direct observation. The limitations of the pseudo-Lagrangian method arise mainly from undetermined physical flows, and the suite of tracers available for towed deployment. Extension of the technique's applicability is possible through advances in instrument development. Used as a complementary dataset to more traditional analyses at sea, the pseudo-Lagrangian technique provides a large set of independent observations to compare with the usual syntheses of disparate measurements used to calculate ecological and biogeochemical budgets.

Acknowledgements

The data for this paper are available upon request from the National Science Foundation California Current Ecosystem (CCE) Long Term Ecological Research (LTER) site. http://cce.lternet.edu/

This work was supported by National Science Foundation (NSF) funding (1026607) for the CCE-LTER site.

We are grateful to the captain and crew of the R/V Melville and all the participants of CCE-LTER August 2012 process cruise. In particular, we thank Carl Matson for SeaSoar deployment and recovery, Alexander Chekalyuk and Mark Hafez for ALF-A data, along with Ralf Goericke for chlorophyll-*a* data. The manuscript benefitted greatly from the input of both Mark Ohman and Michael Landry.

Chapter 2, in full, is a reprint of previously published material in Journal of Geophysical Research: Oceans, in press, de Verneil, A., and Franks, P.J.S. The dissertation author was the primary investigator and author of this paper.

References

Abbott, M. R., Brink, K.H., Booth, C.R., Blasco, D., Codispoti, L.A., niiler, P.P., Ramp, S.R., 1990. Observations of phytoplankton and nutrients from a Lagrangian drifter off northern California. *Journal of Geophysical Research: Oceans (1978–2012)*, *95*(C6), 9393-9409. doi: 10.1029/JC095iC06p09393.

Abbott, M. R., Zion, P.M., 1985. Satellite observations of phytoplankton variability during an upwelling event. *Continental Shelf Research*, *4*(6), 661-680. doi:10.1016/0278-4343(85)90035-4.

Alin, S. R., Feely, R.A., Dickson, A.G., Hernández-Ayón, J.M., Juranek, L.W., Ohman, M.D., Goericke, R., 2012. Robust empirical relationships for estimating the carbonate system in the southern California Current System and application to CalCOFI hydrographic cruise data (2005–2011). *Journal of Geophysical Research: Oceans (1978–2012)*, *117*(C5). doi: 10.1029/2011JC007511.

Allen, J. T., Smeed, D.A., Nurser, A.J.G., Zhang, J.W., Rixen, M., 2001. Diagnosis of vertical velocities with the QG omega equation: an examination of the errors due to sampling strategy. *Deep Sea Research Part I: Oceanographic Research Papers*, *48*(2), 315-346. doi: 10.1016/s0967-0637(00)00035-2.

Andrews, D. G., McIntrye, M.E., 1978. An exact theory of nonlinear waves on a Lagrangian-mean flow. *Journal of Fluid Mechanics*, *89*(04), 609-646. doi: 10.1017/s0022112078002773.

Bednaršek, N., Ohman, M.D., 2015. Changes in pteropod distributions and shell dissolution across a frontal system in the California Current System. *Marine Ecology Progress Series* (in press). doi: 10.3354/meps11199.

Blanke, B., Raynaud, S., 1997. Kinematics of the Pacific Equatorial Undercurrent: an Eulerian and Lagrangian approach from GCM results. *Journal of Physical Oceanography*, *27*(6), 1038-1053. doi: 10.1175/1520-0485(1997)027<1038:KOTPEU>2.0.CO;2.

Bowman, K. P., Lin, J.C., Stohl, A., Draxler, R., Konopka, P., Andrews, A., Brunner, D., 2013. Input data requirements for Lagrangian trajectory models. *Bulletin of the American Meteorological Society*, *94*(7), 1051-1058. doi: 10.1175/BAMS-D-12-00076.

Boyd, P. W., Jickells, T., Law, C.S., Blain, S., Boyle, E.A., Buesseler, K.O., … Watson, A.J., 2007. Mesoscale iron enrichment experiments 1993-2005: Synthesis and future directions. *Science*, *315*(5812), 612-617. doi: 10.1126/science.1131669.

Bracco, A., Provenzale, A., Scheuring, I., 2000. Mesoscale vortices and the paradox of the plankton. *Proceedings of the Royal Society of London. Series B: Biological Sciences*, *267*(1454), 1795-1800. doi: 10.1098/rspb.2000.1212.

Chekalyuk, A. M., Hafez, M.A., 2008. Advanced laser fluorometry of natural aquatic environments. *Limnology and Oceanography: Methods*, *6*, 591. doi: 10.4319/lom.2008.6.591.

Chekalyuk, A.M., Hafez, M.A., 2011. Photo-physiological variability in phytoplankton chlorophyll fluorescence and assessment of chlorophyll concentration. *Optics express* 19.23, 22643-22658. doi: 10.1364/OE.19.022643

D'Asaro, E. A., 2003. Performance of autonomous Lagrangian floats. *Journal of Atmospheric and Oceanic Technology*, *20*(6), 896-911. doi: 10.1175/1520-0426(2003)020<0896:POALF>2.0.CO;2.

D'Asaro, E. A., Lee, C., Rainville, L., Harcourt, R., Thomas, L., 2011. Enhanced turbulence and energy dissipation at ocean fronts. *Science*, *332*(6027), 318-322. doi: 10.1126/science.1201515.

d'Ovidio, F., De Monte, S., Alvain, S., Dandonneau, Y., Lévy, M., 2010. Fluid dynamical niches of phytoplankton types. *Proceedings of the National Academy of Sciences*, *107*(43), 18366-18370. doi: 10.1073/pnas.1004620107.

d'Ovidio, F., Fernández, V., Hernández-García, E., López, C., 2004. Mixing structures in the Mediterranean Sea from finite-size Lyapunov exponents. *Geophysical Research Letters*, *31*(17). doi: 10.1029/2004gl020328.

Doglioli, A. M., Veneziana, M., Blanke, B., Speich, S., Griffa, A., 2006. A Lagrangian analysis of the Indian-Atlantic interocean exchange in a regional model. *Geophysical research letters*, *33*(14). doi: 10.1029/2006gl026498.

Doglioli, A. M., Nencioli, F., Petrenko, A.A., Rougier, G., Fuda, J.L., Grima, N., 2013. A software package and hardware tools for in situ experiments in a Lagrangian reference frame. *Journal of Atmospheric and Oceanic Technology*, *30*(8), 1940-1950. doi: 10.1175/JTECH-D-12-00183.1.

Dragani, R., Redaelli, G., Visconti, G., Mariotti, A., Rudakov, V., Mackenzie, A.R., Stefanutti, L., 2002. High-resolution stratospheric tracer fields reconstructed with Lagrangian techniques: A comparative analysis of predictive skill. *Journal of the atmospheric sciences*, *59*(12), 1943-1958. doi: 10.1175/1520-0469(2002)059<1943:HRSTFR>2.0.CO;2.

Firing, E., Hummon, J.M., 2010. Shipboard ADCP measurements. *The go-ship repeat hydrography manual: a collection of expert reports and guidelines. IOCCP report*, (14), 1-11.

Freeland, H. J., Roemmich, D., Garzoli, S.L., Le Traon, P.Y., Ravichandran, M., Riser, S., … Xu, J., 2010. Argo-a decade of progress. In *OceanObs' 09: Sustained Ocean Observations and Information for Society (Vol. 2), Venice, Italy, 21-25 September 2009*. doi: 10.5270/oceanobs09.cwp.32.

Gurvich, A. S., Yaglom, A.M., 1967. Breakdown of eddies and probability distributions for small-scale turbulence. *Physics of Fluids (1958-1988)*, *10*(9), S59-S65. doi: 10.1063/1.1762505.

Hinkley, D.V., 1969. On the ratio of two correlated normal random variables. *Biometrika* 56.3, 635-639. doi: 10.1093/biomet/56.3.635

Hood, R. R., Abbott, M.R., Huyer, A., 1991. Phytoplankton and photosynthetic light response in the coastal transition zone off northern California in June 1987. *Journal of Geophysical Research: Oceans (1978–2012)*, *96*(C8), 14769-14780. doi: 10.1029/91jc01208.

Hoskins, B. J., Draghici, I., Davies, H.C., 1978. A new look at the ω-equation. *Quarterly Journal of the Royal Meteorological Society*, *104*(439), 31-38. doi: 10.1256/smsqj.43902.

Jickells, T. D., Liss, P.S., Broadgate, W., Turner, S., Kettle, A.J., Read, J., … DeGrandpre, M.D., 2008. A Lagrangian biogeochemical study of an eddy in the Northeast Atlantic. *Progress in Oceanography*, *76*(3), 366-398. doi: 10.1016/j.pocean.2008.01.006.

Jones, B. H., Atkinson, L.P., Blasco, D., Brink, K.H., Smith, S.L., 1988. The asymmetric distribution of chlorophyll associated with a coastal upwelling center. *Continental Shelf Research*, *8*(10), 1155-1170. doi: 10.1016/0278-4343(88)90017-9.

Kiørboe, T., Møhlenberg, F., Riisgård, H.U., 1985. In situ feeding rates of planktonic copepods: a comparison of four methods. *J. exp. mar. Biol. Ecol., 88,* 67-81. doi: 10.1016/0022-0981(85)90202-3.

Knauer, G.A., Martin, J.H., Bruland, K.W., 1979. Fluxes of particulate carbon, nitrogen, and phosphorus in the upper water column of the northeast Pacific. *Deep-Sea Research Part A. Oceanogr. Res. Papers, 26(1)*, 97-108. doi: 10.1016/0198-0149(79)90089-x.

Kolmogorov, A. N., 1962. A refinement of previous hypotheses concerning the local structure of turbulence in a viscous incompressible fluid at high Reynolds number. *Journal of Fluid Mechanics*, *13*(01), 82-85. doi: 10.1017/s0022112062000518.

Koszalka, I., Bracco, A., Pasquero, C., Provenzale, A., 2007. Plankton cycles disguised by turbulent advection. *Theoretical population biology*, *72*(1), 1-6. doi: 10.1016/j.tpb.2007.03.007.

Krause, G. H., Weis, E., 1991. Chlorophyll fluorescence and photosynthesis: the basics. *Annual review of plant biology*, *42*(1), 313-349. doi: 10.1146/annurev.pp.42.060191.001525.

Kruskopf, M., Flynn, K.J., 2006. Chlorophyll content and fluorescence responses cannot be used to gauge reliably phytoplankton biomass, nutrient status or growth rate. *New Phytologist*, *169*(3), 525-536. doi: 10.1111/j.1469-8137.2005.01601.x.

Kunze, E., Sanford, T.B., 1984. Observations of near-inertial waves in a front. *Journal of physical oceanography*, *14*(3), 566-581. doi: 10.1175/1520-0485(1984)014<0566:OONIWI>2.0.CO;2.

LaCasce, J. H., 2008. Statistics from Lagrangian observations. *Progress in Oceanography*, *77*(1), 1-29. doi: 10.1016/j.pocean.2008.02.002.

Landry, M.R., Hassett, R.P., 1982. Estimating the Grazing Impact of Marine Micro-zooplankton. *Marine Biology, 67,* 283-288. doi: 10.1007/BF00397668.

Landry, M. R., Ohman, M.D., Goericke, R., Stukel, M.R., Tsyrklevich, K., 2009. Lagrangian studies of phytoplankton growth and grazing relationships in a coastal upwelling ecosystem off Southern California. *Progress in Oceanography*, *83*(1), 208-216. doi: 10.1016/j.pocean.2009.07.026.

Law, C. S., Watson, A.J., Liddicoat, M.I., Stanton, T., 1998. Sulphur hexafluoride as a tracer of biogeochemical and physical processes in an open-ocean iron fertilisation experiment. *Deep-Sea Research Part II*, *45*(6), 977-994. doi: 10.1016/s0967-0645(98)00022-8.

Le Traon, P. Y., 1990. A method for optimal analysis of fields with spatially variable mean. *Journal of Geophysical Research: Oceans (1978–2012)*, *95*(C8), 13543-13547. doi: 10.1029/jc095ic08p13543.

Lehahn, Y., d'Ovidio, F., Lévy, M., Heifetz, E., 2007. Stirring of the northeast Atlantic spring bloom: A Lagrangian analysis based on multisatellite data. *Journal of Geophysical Research: Oceans (1978–2012)*, *112*(C8). doi: 10.1029/2006jc003927.

Lett, C., Verley, P., Mullon, C., Parada, C., Brochier, T., Penven, P., Blanke, B., 2008. A Lagrangian tool for modelling ichthyoplankton dynamics. *Environmental Modelling & Software*, *23*(9), 1210-1214. doi: 10.1016/j.envsoft.2008.02.005.

Li, Q. P., Franks, P.J.S., Landry, M.R., 2011. Microzooplankton grazing dynamics:-parameterizing grazing models with dilution experiment data from the California Current Ecosystem. *Marine Ecology Progress Series*, *438*, 59-69. doi: 10.3354/meps09320.

Li, Q. P., Franks, P.J.S., Landry, M.R., Goericke, R., Taylor, A.G., 2010. Modeling phytoplankton growth rates and chlorophyll to carbon ratios in California coastal and pelagic ecosystems. *Journal of Geophysical Research: Biogeosciences (2005–2012)*, *115*(G4). doi: 10.1029/2009jg001111.

Li, Q. P., Hansell, D.A., McGillicuddy, D.J., Bates, N.R., Johnson, R.J., 2008. Tracer-based assessment of the origin and biogeochemical transformation of a cyclonic eddy in the Sargasso Sea. *Journal of Geophysical Research: Oceans (1978–2012)*, *113*(C10). doi: 10.1029/2008jc004840.

Lueck, R. G., Picklo, J.J., 1990. Thermal inertia of conductivity cells: Observations with a Sea-Bird cell. *Journal of Atmospheric and Oceanic Technology*, *7*(5), 756-768. doi: 10.1175/1520-0426(1990)007<0756:TIOCCO>2.0.CO;2.

MacIsaac, J. J., Dugdale, R.C., Barber, R.T., Blasco, D., Packard, T.T., 1985. Primary production cycle in an upwelling center. *Deep Sea Research Part A. Oceanographic Research Papers*, *32*(5), 503-529. doi: 10.1016/0198-0149(85)90042-1.

Mackas, D., Bohrer, R., 1976. Fluorescence analysis of zooplankton gut contents and an investigation of diel feeding patterns. *J. exp. mar. Biol. Ecol., 25,* 77-85. doi: 10.1016/0022-0981(76)90077-0.

Martin, A. P., 2003.. Phytoplankton patchiness: the role of lateral stirring and mixing. *Progress in Oceanography*, *57*(2), 125-174. doi: 10.1016/s0079-6611(03)00085-5.

Martz, T. R., Connery, J.G., Johnson, K.S., 2010. Testing the Honeywell Durafet® for seawater pH applications. *Limnol Oceanogr Methods*, *8*, 172-184. doi: 10.4319/lom.2010.8.172.

McWilliams, J. C., Fox-Kemper, B., 2013. Oceanic wave-balanced surface fronts and filaments. *Journal of Fluid Mechanics*, *730*, 464-490. doi: 10.1017/jfm.2013.348.

Methven, J., Arnold, S.R., O'Connor, F.M., Barjat, H., Dewey, K., Kent, J., Brough, N., 2003. Estimating photochemically produced ozone throughout a domain using flight data and a Lagrangian model. *Journal of Geophysical Research: Atmospheres (1984–2012)*, *108*(D9). doi: 10.1029/2002jd002955.

Molcard, A., Piterbarg, L.I., Griffa, A., Özgökmen, T.M., Mariano, A.J., 2003. Assimilation of drifter observations for the reconstruction of the Eulerian circulation field. *Journal of Geophysical Research: Oceans (1978–2012)*, *108*(C3). doi:10.1029/2001JC001240.

Müller, P., Li, X.P., Niyogi, K.K., 2001. Non-photochemical quenching. A response to excess light energy. *Plant Physiology*, *125*(4), 1558-1566. doi: 10.1104/pp.125.4.1558.

Nilsson, E. D., Leck, C., 2002. A pseudo-Lagrangian study of the sulfur budget in the remote Arctic marine boundary layer. *Tellus B*, *54*(3), 213-230. doi: 10.3402/tellusb.v54i3.16662.

Pallàs-Sanz, E., Johnston, T.M.S., Rudnick, D.L., 2010. Frontal dynamics in a California Current System shallow front: 1. Frontal processes and tracer structure. *Journal of Geophysical Research: Oceans (1978–2012)*, *115*(C12). doi: 10.1029/2009jc006032.

Powell, T. M., Okubo, A., 1994. Turbulence, diffusion and patchiness in the sea. *Philosophical Transactions of the Royal Society of London. Series B: Biological Sciences*, *343*(1303), 11-18. doi: 10.1098/rstb.1994.0002.

Rixen, M., Allen, J.T., Alderson, S., Cornell, V., Crisp, N., Fielding, S., … Beckers, J.M., 2003. Along or across front survey strategy? An operational example at an unstable front. *Geophysical research letters*, *30*(1), 17-1. doi: 10.1029/2002gl015341.

Rixen, M., Beckers, J.M., Allen, J.T., 2001. Diagnosis of vertical velocities with the QG Omega equation: a relocation method to obtain pseudo-synoptic data sets. *Deep Sea Research Part I: Oceanographic Research Papers*, *48*(6), 1347-1373. doi: 10.1016/s0967-0637(00)00085-6.

Rudnick, D. L., 1996. Intensive surveys of the Azores Front: 2. Inferring the geostrophic and vertical velocity fields. *Journal of Geophysical Research: Oceans (1978–2012)*, *101*(C7), 16291-16303. doi: 10.1029/96jc01144.

Rudnick, D. L., Luyten, J.R., 1996. Intensive surveys of the Azores Front: 1. Tracers and dynamics. *Journal of Geophysical Research: Oceans (1978–2012)*, *101*(C1), 923-939. doi: 10.1029/95jc02867.

Shepard, D.,1968. A two-dimensional interpolation function for irregularly-spaced data. In *Proceedings of the 1968 23rd ACM national conference* (pp. 517-524). ACM. doi: 10.1145/800186.810616.

Spaulding, R. S., DeGrandpre, M.D., Beck, J.C., Hart, R.D., Peterson, B., De Carlo, E.H., … Hammar, T.R., 2014. Autonomous in situ measurements of seawater alkalinity. *Environmental science & technology*, *48*(16), 9573-9581. doi: 10.1021/es501615x.

Strub, P. T., Kosro, P.M., Huyer, A., 1991. The nature of the cold filaments in the California Current System. *Journal of Geophysical Research: Oceans (1978–2012)*, *96*(C8), 14743-14768. doi: 10.1029/91jc01024.

Sutton, R. T., Maclean, H., Swinbank, R., O'Neill, A., Taylor, F.W., 1994. High-resolution stratospheric tracer fields estimated from satellite observations using Lagrangian trajectory calculations. *Journal of the atmospheric sciences*, *51*(20), 2995-3005. doi: 10.1175/1520-0469(1994)051<2995:HRSTFE>2.0.CO;2.

Taylor, J. A., 1992. A global three-dimensional Lagrangian tracer transport modelling study of the sources and sinks of nitrous oxide. *Mathematics and computers in simulation*, *33*(5), 597-602. doi: 10.1016/0378-4754(92)90157-c.

Viúdez, Á., Haney, R.L., Allen, J.T., 2000. A study of the balance of horizontal momentum in a vertical shearing current. *Journal of Physical Oceanography*, *30*(3), 572-589. doi: 10.1175/1520-0485(2000)030<0572:ASOTBO>2.0.CO;2.

Whitt, D. B., Thomas, L.N., 2013. Near-inertial waves in strongly baroclinic currents. *Journal of Physical Oceanography*, *43*(4), 706-725. doi: 10.1175/JPO-D-12-0132.1.

Wilkerson, F. P., Dugdale, R.C., 1987. The use of large shipboard barrels and drifters to study the effects of coastal upwelling on phytoplankton dynamics. *Limnology and Oceanography*, *32*(2), 368-382. doi: 10.4319/lo.1987.32.2.0368.

Yamazaki, H., Lueck, R., 1990. Why oceanic dissipation rates are not lognormal. *Journal of physical oceanography*, *20*(12), 1907-1918. doi: 10.1175/1520-0485(1990)020<1907:WODRAN>2.0.CO;2.

Chapter 3.

Fine-Scale Vertical and Horizontal Layers of Salinity and Chlorophyll-a Fluorescence at a Front: Formation by Cross-Frontal Vertical Shear

Abstract

Fine-scale vertical structuring of phytoplankton communities has significant consequences for the marine food web, from altering the phytoplankton exposure of surface light and limiting nutrients to influencing the foraging of zooplankton. Hence, it is important to identify fine-scale features and determine their underlying dynamics. We present evidence of fine-scale vertical features in salinity and chlorophyll-*a* fluorescence at a front west of Point Conception, California. The salinity gradients were density-compensated, slanting at a slope different than the isopycnals, diagnostic of formation via shearing of pre-existing patches. The scales and angles of the resultant layers suggests formation through cross-frontal vertical shear due to an ageostrophic secondary circulation (ASC) cell, flowing in a direction consistent with forcing due to frontogenesis. Using remote sensing data, we identify the most likely source of frontogenetic forcing upstream, and using scaling arguments estimate the horizontal extent of the original salinity and Chl-*a* patches. These results highlight how pre-existing horizontal biological gradients can be transformed into fine-scale vertical structure at a front. This mechanism provides a source of biological variability within a front that should be explored in future studies.

3.1. Introduction

Surface ocean fronts are regions of enhanced physical and biological gradients and properties. Studies of plankton at fronts often focus on responses of the planktonic ecosystem to bottom-up control through vertical exchanges of biomass and nutrients [*Strass*, 1992; *Lévy et al.*, 2001; *Li et al.*, 2012; *Spall and Richards*, 2000; *Zakardjian and Prieur*, 1998; *Oguz et al.*, 2014; *Nagai et al.*, 2008]. In addition to directly impacting the ecosystem via nutrient or light availability, fronts play a role in structuring the spatial distribution of planktonic organisms through kinematic mechanisms. First, the presence of a strong horizontal density gradient and the associated geostrophic current acts as a barrier, enhancing diversity [*d'Ovidio et al.,* 2010]. Additionally, geostrophic shear present at fronts has been implicated in the dynamics of thin layers [*Johnston et al.,* 2009]. The altered biological distributions and gradients arising from these motions will have important consequences for the dynamics of all the trophic levels that depend upon phytoplankton for sustenance.

Physical dynamics at fronts are governed by the front's density structure; a front's subsequent evolution involves the interplay between the density and forcing. One curious aspect of seawater density, however, is its nonlinear equation of state: salinity and temperature can counter each other's contribution to density, called compensation, resulting in a uniform density with different hydrographic (temperature and salinity) characteristics. It is important to note, additionally, that salinity-temperature compensation occurs with a linearized equation of state Essentially, these density-compensated gradients in salinity and temperature are invisible for most dynamical considerations at a front [though see *Hosegood et al.*, 2006]. Compensation of density has

been widely observed in the ocean [*Roden*, 1977; *Yuan and Talley*, 1992; *Arhan*, 1990]; compensated gradients in salinity and temperature can persist for longer timescales than equivalent gradients in density before diffusing [*Chen and Young*, 1995]. Passive tracers, such as nutrients or phytoplankton, can likewise maintain gradients for extended periods of time before the gradients are dissipated. Therefore, one would expect to find enhanced variability in nutrients, phytoplankton, salinity and temperature at smaller spatial scales than variability in density [*Ferrari and Rudnick*, 2000; *Klein et al.*, 1998].

In this study, we present observational evidence of small-scale vertical and horizontal structure forming layers in two tracers at a front: salinity and chlorophyll-*a* (Chl-*a*) fluorescence. While the presence of small-scale variability is not novel, we find that the nature of the tracer distribution is diagnostic of a mechanism of layer formation not usually examined in the context of fronts: vertical cross-frontal shear. The paper is structured as follows: section 2 describes the observational context and methodology of collecting the data used in this study. Section 3 describes the spatial distributions of our tracer data, identifying persistent layers, and hypothesizing some mechanisms that may be responsible for their characteristics. Section 4 estimates the magnitude, source, and plausibility of the hypothesized mechanism: frontogenesis. Section 5 concludes this study with speculation concerning this mechanism's biological consequences.

3.2. Data

3.2.1 Sampling plan and context

The data used in this study come from the 2012 process cruise (P1208), dubbed "E-Front", of the NSF-funded California Current Ecosystem (CCE) Long Term

Ecological Research (LTER) program conducted from July to August aboard the *R/V Melville*. The cruise's main objectives were to identify regions of enhanced horizontal physical and biological gradients (i.e., fronts) and quantify their role in structuring the pelagic ecosystem. The study area was roughly inside a 1°x1° box, centered near 34.3° N and 122.5° W. For the entire cruise, a frontal region existed in the vicinity of two mesoscale features: cyclonic to the southeast, and anticyclonic to the west, as indicated by Aviso satellite sea surface height data (Figure 3.1). The chronology of the cruise was as follows: an initial SeaSoar [*Pollard,* 1986] survey was conducted in a radiator pattern from 30 July to 3 August, going south to north, opposing the geostrophic jet. Subsequent to this survey, four Conductivity-Temperature-Depth (CTD) front crossings were conducted by a Moving Vessel Profiler (MVP: *Ohman et al.*, [2012]) focused around the frontal region over the course of 15 hours. The four transects were followed by biological sampling and hydrographic surveys for the rest of the cruise, including overnight transects and multi-day experimental cycles, similar to *Landry et al.* [2009].

3.2.2 MVP CTD data and Geostrophic Currents

The majority of the data presented here derive from the MVP CTD surveys conducted prior to the first overnight front crossing. The MVP vehicle samples vertically by freewheeling the synthetic cable attached to the MVP fish, allowing for a near-vertical descent at ~ 4 m/s. At a prescribed depth (here ~ 200 dbar), the brake is applied to the computer-controlled winch and the fish automatically winched back to the surface. Only down-casts are used in this dataset. Onboard the fish is a rapid response AML Micro conductivity sensor, thermistor, Chl-*a* fluorometer, and laser optical particle counter

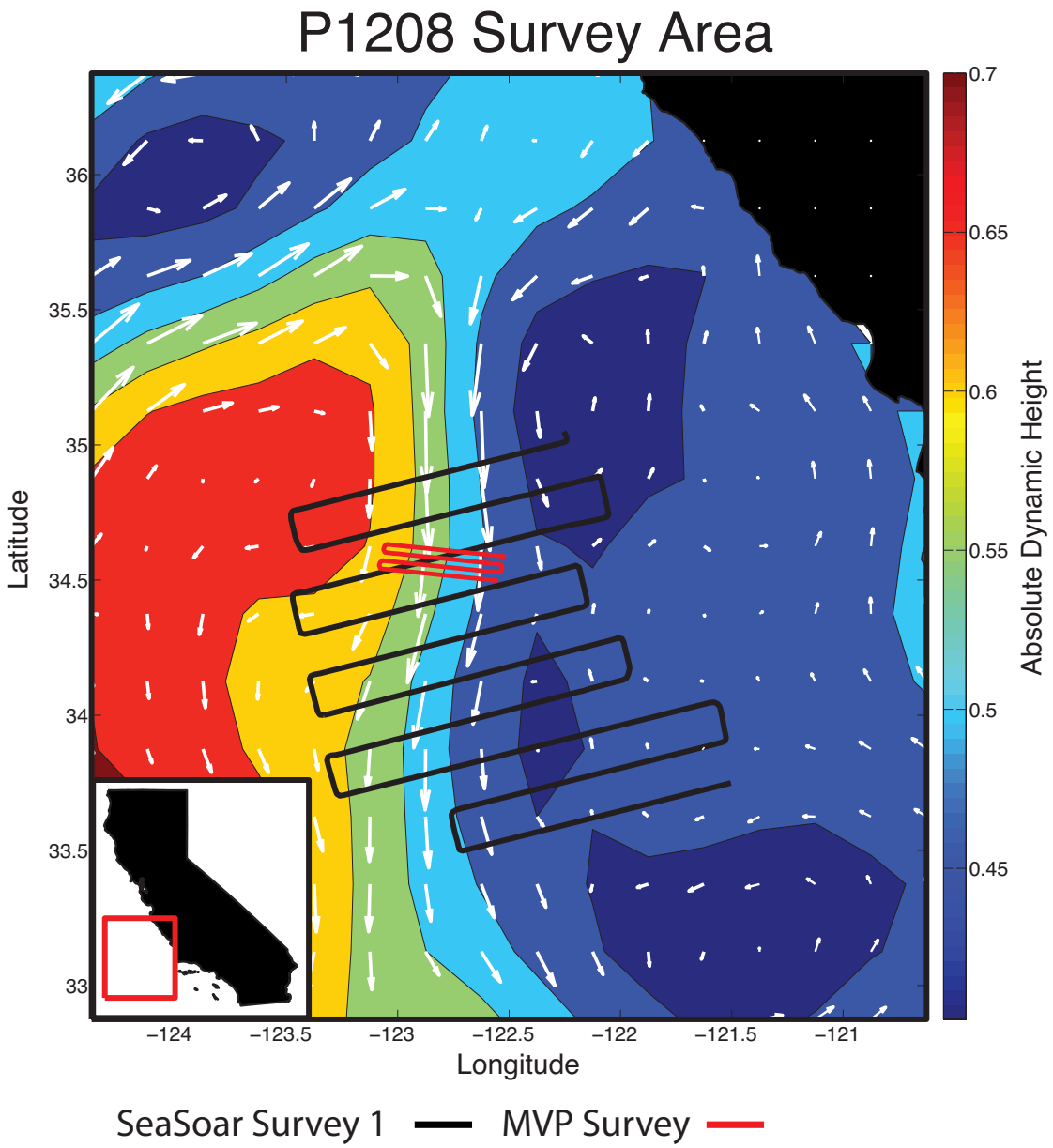

Figure 3.1. P1208 Process cruise survey region: E-Front. A large-scale SeaSoar survey (black line) was conducted July 30 to August 3 2012 in a frontal region. Four transects from an MVP survey (red line) were conducted August 4 to August 5. Contours are absolute dynamic height, and white arrows are geostrophic currents calculated from AVISO data. Black regions indicate the coast of central California. The inset shows the location of the sampling region relative to the California coast.

(LOPC). The conductivity and temperature data were lag-corrected to reduce salinity spiking. A previous study utilizing MVP data found an operational threshold binning of ~ 1 m in the vertical [*Li et al.*, 2012]. However, for this study we bin at 3 m as a compromise between resolving small-scale vertical salinity and fluorescence gradients and maintaining a smooth density profile. In order to resolve the horizontal distribution of salinity and Chl-*a* fluorescence, the vertical perturbations of density due to aliased internal waves and other noise must be removed. To achieve this, at each depth density is horizontally smoothed with a moving window of 20 observations, roughly equivalent to 25 km distance in the horizontal. The chosen 25 km length scale is the same as the estimated cross-front autocovariance of density as observed with the SeaSoar data and used for objective mapping, as described in *de Verneil and Franks* [2015]. Vertical profiles of smoothed density are then required to be statically stable using a constrained linear least-squares algorithm (lsqlin in Matlab Release 2012b, The Mathworks, Inc., Natick, Massachusetts, United States). In order to prevent horizontal smoothing of the small-scale signals in salinity and fluorescence, the vertical profiles of both tracers were fit by splines to the unsmoothed density and correspondingly interpolated to the smoothed profile. The Chl-*a* fluorescence is not calibrated or corrected for non-photochemical quenching [*Müller et al.*, 2001]. These limitations prevent us from making quantitative comparisons between fluorescence patches in terms of phytoplankton biomass or population dynamics, an application fraught with its own problems [*Kruskopf and Flynn*, 2006]. Consequently, for the remainder of this study, fluorescence is used qualitatively as a passive tracer to identify structure in the water column; we will focus solely on relative values.

3.3. Evidence of fine structure and possible mechanisms

The MVP transects conducted after the first SeaSoar survey and immediately before the first overnight front crossing contain both fine-scale horizontal and vertical variability in salinity and Chl-*a* fluorescence. Before interpreting the two-dimensional distribution of these tracers, we first consider the one-dimensional perspective provided by individual CTD casts. Subsequently, we describe the two-dimensional gradients present in E-Front, and provide hypotheses for the formation of the fine-scale layers observed at the front.

3.3.1 Vertical variability of salinity and fluorescence in E-Front

Many vertical profiles in our dataset contain sub-surface minima and maxima of both fluorescence and salinity (e.g., Figure 3.2). The density increases monotonically with depth, consistent with a stable profile. The salinity profile, however, contains multiple maxima in the upper 60 m of the water column. Initially, salinity increases to a maximum of 33.6 at 30 m, then drops to a minimum of ~33.3 at 45 m. Subsequently, the salinity then increases again to a local maximum of 33.7 at 55 m, prior to another minimum of 33.5 just below 60 m. Below 60 m, salinity increases, indicating the transition into a halocline at depth, also mirrored by the increase in density. Again, the monotonic increase of density in the presence of these large salinity variations reflects salinity-temperature compensation of density near the surface. The profile of Chl-*a* fluorescence likewise has multiple maxima and minima in the upper 60 m. The near-surface maximum is slightly shallower than the shallow salinity maximum, at ~15 m, although the gradient of decreasing fluorescence at 30 m is similar to the salinity profile.

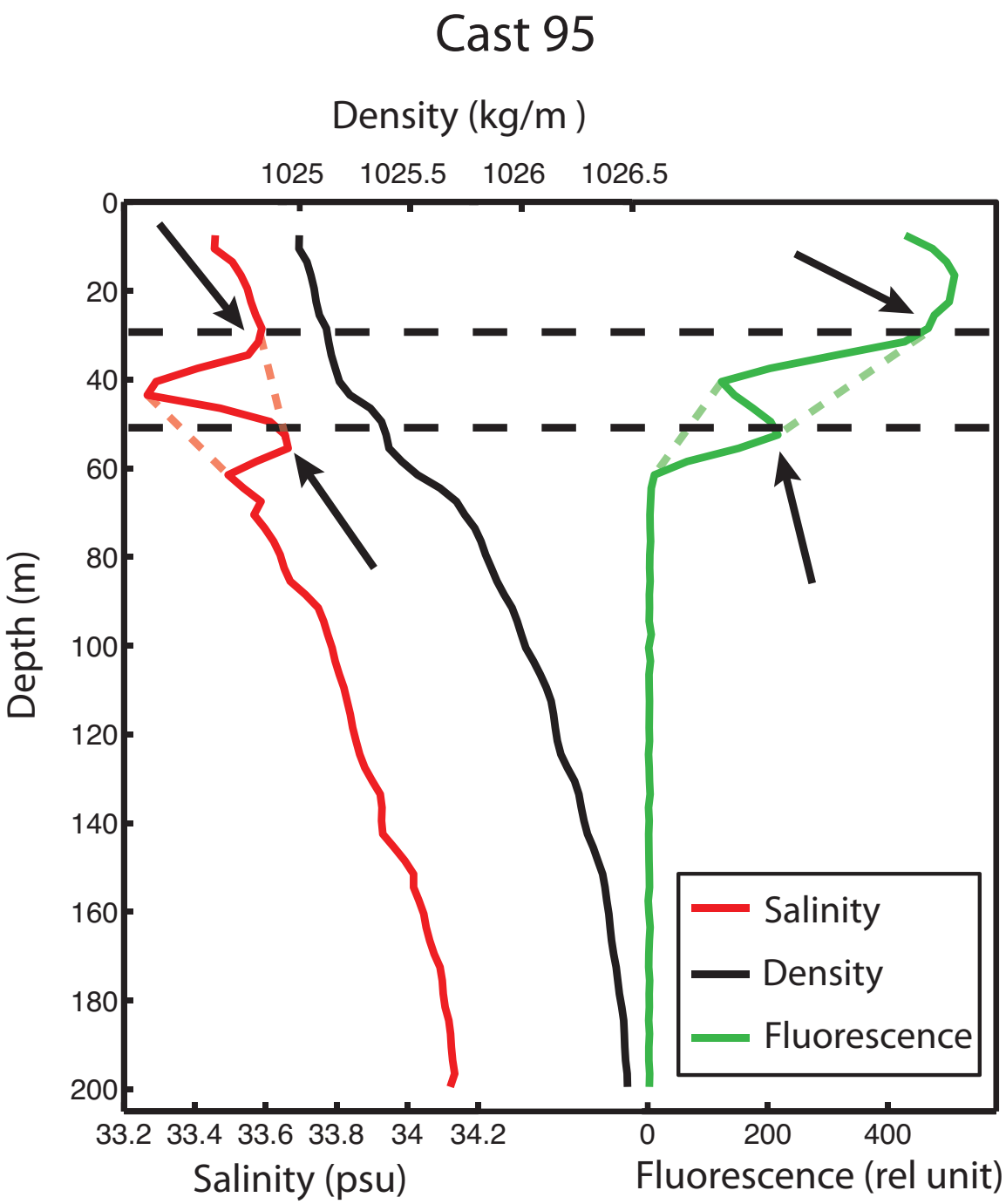

Figure 3.2. Profiles of salinity, density, and chlorophyll-*a* fluorescence from an MVP cast in the front. Arrows point to maxima in salinity and fluorescence. Black dashed lines indicate the depths of the maxima. Dashed red and green lines connect the maxima and minima of salinity and fluorescence, respectively, to demonstrate the implied water mass characteristics.

The minimum value at 40 m is close to the salinity minimum at 45 m, with another maximum at 50 m before dropping to noise levels below 60 m.

Taken as an individual observation, there are a number of conclusions that one can make from this cast. First, one can visually connect the two salinity maxima in the vertical profile (dashed lines in Figure 3.2), noticing that the deeper maximum has a larger salinity value, and thus may make a plausible continuous salinity gradient if the salinity minimum were not present. Fluorescence could also monotonically decrease by connecting the two regions of elevated fluorescence. Therefore, one may conclude that there are two water masses present in the upper 60 m, one characterized by high salinity and fluorescence (HSC), and the other described by low salinity and fluorescence. The salinity gradient below 60 m is more consistent with a continuation of the low salinity water mass, indicating that the HSC water is the anomalous feature in this profile.

The fluorescence-salinity relationship present in HSC water is consistent with properties of the survey region. The California coast is well known to undergo wind-driven coastal upwelling, which brings dense, salty water rich with nutrients to the surface, stimulating phytoplankton growth [*Huyer*, 1983; *Hickey*, 1979; *Di Lorenzo*, 2003; *Marchesiello et al.*, 2003]. The phenomenology of coastal upwelling thus provides likely source of the HSC relationship. Additionally, observational and modeling studies of the California current find that HSC features, initially formed at the coast, subsequently evolve on their own, often advecting productive water with enhanced biomass offshore within filaments or eddies [*Hood et al.*, 1991; *Washburn et al.*, 1991; *Chenillat et al.*, 2015; *Nagai et al.*, 2015). This would explain how HSC water is anomalous in the profile: salty, productive water from the coast is subsequently advected

offshore, impinging on the less salty, oligotrophic water characteristic of the offshore California Current.

The vertical profile shows layers of these two water masses alternately stacked upon one another. The question is how such layers may have formed, and how they may affect the local plankton dynamics. Are these layers indicative of water intrusions? Or, considering this is a single cast, should variability in these layers be considered anomalous, or perhaps spurious and ignored? We can answer these questions by exploring the two-dimensional (cross-front, depth) distribution of our two tracers, salinity and fluorescence.

3.3.2 Two-dimensional salinity and fluorescence variability

The horizontal and vertical distribution of salinity and fluorescence during the four cross-front MVP transects (Figure 3.3) shows that the large-scale horizontal gradient in salinity reflects what we inferred from the single cast: the HSC water is indicative of coastal, perhaps recently upwelled water. Offshore, the salinity decreases, with an additional mid-water salinity minimum. The highest fluorescence values, as well as the presence of salinity and fluorescence layers, are concentrated in the region where the 1025 kg m^{-3} isopycnal reaches closest to the surface.

In the frontal region where the 1025 isopycnal comes closest to the surface, two regions of enhanced fluorescence can be seen near the surface. Two tongues of high-fluorescence water extend down from these maxima toward the less-dense side of the front (Figure 3.3 b, f, j, n). These tongues are coincident with tongues of high-salinity

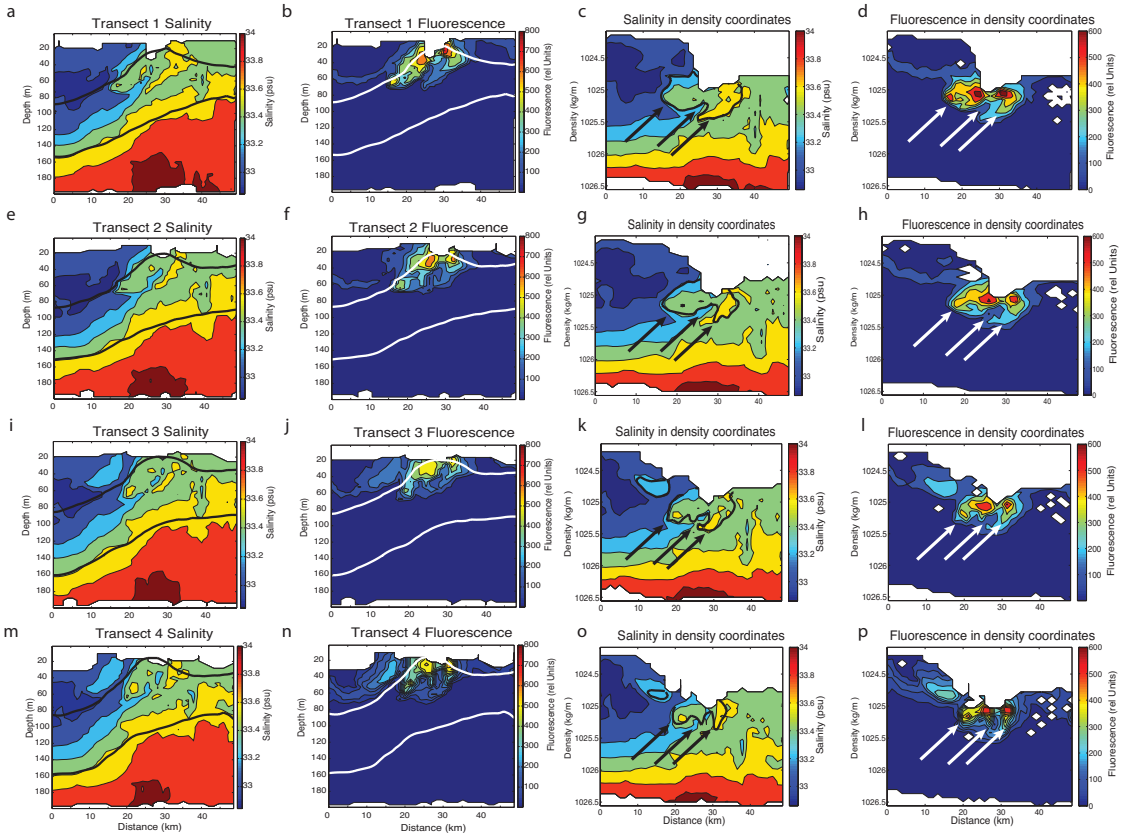

Figure 3.3. MVP transects of salinity (left column; panels a,e,i,m) and Chl-*a* fluorescence (second column; panels b,f,j,n) in physical coordinates. Contour lines are 1025 and 1026 kg m^{-3} isopycnals, black in the salinity plots, white in the fluorescence plots. The right two columns display the same data in density coordinates with salinity in panels c,g,k,o, and fluorescence in d,h,l,p. Arrows highlight regions of layering. Fluorescence contours are displayed in black on the salinity panels c,g,k, and o.

water (Figure 3.3a, e, i, m). These tongues form the layers that appear as fine-structure maxima in the vertical profiles (Figure 3.2).

The layers within the filament show a consistent orientation. All the layers are slanted, with the layer presenting itself at shallow depths inshore, deepening as one moves offshore across the feature. Using the 33.4 and 33.6 salinity contours, along with fluorescence contours of 200 and 400 relative units, we find the median thickness and cross-front width of the subsurface layers to be 15 m and 4 km, respectively. Aggregating

the patches present in the MVP E-Front dataset, we arrive at an average layer slope of 5 m per km, with most layers spanning a total of ~ 5 km horizontally and 25 m vertically (Figure 3.4). We note that the 3 m binning resolution was used here to identify the tracer patches within the water column. To use these data to calculate dynamically relevant quantities such as density gradients requires smoothing and objective mapping to remove aliased phenomena such as internal waves [*Rudnick*, 1996]. Such smoothing and mapping will often remove the small-scale features we explore here. Indeed, processing the E-Front SeaSoar survey data in the typical fashion (coarse binning followed by objective mapping) results in smooth, well-behaved distributions that, while reflecting the large-scale horizontal gradients present, do not contain the fine-scale vertical fluorescence and salinity structures observed in the MVP data.

3.3.3 Possible mechanisms of formation

3.3.3.1 Internal Waves and Mixing

The fact that these layers tilt across a range of density values also precludes linear internal waves as a formation mechanism: internal waves would influence isopycnal layer thickness and spatial distribution. However, we removed these effects by smoothing the horizontal density distribution, and the effects of internal waves would disappear when plotting fluorescence and salinity in isopycnal coordinates. As seen in Figure 3.3, the layers are still distinct in isopycnal coordinates, extending downward across the front and across isopycnals, toward denser water. Thus these layers were unlikely to have been formed by internal waves.

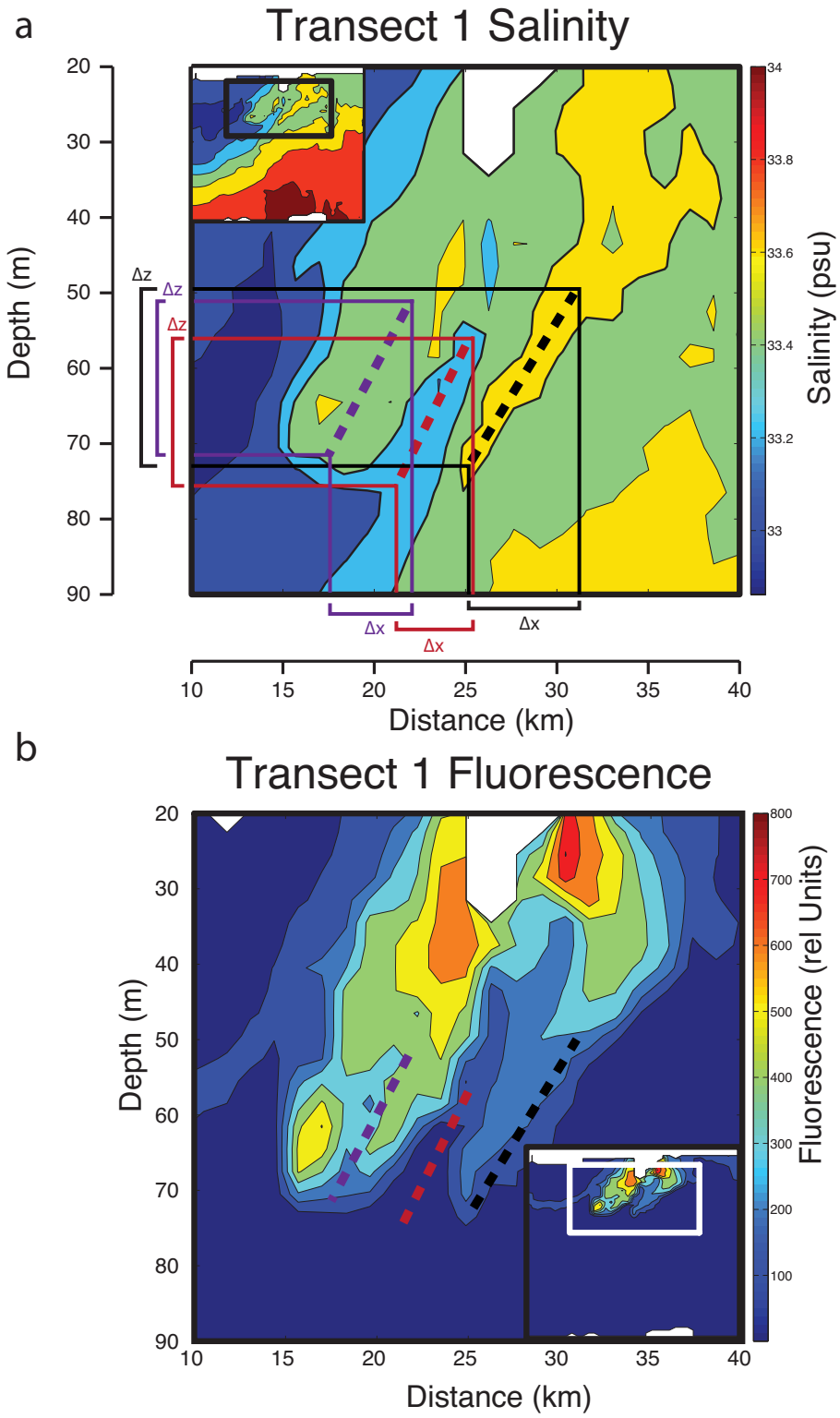

Figure 3.4. Transect 1 salinity (a) and fluorescence (b), zoomed in from the full transect (insets). Dashed lines indicate orientation of alternating layers, with solid lines marking the vertical and horizontal scales of the patches.

Diabatic (across-isopycnal) processes in the water column (i.e., friction, diffusion, and mixing) could not have formed these layers, as such processes would tend to destroy the gradients in salinity and fluorescence rather than enhance the vertical structure. Therefore, we conclude that the observed gradients in salinity and fluorescence are due to pre-existing horizontal heterogeneity that was subsequently altered by water motions at the front.

3.3.3.2 Cross-frontal Shear

After rejecting local water mass intrusion and internal waves, we now search for alternate explanations for the spatial structure of the HSC water patches. As previously mentioned, the HSC patches, when viewed in density coordinates, span a range of isopycnals. The slanting of these patches seen in physical coordinates is also preserved when viewed in density coordinates. This consistent tilting of horizontal gradients across isopycnals is diagnostic of shear-driven layering, in our case acting upon tracers oriented across a front [*Franks*, 1995; *Birch et al.*, 2008; *Durham and Stocker*, 2012].

The hypothesized shearing mechanism would act as follows: an initial patch with a finite horizontal scale is formed at the front (Figure 3.5). This patch extends vertically, crossing isopycnals. A vertical shear of the cross-frontal velocities would move different depths of the initial patch different distances across the front, stretching the patch and tilting it [e.g., *Franks*, 1995; *Birch et al.*, 2008] as the bottom of the patch moves across the front relative to the top of the patch. This cross-frontal stretching and tilting would lead to the presence of layers in vertical profiles; the layers should be contiguous, but angle across isopycnals – just as we observe in our HSC layers.

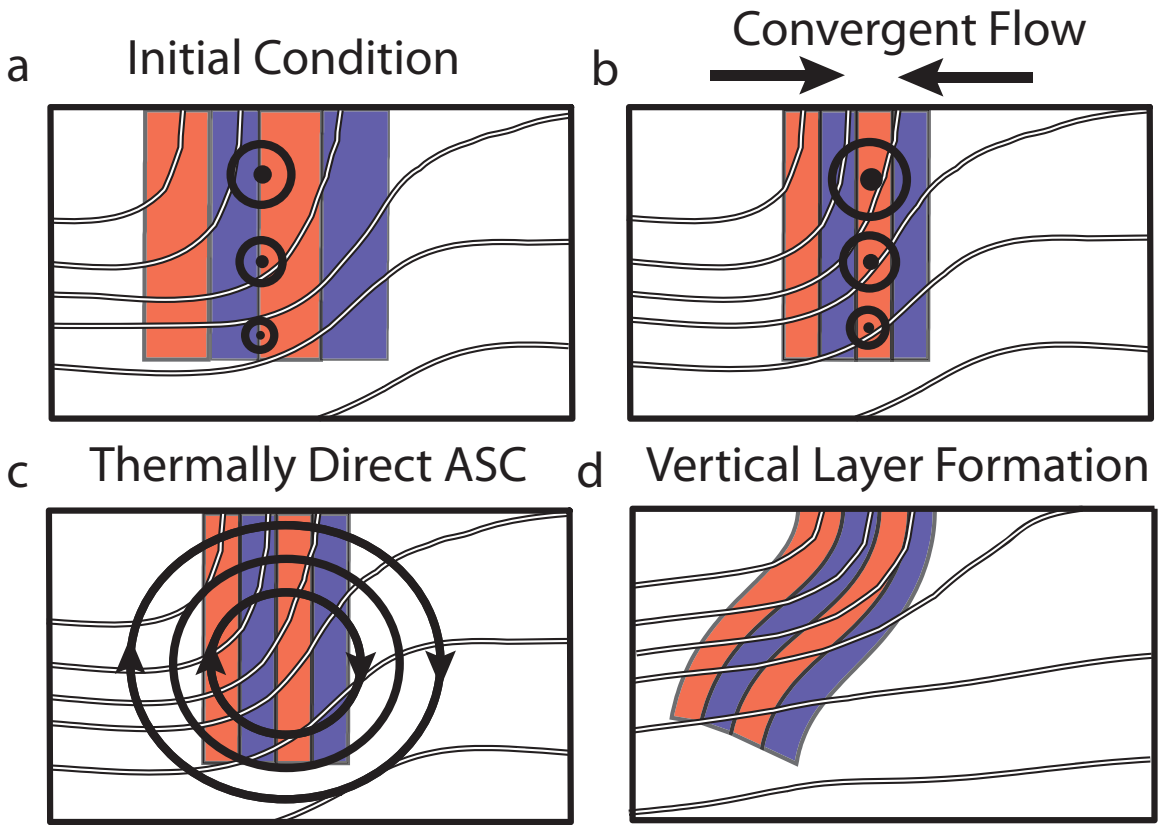

Figure 3.5. Hypothesized cross-frontal layer generation. (a) Vertical patches (red and blue boxes) exist within a weak front. (b) Large-scale convergence squeezes the patches and accelerates the geostrophic current coming out of the page (black circles), tilting the isopycnals upward (white/black lines). (c) The accelerated current induces a thermally direct ageostrophic secondary circulation, tending to flatten the isopycnals while also creating a vertical shear (heavy black lines). (d) Patches in the front tilted and stretched by the ASC now slant horizontally, creating vertical structure and layers from the initial horizontal gradients.

Shear as a mechanism of vertical layer formation is not a novel concept; in the context of a front, however, usually the vertical shear *along* the front due to geostrophic currents is first considered [*Johnston et al.*, 2009]. In this case, we search for a mechanism of vertical shear *across* the front at E-Front that could generate this vertical fine structure from pre-existing cross-frontal horizontal gradients.

3.3.4 Cross-front Shear and Ageostrophic Secondary Circulations

Vertical shear across a front is typically explored within the context of ageostrophic secondary circulations (ASC). These motions are induced when an evolving front's geostrophic flow becomes out of geostrophic balance; when this happens, vorticity and mass conservation dictate an adjustment via a cross-frontal circulation cell [*Hoskins*, 1982]. Essentially, water on one side of the front downwells while water on the other side moves upward. Mass balance requires a horizontal ageostrophic velocity to close the circulation pattern. If a cell downwells water on the dense side of a front and upwells on the less-dense side, it forces the isopycnals to be more horizontal. This kind of ASC is termed "thermally direct" (heavy water goes down, light goes up). The reverse process (steepening isopycnals) is considered thermally indirect. The kind of ASC induced by a given frontal adjustment is usually explored using the quasi-geostrophic or semi-geostrophic omega equations [*Hoskins et al.*, 1978; *Hoskins*, 1975]. In a pragmatic sense, if a front intensifies (frontogenesis), a thermally direct ASC develops to counteract it, forcing isopycnals to slightly flatten. The reverse happens when a front's horizontal density gradients are spread apart (frontolysis). Additionally, the meandering of a geostrophic current will create ASC's. A deviation to the left relative to the geostrophic current (cyclonic perturbation) will induce a flattening of isopycnals, while a deviation to the right (anticyclonic perturbation) will sharpen them [*Cushman-Roisin and Beckers*, 2011]. Both these forms of forcing (intensification of density gradients via frontogenesis and meandering currents) are reversible. Other forcing, such as wind-driven Ekman transport, can also influence ASC's, though irreversibly. As one might expect, a down-front wind steepens isopycnals, and conversely flattens them for up-front winds [*Pallás-*

Sanz et al., 2010]. Sufficient down-front wind forcing can contribute to frontogenesis, and create multiple ASC's [*Thomas and Lee*, 2005]. The hallmark of this form of frontogenesis due to down-front wind forcing is negative potential vorticity and subsequent convective mixing. Since the wind-driven frontogenesis in *Thomas and Lee* [2005] creates mixing, and thus removes the observed HSC gradients, it is not a candidate in this study.

In the E-Front MVP transects, the orientation of the HSC layers is consistent with a circulation that was flattening the isopycnals at the front: a thermally direct ASC. Therefore, we can rule out a few of the potential mechanisms. While the MVP transect is located near a slight anticyclonic bend in the front (as determined by the first SeaSoar survey), this is the wrong direction to account for the observed tracer pattern. Also, satellite altimetry suggests a largely straight geostrophic current in the region to the North of our surveys (Figure 3.1). In addition, shipboard wind data (not shown) indicate a steady North-Northwesterly wind throughout the cruise, indicating a mostly down-front wind, which would also induce an ASC inconsistent with the orientation of the layers; we do not consider wind further in this study. As a result, we focus on the generation of a thermally direct ASC through frontogenesis. A frontogenetic ASC would stretch and deform tracers that were present when the front was formed, generating patterns consistent with the orientation of our HSC patches.

3.4. Diagnosis of Cross-frontal Shear

A simple and well-studied example of frontogenesis arises from the horizontal deformation model of *Hoskins and Bretherton* [1972]. In this two-dimensional model, an

initial density perturbation advects into a region of mesoscale forcing characterized by a strain rate of α (here $u=-\alpha x$ and $v=\alpha y$). As a parcel moves with this flow, it is compressed horizontally in the x (cross-front) direction in an exponential fashion, proportional to α, while being stretched in the y (along front) direction. The strengthening horizontal buoyancy gradients in the x direction induce an acceleration of the geostrophic current, which in turn creates a thermally direct ASC across the front [*Thomas et al.*, 2008; *MacVean and Woods*, 1980; *Bleck et al.*, 1988]. The scaling for the ageostrophic cross-front velocity u_{ag} can be found [*McWilliams et al.*, 2009] from the strain rate α, the Coriolis frequency f, and the along-front geostrophic velocity v_g:

$$v_g \sim \frac{\alpha}{f} u_{ag} \qquad (1)$$

To estimate u_{ag} we use the geostrophic velocities calculated from the first SeaSoar survey and ADCP data from E-Front [*de Verneil and Franks*, 2015]. These data are better constrained to satisfy geostrophy and contain more three dimensional context and observations than the MVP ADCP observations. The difference in timing between the surveys with the SeaSoar and MVP platforms is ~2 days, less than the duration of SeaSoar survey. We therefore assume that the geostrophic velocity did not vary during this timeframe. Using our calculated geostrophic velocity field, we choose a representative velocity of v_g~0.5 m s^{-1} at our feature. We estimate the strain rate α using AVISO absolute dynamic height, which shows the large-scale geostrophic current present in our survey coming from the North (Figure 3.6). The horizontal deformation, $\partial u/\partial x - \partial v/\partial y$, shows a region of large-scale confluence to the North, with a maximum

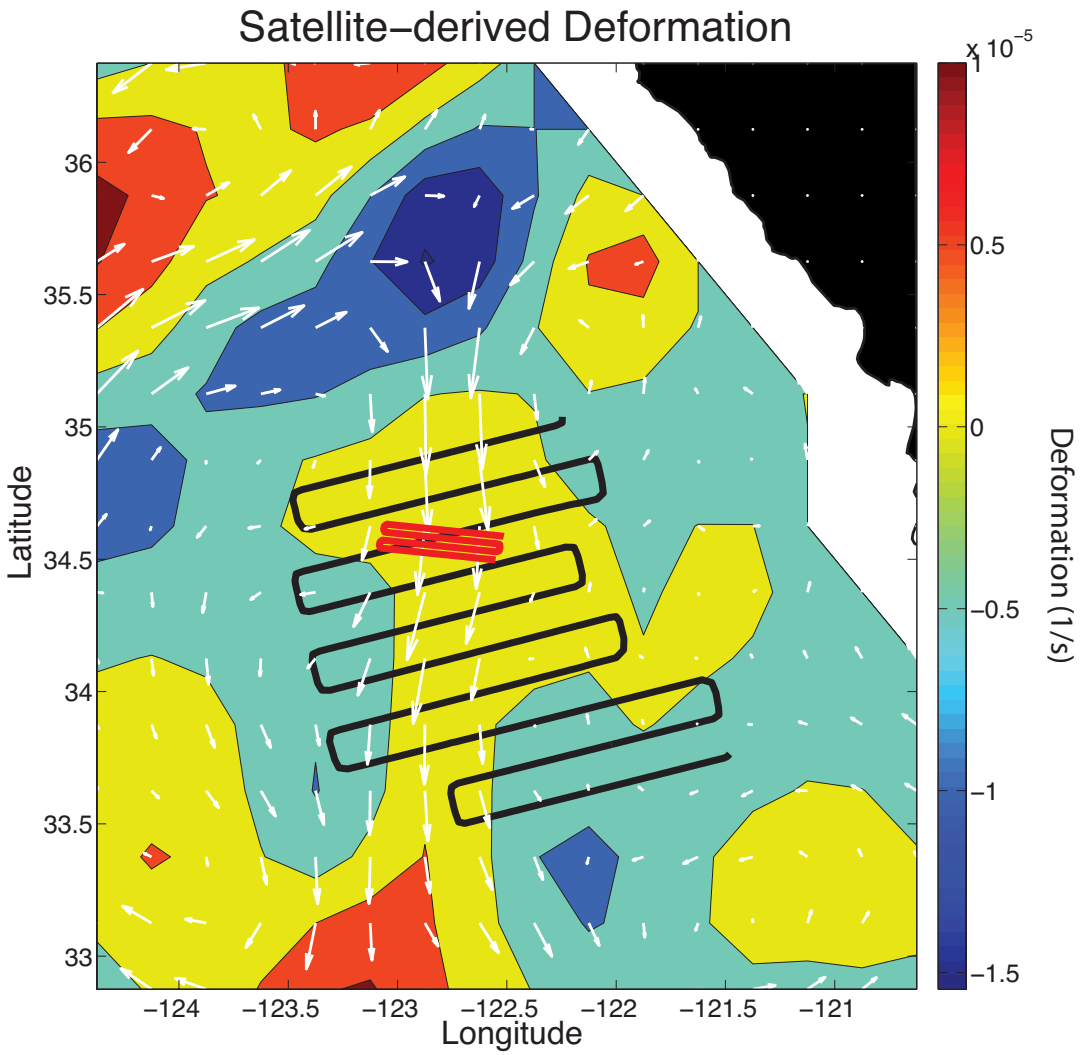

Figure 3.6. Contour plot of horizontal deformation rate (1/s) calculated from geostrophic currents estimated by AVISO absolute dynamic height. Black and red lines and white arrows are survey locations and currents, similar to Figure 1.

deformation rate of $\alpha \sim 7 \times 10^{-6}$ s^{-1}. Using this value for α, and a typical value of 1×10^{-4} s^{-1} for *f*, we get a cross-front velocity ~0.04 m s^{-1} at the climax of frontogenesis.

As reported in Section 3.2, the HSC layers spanned ~5 km horizontally, and ~25 m vertically, with a slope of 5 m per km. If we assume that the cross-frontal ASC extends about 50 m from the surface, with the top moving at 0.04 m s^{-1} in one direction and the bottom moving at the same speed but opposite direction, then the top of a layer of HSC

water at 25 m should remain motionless relative to the waters below at 50 m moving at 0.04 m s^{-1}. If we assume that these tilted layers were vertical when they were formed, the estimated shear would have taken 1.4 days to create the tilted layers. Furthermore, this amount of deformation would suggest that the patches had initial horizontal dimensions of $e^{\alpha t}$, or approximately 2.5 times their final size. Therefore, it seems likely that the HSC patches were at least 12.5 km wide initially, or about the same horizontal scale as the local Rossby radius of deformation.

These calculations must be viewed as qualitative and only accurate to orders of magnitude. As frontogenesis begins, the ageostrophic velocity would not be as strong initially, and would probably take more time to advect a tracer layer than estimated here. Also, the placement of the initial HSC patch in relation to the density field and the intensifying geostrophic current will determine which part of the ASC impacts the patch. For example, if a patch were perfectly placed at the center of the region of confluence, vertically spanning the ensuing ASC, the cross-frontal deformation and layer formation would be maximal. If the patch were offset from the center of confluence, an additional component of vertical velocity would subduct the HSC patch on the dense side of the front, or upwell the patch on the less-dense side of the front. The horizontal velocities on either side would still have a vertical shear that would create a tilted layer distribution similar to our observations. Finally, there is no guarantee that the HSC patch was perfectly vertically oriented as an initial condition. These complications notwithstanding, we believe that cross-frontal shear associated with frontogenesis is the most plausible mechanism for the formation of the layered HSC distributions observed at E-Front.

3.5. Biological Consequences and Conclusions

Our data provide evidence of fine-scale layering in both salinity and Chl-*a* fluorescence at a surface ocean front. These gradients and layers are difficult to detect using standard deployment of sampling platforms and the typical processing of hydrographic data. We conclude that these vertically layered structures in salinity and fluorescence, which extend downward and horizontally from the dense to the less-dense side of the front, reflect cross-frontal shear-driven tilting and stretching of horizontal gradients initially present in the water column as the front was formed. We find that the fine-scale *vertical* layers resulted from cross-frontal vertical shearing of larger-scale *horizontal* features that spanned the entire front. Prior studies of layer formation through shear at a front mainly considered the along-front component of vertical shear. While the vertical shear associated with a geostrophic current will dominate the magnitude of any cross-frontal shear, the cross-frontal shear is clearly also an important factor in structuring hydrographic and phytoplankton distributions at fronts.

After consideration of various mechanisms driving ASC's, we find that frontogenesis due to remote confluence is the most likely source of forcing necessary to recreate our observations. In a two-dimensional framework, phytoplankton patches entering a frontogenetic region will be first compressed horizontally by frontogenesis, reducing the effective cross-frontal area. Subsequently, the vertical shear of the cross-frontal velocities associated with an ASC can expand this cross-frontal area by shearing the patch horizontally, stretching it across the front and forming a thinning layer. The decreased vertical thickness of the layer formed from the initial patch would potentially expose the phytoplankton at the bottom of the layer to different light conditions by

relieving self-shading or changing their depth. Additionally, the increased horizontal extent of the layer will impact the phytoplankton grazers, especially diel vertical migrators that now have an increased probability of encountering the layer due to its increased cross-frontal horizontal extent compared to the original patch.

Along with the horizontal motion that creates vertical cross-front shear, ASC's have a vertical component to their velocity. This aspect of ASC's is what most investigators report; however, the impact of these motions will be altered in the presence of horizontal variability within a front. If a vertical patch of phytoplankton is found on the less dense side of the front, it will create slanting layers while being upwelled. Phytoplankon on the dense side of the front, conversely, will be subducted while creating slanting layers. In this process, these phytoplankton may be moved below the euphotic zone where they will likely die and sink. Thus the shearing/subduction of patches by ASCs could enhance the organic carbon export at the front.

In conclusion, the fine-scale vertical and horizontal layers analyzed in this study underscore the importance of understanding the enhanced biological gradients present at fronts – even those arising from second-order motions that are not oriented vertically. The potential role of frontogenesis-driven cross-frontal shear in structuring the ecological interactions of planktonic ecosystems within a front may be substantial, and should be investigated further.

Acknowledgements

Chapter 3, in part, is currently being prepared for submission for publication of the material. de Verneil, A. ,Franks, P.J.S., Ohman, M.D. Fine-Scale Vertical and Horizontal Layers of Salinity and Chlorophyll-a Fluorescence at a Front: Formation by Cross-Frontal Vertical Shear. Geophysical Research Letters. The dissertation author was the primary investigator and author of this paper.

References

Arhan, M., 1990. The North Atlatnic Current and Subarctic Intermediate Water. Journal of Marine Research 48, 109-144.

Birch, D.A., Young, W.R., Franks, P.J.S., 2008. Thin layers of plankton: Formation by shear and death by diffusion. Deep Sea Research Part I 55 (3) 277-295.

Bleck, R., Onken, R., Woods, J.D., 1988. A two-dimensional model of mesoscale frontogenesis in the ocean. Quarterly Journal of the Royal Meteorological Society 114 (480), 347-371.

Chen, L., Young, W.R., 1995. Density compensated thermohaline gradients and dispycnal fluxes in the mixed layer. Journal of Physical Oceanography 25, 3064-3075.

Chenillat, F., Franks, P.J.S., Rivière, P., Capet, X., Grima, N., Blanke, B., 2015. Plankton dynamics in a cyclonic eddy in the Southern California Current System. Journal of Geophysical Research: Oceans. Online Access. doi: 10.1002/2015JC010826.

Cushman-Roisin, B., Beckers, J.M., 2011. Introduction to Geophysical Fluid Dynamics: Physical and Numerical Aspects (Vol. 101). Academic Press.

de Verneil, A., Franks, P.J.S., 2015. A pseudo-Lagrangian method for remapping ocean biogeochemical tracer data: Calculation of net Chl-*a* growth rates. Journal of Geophysical Research: Oceans 120 Online Access. doi: 10.1002/2015JC01898

Di Lorenzo, E., 2003. Seasonal dynamics of the surface circulation in the Southern California Current System. Deep Sea Research Part II 50 (14),2371-2388.

D'Ovidio, F., De Monte, S., Alvain, S., Dandonneau, Y., Lévy, M., 2010. Fluid dynamical niches of phytoplankton types. Proceedings of the National Academy of Sciences 107 (43), 18366-18370, doi: 10.1073/pnas.1004620107.

Durham, W.M., Stocker, R., 2012. Thin phytoplankton layers: characteristics, mechanisms, and consequences. Annual Review of Marine Science 4, 177-207.

Ferrari, R., Rudnick, D.L., 2000. Thermohaline variability in the upper ocean. Journal of Geophysical Research: Oceans 105 (C7) 16857-16883.

Franks, P.J.S., 1995. Thin layers of phytoplankton: A model of formation by near-inertial wave shear. Deep Sea Research I 42 (1), 75-91.

Hickey, B.M., 1979. The California Current system – hypotheses and facts. Progress in Oceanography 8 (4), 191-279.

Hood, R.R., Abbott, M.R., Huyer, A., 1991. Phytoplankton and photosynthetic light response in the coastal transition zone off northern California in June 1987. Journal of Geophysical Research: Oceans 96 (C8), 14769-14780.

Hosegood, P., Gregg, M.C., Alford, M.H., 2006. Sub-mesoscale lateral density structure in the oceanic surface mixed layer. Geophysical research letters, 33 (22).

Hoskins, B.J., Bretherton, F.P., 1972. Atmospheric frontogenesis models: Mathematical formulation and solution. Journal of Atmospheric Science 29, 11-37.

Hoskins, B.J., 1975. The geostrophic momentum approximation and the semi-geostrophic equations. Journal of the Atmospheric Sciences 32 (2), 233-242.

Hoskins, B.J., Draghici, I., Davies, H.C., 1978. A new look at the ω-equation. Quarterly Journal of the Royal Meteorological Society 104, 31-38.

Hoskins, B.J., 1982. The mathematical theory of frontogenesis. Annual Review of Fluid Mechanics 14 (1), 131-151.

Huyer, A., 1983. Coastl upwelling in the California Current system. Progress in Oceanography 12 (3), 259-284.

Johnston, T.S., Cheriton, O.M., Pennington, J.T., Chavez, F.P., 2009. Thin phytoplankton layer formation at eddies, filaments, and fronts in a coastal upwelling zone. Deep Sea Research II 56 (3), 246-259.

Klein, P., Treguier, A.M., Hua, B.L., 1998. Three-dimensional stirring of thermohaline fronts. Journal of Marine Research 56 (3), 589-612.

Kruskopf, M., Flynn, K.J., 2006. Chlorophyll content and fluorescence responses cannot be used to gauge reliably phytoplankton biomass, nutrient status or growth rate. New Phytologist 169 (3), 525-536.

Landry, M.R., Ohman, M.D., Goericke, R., Stukel, M.R., Tsyrklevich, K., 2009. Lagrangian studies of phytoplankton growth and grazing relationships in a coastal upwelling ecosystem off southern California. Progress in Oceanography 83, 208-216.

Lévy, M., Klein, P., Tréguier, A.M., 2001. Impact of sub-mesoscale physics on production and subduction of phytoplankton in an oligotrophic regime. Journal of Marine Research 59, 535-565.

Li, Q.P., Franks, P.J.S., Ohman, M.D., Landry, M.R., 2012. Enhanced nitrate fluxes and biological processes at a frontal zone in the southern California current system. Journal of Plankton Research 34, 790-801.

MacVean, M.K., Woods, J.D., 1980. Redistribution of scalars during upper ocean frontogenesis – A numerical model. Quarterly Journal of the Royal Meteorological Society 106, 293-311.

Marchesiello, P., McWilliams, J.C., Shchepetkin, A., 2003. Equilibrium structure and dynamics of the California Current System. Journal of Physical Oceanography 33 (4),753-783.

McWilliams, J.C., Colas, F., Molemaker, M.J., 2009. Cold filamentary intensification and oceanic surface convergence lines. Geophysical Research Letters 36 (18).

Müller, P., Li, X.P., Niyogi, K. K., 2001. Non-photochemical quenching. A response to excess light energy. Planty Physiology 125 (4), 1558-1566.

Nagai, T., Tandon, A., Gruber, N., McWilliams, J.C., 2008. Biological and physical impacts of ageostrophic frontal circulations driven by confluent flow and vertical mixing. Dynamics of Atmospheres and Oceans 45 (3-4), 229-251.

Nagai, T., Gruber, N., Frenzel, H., Lachkar, Z., McWilliams, J.C., Plattner, G.K., 2015. Dominant role of eddies and filaments in the offshore transport of carbon and nutrients in the California Current System. Journal of Geophysical Research: Oceans. Online Access. doi: 10.1002/2015JC010889.

Oguz, T., Macias, D., Garcia-Lafuente, J., Pascual, A., Tintoré, J., 2014. Fueling Plankton production by a meandering frontal jet: A case study for the Alboran Sea (Western Mediterranean). PLoS ONE 9 (11): e111482.

Ohman, M.D., Powell, J.R., Picheral, M., Jensen, D.W., 2012. Mesozooplankton and particulate matter responses to a deep-water frontal system in the southern California Current System. Journal of Plankton Research 34 (9), 815-827.

Pallàs-Sanz, E., Johnston, T.M.S., Rudnick, D.L., 2010. Frontal dynamics in a California Current System shallow front: 1. Frontal processes and tracer structure. Journal of Geophysical Research: Oceans 115 (C12).

Pollard, R., 1986. Frontal surveys with a towed profiling conductivity/temperature/depth measurement package (SeaSoar). Nature 323, 433-435.

Roden, G. I., 1977. Oceanic subarctic fronts of the central Pacific: Structure of and response to atmospheric forcing. Journal of Physical Oceanography 7, 761-778.

Rudnick, D.L., 1996. Intensive surveys of the Azores Front: 2. Inferring the geostrophic and vertical velocity fields. Journal of Geophysical Research: Oceans 101 (C7) 16291-16303.

Spall, S.A., Richards, K.J., 2000. A numerical model of mesoscale frontal instabilities and plankton dynamics – I. Model formulation and initial experiments. Deep Sea Research Part I: Oceanographic Research Papers 47(7), 1261-1301, doi: 10.1016/S0967-0637(99)00081-3

Strass, V.H., 1992. Chlorophyll patchiness caused by mesoscale upwelling at fronts. Deep-Sea Research 39 (1), 77-96.

Thomas, L.N., Lee, C.M., 2005. Intensification of ocean fronts by down-front winds. Journal of Physical Oceanography 35 (6), 1086-1102.

Thomas, L.N., Tandon, A., Mahadevan, A., 2008. Submesoscale processes and dynamics. In Ocean Modeling in an Eddying Regime. Geophysical Monograph Series 177, 17-38.

Washburn, L., Kadko, D.C., Johnes, B.H., Hayward, T.P., Kosro, M., Stanton, T.P., Ramp, S., Cowles, T., 1991. Water mass subduction and the transport of phytoplankton in a coastal upwelling system. Journal of Geophysical Research: Oceans 96 (C8), 14927-14945.

Yuan, X., Talley, L.D., 1992. Shallow salinity minimum in the North Pacific. Journal of Physical Oceanography 22, 1302-1316.

Zakardjian, B., Prieur, L, 1998. Biological and chemical signs of upward motions in permanent geostrophic fronts of the Western Meidterranean. Journal of Geophysical Research: Oceans 103 (C12) 27849-27866.

Chapter 4.

Submesoscale Mixed Layer and Symmetric Instabilities: Physical Dynamics and Biological Responses.

Abstract

There has been a recent surge of interest in the role of submesoscale frontal instabilities in altering phytoplankton production. Understanding the potential biological effects of these instabilities requires a good understanding of the physical dynamics of fronts; this can be challenging for non-specialists. To help build intuition about submesoscale physical-biological coupling at fronts, we review two submesoscale dynamics: symmetric instabilities and mixed layer instabilities. Our goal is to describe these physical phenomena in terms that will build the intuition of non-specialists who may be observing them (either purposely or serendipitously) in models and in the field. We first discuss the conditions favorable for their development, then describe the motions they induce, and finally explore the effects they may have upon phytoplankton growth and distribution patterns at fronts.

4.1. Introduction

Water motions in the ocean occur over a large range of spatiotemporal scales, and different motions have different impacts on phytoplankton life cycles, distributions, and ecological contributions to primary productivity. From global thermohaline circulation to molecular diffusion and turbulence, the physical environment mediates all the

ecologically important aspects of a phytoplankter: nutrient and light availability, and encounter rates with congeners and other organisms involved in trophic transfers and other ecological functions, be it bacteria, viruses, or predators. Ecological responses scale with the spatiotemporal nature of physical forcing; these responses range from biogeographic distributions determined by global interannual/climatic cycles, to patchy blooms and layers created by local circulation patterns. Thus, understanding biological dynamics in the ocean requires understanding of the physical forcing, in addition to all the ecological complexities of biological origin.

One particularly important spatiotemporal scale is the submesoscale, ranging over 1-10's of kilometers and encompassing dynamics that occur over 1 day to weeks. Submesoscale dynamics are particularly important at fronts – regions of enhanced horizontal density gradients. Fronts have been known as areas of enhanced biological activity for decades; from regions of enhanced phytoplankton primary productivity to hotspots for mobile top predators [*Franks,* 1992*; Owen,* 1981*; Olson et al.,* 1994*; Sournia,* 1994]. Fronts biologically are important because of their enhanced vertical circulation and sensitivity to instabilities that can mix the water column vertically and horizontally [*Mahadevan and Tandon*, 2006]. Two such instabilities in particular, Symmetric Instability (SI) and Mixed Layer Instability (MLI), have received attention recently for their role in biological dynamics such as the North Atlantic Spring Bloom [*Taylor and Ferrari*, 2011b].

Our primary aim is to provide a description of these two submesoscale instabilities, SI and MLI, their associated motions, and their potential biological consequences. We hope to provide the reader with increased intuition concerning the

range of submesoscale phenomena, why they occur, where and when to expect them within the ocean, and their possible ramifications for planktonic ecosystems. Section 2 provides an overview of the submesoscale regime, a discussion of relevant concepts and metrics of the physical dynamics at a front, and introduces our methodology of evaluating biological impacts. Sections 3 and 4 look at SI and MLI, respectively, reviewing the required conditions and nature of each instability's development, and particular ecological impacts. Section 5 provides conclusions regarding biological responses to submesoscale instabilities at fronts.

4.2. Submesoscale phenomena, terminology, and set-up

Before delving into the two submesoscale instabilities, we provide a background characterizing the submesoscale, followed by an explanation of the terms that will be used in this paper, and finally a description of our general approach in assessing biological impacts. First, we review submesoscale variability and its biological implications. Then, we will consider the relative scales of variability in density, both horizontal and vertical, what this means for ocean dynamics, and how the physical oceanography discipline communicates these properties. We also discuss useful metrics for characterizing a flow. Finally, we will provide two general hydrographic scenarios that will be used throughout our discussion to motivate investigations of the two dominant factors limiting phytoplankton growth: light and nutrients.

4.2.1 Characteristics of the submesoscale and biological relevance

Both SI and MLI occur in the spatiotemporal regime known as the submesoscale. This range, with spatial scales O(1-10 km), with timescales O(1 day-weeks), shows a strong dynamic signature at surface ocean fronts and small eddies. Fronts are regions of enhanced horizontal density gradients. While basin-scale circulations provide a mean flow, the local surface currents are typically dominated by fluctuations caused by eddies and fronts. Indeed, a large portion of the surface kinetic energy of the ocean, which scales with the magnitude of velocity squared, is present in eddies and fronts [*Wyrtki et al.*, 1976; *Stammer*, 1997]. The submesoscale contrasts with the more familiar mesoscale, populated by larger eddies like the rings of the Gulf Stream [e.g., *Olson*, 1991]. Mesoscale features characteristically occupy spatial scales of O(10-100 km) and evolve over O(weeks-months).

Both physical and biological oceanographers have begun to intensively study the transition from the smaller submesoscale regime, dominated by fronts, to the larger mesoscale regime populated by eddies. A present challenge in biological oceanography is to determine the net impact of fronts and submesoscale motions on global primary production [*Thomas et al.*, 2008]. For decades fronts have been known to be biological hotspots; whales, fish, seabirds, and other top predators routinely aggregate at fronts to exploit the locally enhanced production, where fishermen in turn exploit the fish [*Yoder*, 1990; *Olson*, 2002]. Additionally, satellite observations of phytoplankton pigments show large gradients visible within coherent physical structures – swirls, filaments, and vortices – which occur precisely at the submesoscale [*Munk et al.*, 2000]. Given these

biological signals, it is imperative to understand the relevant mechanisms of motion that explain the ecological impacts of fronts.

One approach to exploring the impact of mesoscale vs. submesoscale motions is to compare their horizontal and vertical motions. Mesoscale horizontal stirring, for example, has been shown to produce ecological niches, maintaining phytoplankton diversity [*d'Ovidio et al.*, 2010; *Perruche et al.*, 2011]. Ostensibly, horizontal gradients at the submesoscale would offer similar barriers to exchange, contributing to the observed mesoscale patterns, though at smaller horizontal scales. Where mesoscale and submesoscale phenomena diverge, however, is in their vertical circulations.

Unlike mesoscale flows, a characteristic of submesoscale physics is enhanced vertical motions, including the potential of upwelling nutrients to stimulate new production, or downwelling existing biomass away from the euphotic zone [*Mahadevan and Tandon*, 2006; *Thomas et al.*, 2008]. Even if there is a large-scale balance of upwelling and downwelling, the sheer magnitude of the locally enhanced vertical fluxes at fronts will have consequences for the phytoplankton community. Niches created by locally enhanced upwelling support larger size classes of phytoplankton with higher growth rates and better inorganic nutrient utilization, altering the trophic transfer efficiency [*Moloney and Field*, 1991]. Unexpected consequences may also result, such as the redistribution of large-scale nutrient pools to reduce overall primary production [*Lévy et al.*, 2012]. Though the role of submesoscale fronts and their motions in altering production is starting to be explored, there is a great deal of work to be done, both from observational and theoretical modeling perspectives; the impact of these motions in an ocean experiencing global climate change is largely unknown.

The practical relevance of understanding submesoscale variability goes beyond fronts and global production. Due to the scale of ships as observational platforms – typically traversing kilometers over the course of a day, and cruises lasting from days to months – submesoscale variability will inevitably affect all biological measurements. Observations of large-scale, regional processes must account for submesoscale fluctuations that vary between stations a few kilometers apart, or over weekly timescales. Similarly, investigations of small-scale biological interactions within a given water parcel, especially using popular quasi-Lagrangian methods [*Landry et al.*, 2009], might produce drastically different results if applied a few kilometers away or days later, due to the intense heterogeneity induced by submesoscale motions.

Finally, due to the short timescales involved with the evolution of submesoscale phenomena, it is difficult to plan an oceanographic research cruise to sample them. Therefore, the more the broader oceanographic community understands their characteristics, the greater the chance to implement a rapid response to observe them while at sea.

4.2.2 Buoyancy, Vertical Stratification, and Horizontal Density Gradients

4.2.2.1 Definition of Buoyancy

By definition, buoyancy is the rescaled density,

$$b = -g\frac{\rho}{\rho_0} \tag{1}$$

where g is the gravitational acceleration, ρ is density, and ρ_0 is a background mean density value. In making buoyancy negative, the intuitive meaning of buoyancy is

attained: i.e., when a water parcel becomes denser, it loses buoyancy (*b* becomes more negative) and sinks. Therefore, the term *buoyancy flux* generally refers to changes in the density in a given region, and isopycnals will coincide with isopleths of buoyancy. Sign conventions across boundaries can sometimes confuse what constitutes a positive versus a negative buoyancy flux. For our purposes, if a buoyancy flux increases the local buoyancy (*b* becomes less negative) inside a water parcel, this will be considered a positive buoyancy flux. If solar heating lowers the density, it increases buoyancy, so the input of solar energy translates into a positive buoyancy flux (n.b. this is opposite of the usual convention for boundary fluxes). Cooling does the opposite, and a significant negative buoyancy flux at the surface can lead to convective overturning of the water column (sinking of cold, dense surface water), such as during North Atlantic Deep Water formation.

Buoyancy fluxes can also result from advective changes, such as a warm-core eddy wandering into a region of cold water. Since the eddy is anomalously warm and increases buoyancy, we consider this to be a positive buoyancy flux. The previous statement regarding eddy buoyancy flux and solar heating thus refers to the contribution of an eddy to altering density through horizontal advection of warm water, compared to the effects of local *in situ* solar heating.

4.2.2.2 Energy considerations

When buoyancy is altered or vertically redistributed, these changes imply transfers of energy. In solar heating, for example, the Sun's radiant energy is transferred to the water in the form of increased temperature. The temperature change represents a

thermodynamic "inherent" energy present in water as heat. Therefore, in the previous section comparing an advecting warm-core eddy to *in situ* solar heating, this is a direct comparison of heat energy.

The vertical redistribution of buoyancy transfers another form of energy, namely gravitational potential energy. The Earth's gravitational pull creates potential energy due to height displacements relative to its surface. The magnitude of potential energy is proportional to the products of mass, gravitational acceleration, and height displacement. Consider a tank of water with a vertical barrier separating it into two halves; the right half is filled with cold water (less buoyant, more dense) and the left filled with hot (more buoyant, less dense) water (Figure 4.1a). Both volumes of water have the same mass, but the more buoyant (less dense) water displaces more volume, so its surface is elevated relative to the less buoyant water by a distance h_{disp}.

The force of gravity upon the tank's water can be represented as acting on the center of mass of each water volume. The tank's total center of mass is centered horizontally in the tank, and near the vertical center, displaced somewhat upwards due to the warmer water's higher elevation. This displacement is proportional to the difference in density between the hot and cold water.

Each side of the tank is unstratified vertically. Intuitively, if we remove the barrier, the elevated surface of the hot water will flow over to the cold side, and the cold water will move across the bottom toward the warm side. Eventually the tank will stratify, with the two layers stacked upon each other, hot over cold [Figure 4.1b, *Franks and Franks*, 2009]. The tank's center of mass is still centered horizontally, but is lower vertically than before. The height change means that in *restratifying*, potential energy was

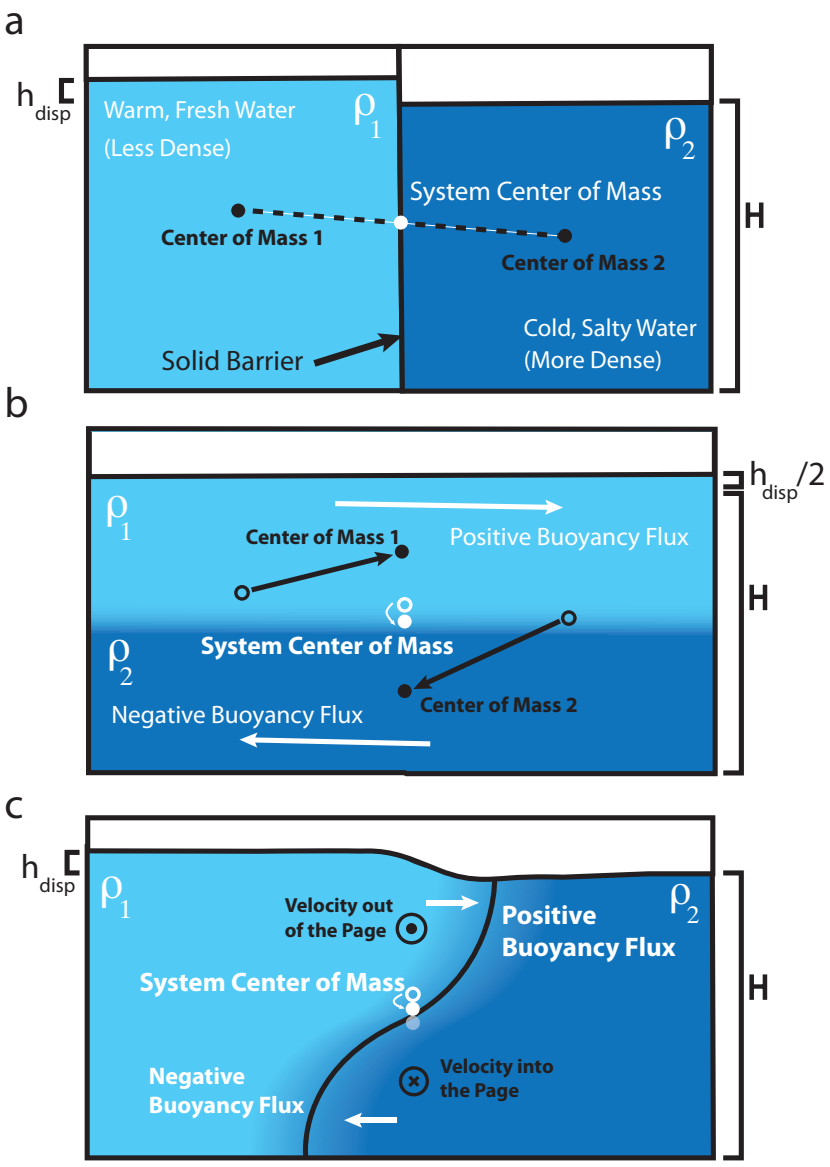

Figure 4.1. Geostrophic adjustment. (a) Two water masses are initially separated by a barrier. (b) Upon removal of the barrier, without rotation the light water will move over the heavy water (positive buoyancy flux at the surface, negative at depth) and move the system's center of mass downward, releasing potential energy. (c) With rotation, the restratification stops partway, establishes a geostrophic current, and releases only a portion of the potential energy present in the initial horizontal density gradient.

released. This potential energy release is transferred into the kinetic energy of the water, which will typically create waves, and be ultimately released by some mixing and friction along the tank's walls.

In this study, we will be focusing on the possible ways that submesoscale instabilities and motions at fronts can lead to a rearrangement or movement of isopycnals, which is essentially a buoyancy flux. When isopycnals are rearranged to be flatter, or more stratified relative to the initial state like in our tank scenario (i.e., *restratification*), this will be considered to be a positive buoyancy flux near the surface and a negative flux near the bottom (Figure 4.1b). Ignoring mixing, heating/cooling, or precipitation/evaporation, the net buoyancy for the whole region should not change. By rearranging the center of mass, the local buoyancy fluxes thus are equivalent to a release of potential energy. This is why buoyancy is a useful variable: fluxes of buoyancy are a universal way to consider different forms and sources of energy in a dynamic system.

4.2.2.3 Stratification and Horizontal Density Gradients

Using buoyancy, the definition for stratification, or the scaled vertical density gradient, becomes the vertical gradient of buoyancy,

$$N^2 = -\frac{g}{\rho_0}\frac{\partial \rho}{\partial z} = \frac{\partial b}{\partial z} \qquad (2)$$

The stratification, N^2 (also called the buoyancy frequency or Brunt-Väisälä frequency, squared) is useful for understanding physical dynamics: it will be negative when heavy water lies on top of light water, which is gravitationally unstable. Because the stratification is a measure of how quickly density changes with depth, one interpretation

of a higher N^2 is that water moved vertically will be more quickly restored to its equilibrium depth: when vertical density differences are greater, gravity will act more strongly. Therefore, it makes sense that the local buoyancy frequency, N, provides an upper bound for the possible frequencies of internal waves, providing the well-known relation

$$f < \omega < N \tag{3}$$

where ω is the frequency of an internal wave, and f is the local Coriolis frequency determined by the Earth's rotation.

Buoyancy can also be used when describing horizontal density gradients. We will represent a horizontal buoyancy gradient as

$$\nabla_h b = \left(\frac{\partial b}{\partial x}, \frac{\partial b}{\partial y} \right) \tag{4}$$

where ∇_h is the horizontal gradient operator, which gives buoyancy gradients as an (x,y) vector oriented in the across-front direction (i.e., perpendicular to the strongest horizontal density gradient).

In general, near the ocean surface the gradients of buoyancy are much greater in the vertical direction than the horizontal. Biogeochemical tracers, such as nutrients, likewise have strong vertical gradients that are often aligned with isopleths of buoyancy (isopycnals) [*Omand and Mahadevan*, 2013; 2015]. Because of the dominance of vertical gradients, we will be focusing on the vertical movements of water parcels and changing nutrient/light limitation in evaluating the biological effects of submesoscale motions.

4.2.3 Geostrophic balance and Richardson Number

4.2.3.1 Geostrophic balance

Most of the surface currents in the ocean are in a near-geostrophic balance, defined as an equilibrium between the horizontal pressure gradient and Coriolis forces [*Niiler et al.*, 2003]. In a rotating reference frame such as the Earth, the non-inertial Coriolis force is strong enough to deflect horizontal flows at large scales. Returning to our tank scenario, in a rotating reference frame such as the Earth, upon removal of the barrier the water will begin to restratify as before. However, with rotation the restratification does not proceed to completion. At the spatial scales of fronts in the ocean (kilometers), the Coriolis force offsets the gravitationally induced horizontal pressure gradient, leading to a geostrophic balance. This equilibrium leads to the familiar geostrophic currents observed in the ocean, where a horizontal buoyancy gradient is associated with horizontal velocities directed perpendicular to the gradient (i.e., along isopycnals, Figure 4.1c). The generation of these velocities from our initial condition (Figure 4.1a) is termed *geostrophic adjustment*. The particular example of geostrophic adjustment used in figure 4.1c is adapted from *Stommel and Veronis* [1980], where we refer the interested reader for a full mathematical treatment. Of particular note is that during adjustment, some of the gravitational potential energy present in the initial condition is converted into waves that radiate away, and some into the kinetic energy of the geostrophic current. However, in a geostrophically balanced front there is still considerable potential energy present within the horizontal buoyancy distribution that is not released [*Gill et al.*, 1974]. Therefore, one way to look at geostrophic balance is the premature arrest of potential energy release – the isopycnals do not become flat, as we

would expect in the non-rotating case. Restratification has been interrupted. For the remainder of this study, we will begin with an initial scenario in which the currents are largely in geostrophic balance.

4.2.3.2 Richardson number

For this paper, we wish to characterize the conditions under which submesoscale instabilities can occur. The following discussion follows from *Thomas et al.* [2013]. One useful characterization of a flow is the balanced Richardson number: the ratio of the vertical density stratification to the vertical velocity shear, or

$$Ri = \frac{N^2}{\left(\frac{\partial u}{\partial z}\right)^2} \tag{5}$$

Since we will be considering currents in which geostrophic velocities are initially dominant, we can convert the vertical velocity shear into a horizontal density gradient using the thermal wind relation,

$$\left|\frac{\partial u}{\partial z}\right| = \frac{g}{f\rho_0}\nabla_h \rho = \frac{\left|\nabla_h b\right|}{f} \tag{6}$$

so that now the Richardson number can be expressed as a ratio between the horizontal and vertical buoyancy gradients,

$$Ri = \frac{f^2 N^2}{\left|\nabla_h b\right|^2} \tag{7}$$

In this formulation, the Richardson number varies from $-\infty$ to $+\infty$, and can be difficult to interpret. We can convert the Richardson number into an angle ϕ such that

$$\phi = \tan^{-1}\left(-\frac{|\nabla_h b|^2}{f^2 N^2}\right) \tag{8}$$

These conversions may seem initially trivial; however, ϕ can be used to diagnose conditions in which certain instabilities may occur, as indicated in figure 4.2 (also adapted from *Thomas et al.*, [2013]). The usefulness of this relation should not be underestimated. Starting with only measurements of vertical and horizontal gradients of density, such as can be acquired during a CTD transect, it is possible to determine the types of instability likely to occur in a given region. Given the very different characteristics of the vertical motions driven by different instabilities, knowledge of the potential instabilities will significantly improve our understanding of the potential biological responses.

We will consider two aspects of figure 4.2 – cyclonic or anticyclonic vorticity, and interpretation of the axes – in the following sections. For now, one intuitive interpretation of this figure is that the ratio of horizontal to vertical buoyancy gradients provides the conditions for a given instability. While stronger horizontal buoyancy gradients represent increased potential energy (and the kinetic energy present in the geostrophic current), vertical buoyancy gradients somewhat represent how easy it is to release this energy via instability (stronger stratification makes it harder for instabilities to develop). Once a relative threshold in the ratio is reached (i.e., an increasingly negative ϕ), submesoscale instabilities may occur.

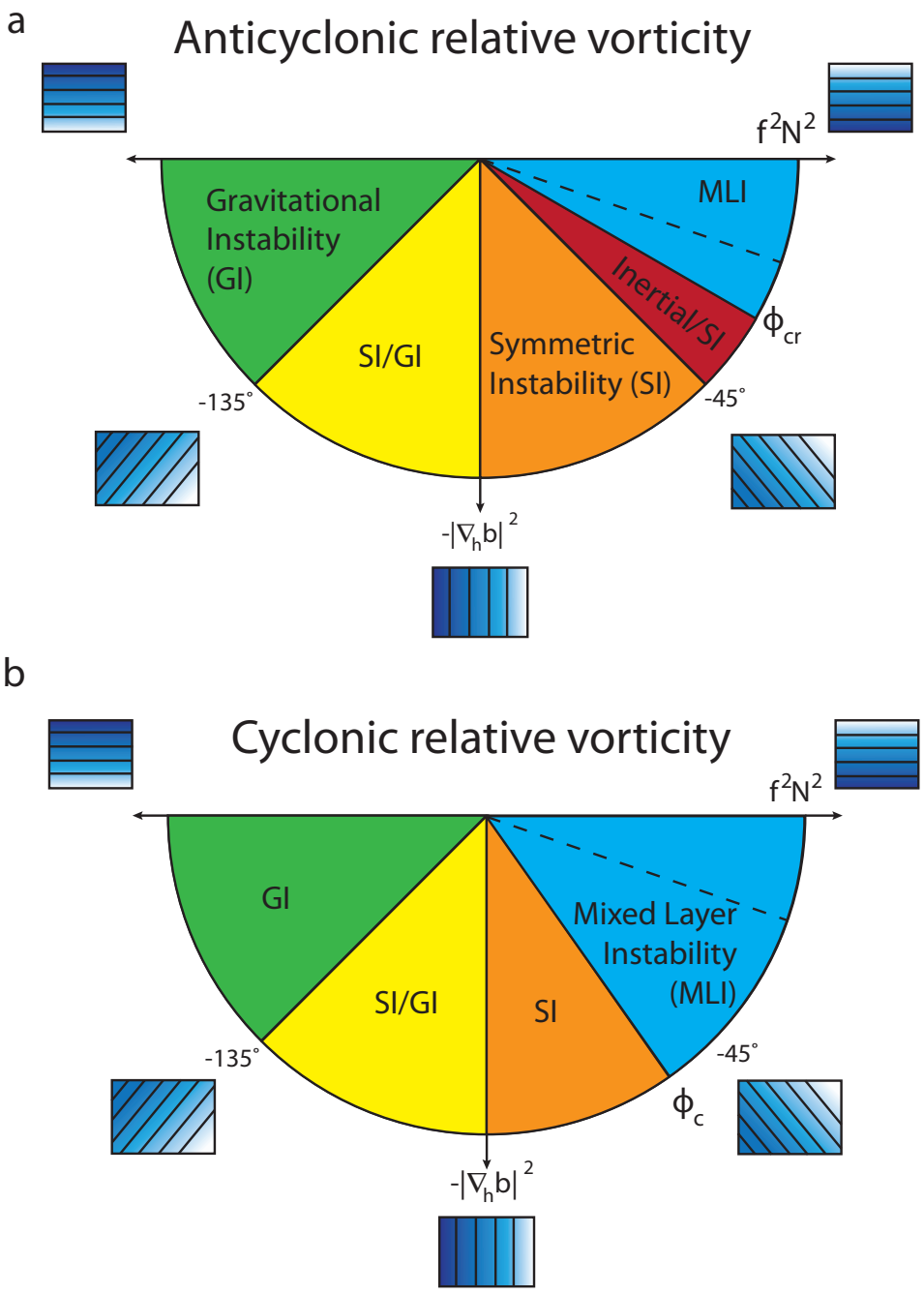

Figure 4.2. Criteria for gravitational (GI), symmetric (SI), inertial, and mixed layer instabilities (MLI) using the metric ϕ. Necessary conditions are presented for (a) anticyclonic vorticity and (b) cyclonic vorticity. Rectangular panels indicate relative distribution of heavy (blue) and light (white) water for different ϕ. In the case of zero relative vorticity, there is no red region of mixed inertial/symmetric instability, and ϕ_{cr} is -45°. The dashed black line denotes MLI with growth rate 0.7 day^{-1}.

4.2.4 Biological Scenarios

As mentioned previously in the definition of stratification, if N^2 is negative, the water column is gravitationally unstable and will overturn. Logically, if N^2 is positive, the water column is stable (less-dense water overlies denser water). But as N^2 approaches zero, the water column can in a sense be considered less stable, as indicated when ϕ approaches -90° (or moving along the top of the semicircle from positive to negative along the N^2 axis in figure 4.2). In our consideration of submesoscale fronts, we will explore two general biological scenarios with different N^2 distributions.

Our first scenario has a linear local horizontal buoyancy gradient in the upper layer, with weak N^2 of 10^{-6} s^{-2} that continues to the base of the mixed layer (Figure 4.3a). This buoyancy distribution is chosen to reflect wintertime conditions in temperate regions, when the phytoplankton community tends to be light limited due to ongoing vertical displacements of phytoplankton within the water column driven by forcing at the surface (white arrows in Figure 4.3a). The necessity for active forcing in light limitation is important to note (viz. the "mixed" vs. "turbulent" layer in *Franks*, [2014]). When we later consider the role of instability-driven restratification in alleviating light limitation, the phytoplankton response will depend on the competitive balance between surface forcing creating turbulent motions and front-driven restratification. If the instability is able to sufficiently restratify the water column, then turbulent motions are reduced (fewer white overturning arrows), in turn increasing the average exposure of phytoplankton to light, and so an increase of production is to be expected. This is precisely the mechanism in *Taylor and Ferrari* [2011a], termed "convective turbulence shutdown," which is an extension of the Critical Turbulence Hypothesis introduced by *Huisman et al.* [1999].

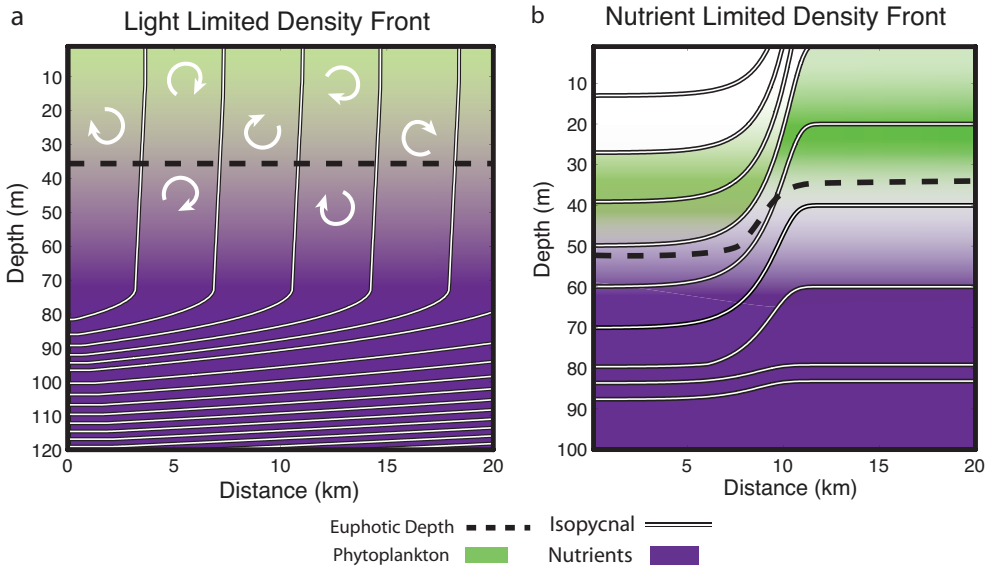

Figure 4.3. Initial conditions for (a) light-limited and (b) nutrient-limited phytoplankton assemblages. The light-limited front has phytoplankton (green) and high concentrations of nutrients (purple) throughout the mixed layer, with active mixing (white arrows) responsible for the light limitation, which extend below the euphotic zone (black dashed line). Isopycnals are plotted at 0.1 kg/m^3 intervals in the mixed layer, and 0.2 kg/m^3 below. The nutrient-limited front has an oligotrophic (left, light green) and eutrophic (right, dark green) side, both with subsurface maxima in biomass. Nutrients increase with depth below the euphotic depth. Contours of density (white and black lines) are shown at 0.2 kg/m^3 intervals.

Negative surface heat flux (cooling) produces a convective layer that will generally not restratify. We will graphically represent this layer's bottom extent by a dashed white line in later figures. A parameterization for the actual depth of this layer can be found in *Taylor and Ferrari* [2010].

The second scenario is an isolated front as one might expect to see in the ocean, with a mixed layer bounded underneath by a pycnocline, and with a horizontal buoyancy gradient in geostrophic balance (Figure 4.3b). The biological community here is nutrient limited, and represented by an oligotrophic community on the more buoyant (less dense) side, and a eutrophic community on the less buoyant (more dense) side, both with

subsurface maxima in phytoplankton biomass concentration. A large-scale vertical nutrient gradient is present, with a maximum located at the bottom of the euphotic zone, just below the mixed layer. The N^2 in the mixed layer is ~10^{-4} s^{-2}.

For scaling purposes, we will consider the phytoplankton in both these scenarios (light limited and nutrient limited) to have maximum growth rates of ~0.7 day^{-1}, which corresponds to a daily population doubling. Therefore, if the motions under consideration relieve the light or nutrient limitation within a phytoplankton doubling time, an increase of primary production is to be expected. We assume possible effects upon higher trophic levels (e.g., zooplankton biomass response) will occur on longer timescales and will not be considered explicitly in this study.

Now that the relevant principles, terms, and biological scenarios have been delineated, we will begin our exploration of submesoscale instabilities.

4.3. Symmetric Instability

The first submesoscale instability that we will consider is Symmetric Instability (SI). Known in the atmospheric literature for decades, this instability has gained recent attention in oceanography due to evidence of its presence in the Gulf Stream and Kuroshio currents [*D'Asaro et al.*, 2011; *Thomas et al.*, 2013]. Of the instabilities and motions we will consider, the generation, evolution, and dissipation of SI are the most spatially restricted to the submesoscale.

What to exactly call SI has been historically ambiguous. *Emanuel* [1988] called SI "slantwise convection". *Haine and Marshall* [1998] consider SI to be a hybrid instability containing parts of both centrifugal and gravitational instabilities. In fact, the

tendency to misuse SI's role in cloud banding in the atmospheric literature has led to papers that point out common misconceptions and misapplications (e.g., *Schultz and Schumacher*, [1999]). The term "symmetric" stems from the fact that the perturbation waveforms responsible for the instability do not change along-front **[***Stone*, 1966]. We will begin with the conditions diagnostic of SI, and define the relevant frontal motions, before interpreting the possible biological effects.

4.3.1 Conditions needed for SI

One diagnostic condition for SI to occur is that Ertel Potential Vorticity (EPV) is negative [*Hoskins,* 1974]. Before one balks at this statement, the important thing to realize is that our previously defined metric, ϕ, contains this information within it. Thus density observations provide a means to determine whether SI can be reasonably expected.

However, before moving forward, an elucidation of EPV and the various terms contributing to its overall positive/negative nature is required. EPV can be defined as

$$q = \left(f\hat{k} + \nabla \times \vec{u}\right) \cdot \nabla b \qquad (11)$$

with $\hat{k}$ being the vertical unit vector, $\nabla \times \vec{u}$ the three-dimensional curl of velocity, and ∇b the three-dimensional buoyancy gradient. Assuming our currents are in geostrophic balance, similarly to Section 2.3.2 we can rewrite (11) as

$$q = N^2\left(f + \zeta_{rel}\right) - \frac{1}{f}\left|\nabla_h b\right|^2 \qquad (12)$$

where ζ_{rel} is the relative vorticity due to the geostrophic horizontal currents, $\left(\frac{\partial v_g}{\partial x} - \frac{\partial u_g}{\partial y}\right)$.

Notice that the last term on the right states that no matter what the direction, a stronger horizontal buoyancy (i.e. density) gradient always contributes negatively to EPV (Figure 4.4c). Since $N^2 f$ is always positive for stably stratified water columns (Figure 4.4b), there are only two ways to make q negative: 1) the relative vorticity ζ_{rel} becomes sufficiently negative (anticyclonic) or 2) the horizontal buoyancy gradient strengthens.

As elucidated in *Thomas et al.* [2013], SI becomes the dominant mechanism governing perturbation flows when ϕ is below a critical value,

$$\phi < \phi_{cr} = \tan^{-1}\left(-\frac{\zeta_g}{f}\right) \qquad (13)$$

where ζ_g is $f + \zeta_{rel}$, the vertical component of vorticity from the geostrophic flow (the term in parentheses in (12)). While this condition appears daunting, we can characterize this critical value based upon our two general frontal scenarios.

For the wintertime, light-limited scenario, with weak N^2 stratification and linear horizontal buoyancy gradient (isopycnals equally spaced in a horizontal sense, Figure 4.3a), ζ_{rel} (second part in parentheses in (12)) is zero, so ζ_g is equal to f, giving a critical value of ϕ of -45°. Though linear horizontal buoyancy gradients are not generally expected in the ocean, they provide a useful base condition wherein SI should be considered, namely $\phi <$ ~ -45°. The horizontal change of density required for our wintertime mixed layer with N^2 of 10^{-6} s^{-2} is ~ 0.01 kg m^{-3} per km, roughly equivalent to a ~0.5 °C temperature change over 10 km.

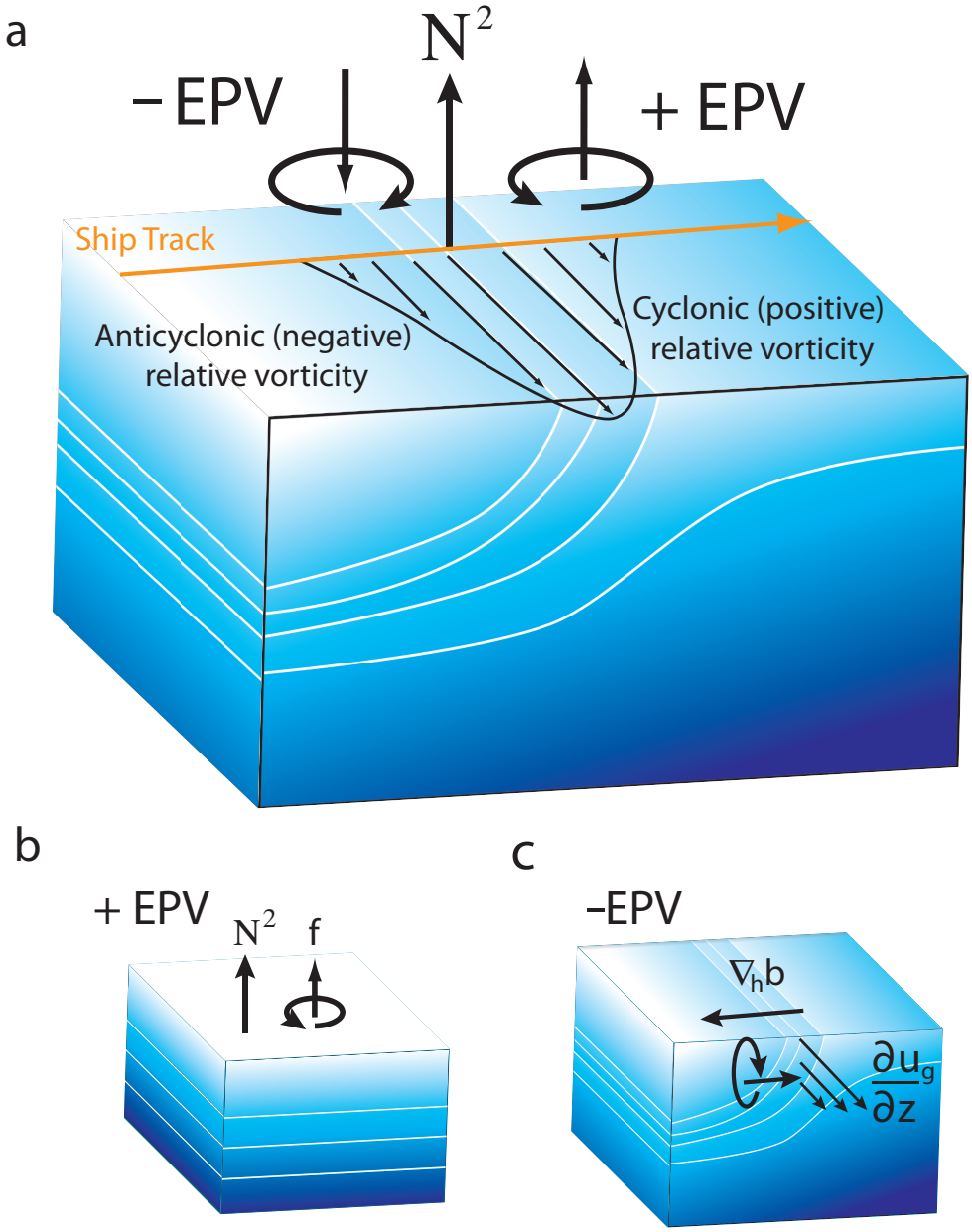

Figure 4.4. Schematic of an isolated front. (a) A ship is sampling across a front, isopycnals shown in white, going from left to right, indicated by the orange line. The geostrophic current increases with increasing density gradient, then decreases again. A region of anticyclonic relative vorticity with negative EPV contribution is encountered prior to a cyclonic region with positive EPV. (b) The planetary vorticity, *f*, always contributes to positive EPV. (c) By contrast, horizontal density gradients in geostrophic balance always contribute to negative EPV.

The nutrient-limited scenario, with an isolated front, is somewhat more complicated. Since the magnitude of the horizontal buoyancy gradient increases then

decreases as one moves across the front (from the left to the right in Figure 4.4a), there is a region of anticyclonic (ζ_{rel} negative) vorticity followed by cyclonic (ζ_{rel} positive) vorticity. The change in magnitude of the along-front geostrophic current, as well as the change in relative vorticity, are both shown schematically in figure 4.4. Looking at (12), we can see that if ζ_{rel} is negative, the EPV q is reduced, as well as $\zeta_g = f + \zeta_{rel}$, changing the instability condition for SI. Now ϕ_{cr} is >-45° (shown in Figure 4.2a). The opposite is true for the cyclonic region (ζ_{rel} positive), where the front is more stable to SI. Therefore, in an isolated front, SI would be expected to occur predominantly on the less dense side of the front with anticyclonic vorticity, and would be less likely on the denser cyclonic side. Since the nutrient-limited N^2 is 10^{-4} s^{-2}, rather than 10^{-6} s^{-2} in the light-limited scenario, the instability criterion for SI translates into an order of magnitude increase in density gradient, leading to an approximate change of 0.1 kg m^{-3} per km, or ~5° C over 10 km – quite a strong change for much of the ocean.

The strong horizontal buoyancy gradients needed for SI preclude its presence in the majority of the world's oceans. *Thomas et al.* [2013] predict that SI will be important in the energetic regions of western boundary currents and frontal regions of the Southern Ocean. By contrast, SI is less likely to occur in more quiescent regions such as central subtropical gyres. The possibility of SI in intermediately energetic regions, such as eastern boundary currents with coastal upwelling, fronts with down-front winds, and regions of considerable mesoscale activity, has not been considered in depth and remains an open question (though negative EPV has been circumstantially detected in the model of *Capet et al.* [2008]).

Importantly, as shown in figure 4.2, a different instability can co-occur with SI when there is anticyclonic vorticity. This instability, termed "inertial" or "centrifugal" instability, occurs when the ζ_{rel} is negative enough to cancel out f in ζ_g (beware that in the literature, SI is sometimes considered as a kind of "centrifugal" instability, as well). In this case, ϕ_{cr} becomes 0. Inertial instability requires a strong anticyclonic flow ($\zeta_g < 0$), and is usually studied in the context of eddies or cyclones [*Wang and Özgökmen*, 2015; *Kloosterziel et al.*, 2007]. Additionally, recent studies focusing on this instability [*Jaio and Dewar*, 2015; *Molemaker et al.,* 2015] highlight its geographically particular and subsurface generation conditions, away from the euphotic zone. As it happens, inertial instability leads to overturns similar to SI in nature and with comparable timescales [*Kloosterziel et al.*, 2007], so its phenomenology and displacement from the euphotic zone justify our choice in not explicitly considering inertial instability further in this study.

Having elucidated the theoretical conditions for SI, here we discuss how to evaluate its presence from field data. One pragmatic way to calculate the value of ζ_g from shipboard measurements is to measure the difference in acoustic Doppler current profiler (ADCP) horizontal velocities as one traverses a front. Moving from the light water to the heavy water in figure 4.4a, we change from anticyclonic vorticity to cyclonic vorticity. As one encounters the geostrophic jet, which is moving 90 degrees to the right (left) of the shiptrack in the northern (southern) hemisphere (Figure 4.4a), the change in the magnitude of horizontal velocity divided by distance gives a measure of the geostrophic vorticity, to be used in condition (13). A positive change means negative (anticyclonic) vorticity, and a negative change indicates positive (cyclonic) vorticity. Considering the

strong horizontal frontal buoyancy gradient needed for SI, it is reasonable to assume that the majority of the observed along-front ADCP signal would be due to geostrophic currents, and can be used to provide a more accurate criterion for SI beyond $\phi = -45°$.

4.3.2 What happens during SI

The motions during SI are oriented across-front and are nearly aligned with isopycnals (Figures 4.5a, 4.6a) [*Haine and Marshall*, 1998]. Therefore, from this starting point there appears to be little possibility of buoyancy flux. However, as SI begins to displace water and grow, secondary instabilities such as Kelvin-Helmholtz instability begin to form due to the across-isopycnal velocity shear, resulting in turbulent flow (Figures 4.5b, 4.6b). This turbulent flow begins to mix water with opposing vorticity (ultimately sourced from the surface and the thermocline; *Haine and Marshall*, [1998]; *Taylor and Ferrari*, [2009]), bringing the Ertel potential vorticity back to zero, and dissipating the conditions that led to SI in the first place. It is in this sense that SI is limited spatially, since its instability leads to its own exhaustion. SI's spatial scale is thus relegated to the area of strong horizontal buoyancy gradients that satisfy the instability criterion (13), i.e., on the order of kilometers. It should be noted, however, that the energy source for SI is not the release of potential energy through relaxed isopycnals, but rather extraction of kinetic energy from the associated geostrophic current (the geostrophic shear production term, or GSP, in *Thomas et al.*, [2013]). However, the net effect of these motions and their mixing upon the density distribution is to restratify the water column, equivalent to a positive buoyancy flux near the surface and a negative flux deeper down.

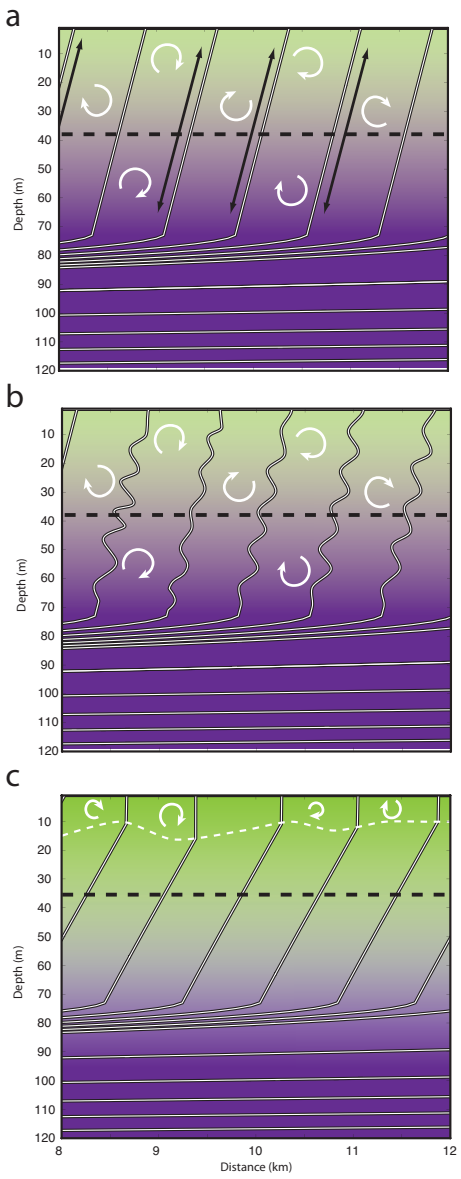

Figure 4.5. SI at a light-limited front. (a) Perturbations move water along isopycnals (black arrows). (b) As perturbations grow, they distort isopycnals and induce secondary instabilities. (c) After equilibration, isopycnals have restratified below the convective layer (white dashed line). Overturns are now restricted to near the surface, alleviating light limitation, inducing increased phytoplankton primary production (darker green near the surface). Mixed layer isopycnals are contoured at 0.01 kg/m^3 intervals.

This restratification occurs quickly, typically over the course of hours to a day [*Stone*, 1966].

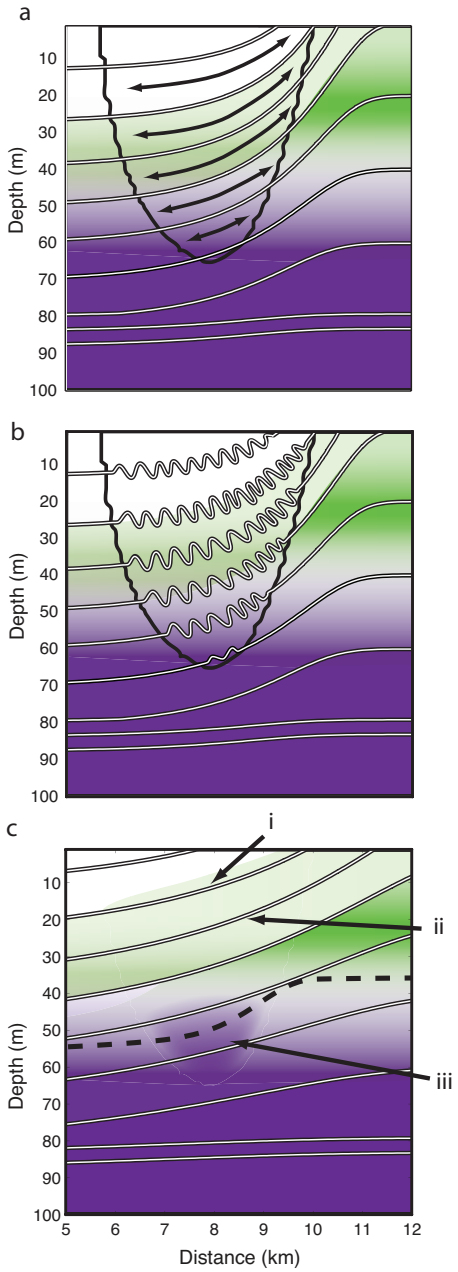

Figure 4.6. SI at a nutrient-limited front. (a) Perturbations aligned with isopycnals, and restricted to instability region (black outline). (b) Onset of stratified turbulence. (c) Front after SI: phytoplankton vertical gradients are somewhat smoothed (i), the isopycnals are slightly flattened (ii), and possible nutrients are entrained from below the instability region (iii).

4.3.3 Biological effects during light limitation

As mentioned in the previous section, SI's net effect is to quickly restratify the local water column at a front. Therefore, the local N^2 is increased, and vertical movements of water are reduced relative to the initial condition (white arrows below convective layer in Figure 4.5c). By reducing the vertical displacement of phytoplankton, for example, SI can alleviate light limitation caused by deep mixing in turbulent layers of a front during wintertime conditions, essentially the "convective turbulence shutdown". *Taylor and Ferrari* [2011b] studied this result in the context of the North Atlantic spring bloom. The hourly-daily timescale of SI overlaps well with the doubling time of phytoplankton, allowing for the observed increase in modeled phytoplankton concentration. The results of *Taylor and Ferrari* [2011b] show that SI led to weaker restratification than mixed layer instability (MLI), which we will consider in Section 4. Interestingly, the phytoplankton response to SI was greater than in MLI, despite less stratification; this highlights the complicated interaction between three-dimensional flows that occur during instabilities and the reduction of turbulent diffusivity caused by surface forcing necessary in light limitation. Therefore, in evaluating our light-limiting scenario, as a rule of thumb restratification should lead to an increase of primary production due to longer residence times of phytoplankton at any depth above the pycnocline; the magnitude of the phytoplankton response will be mediated by the specifics of the instability's flow.

It should also be noted that phytoplankton growth will be concentrated near the surface. As already elucidated, the decrease in vertical displacements due to restratification will allow for net growth in the face of ongoing turbulent motions in the

convective layer near the surface. Due to the exponential nature of light penetration in the ocean, the greatest growth is biased towards the surface; phytoplankton deeper down may not benefit as much from SI's restratification. Additionally, restratification implies a frontal-scale vertical redistribution of phytoplankton; at a given depth across the front, phytoplankton in more dense (less buoyant) water are subducted, and phytoplankton in less dense (more buoyant) water are upwelled. By this reasoning, phytoplankton starting in the less dense water will be selected for the fastest growth by moving closer to the light exposure at the surface. Since we did not impose a horizontal biological gradient and are focusing on the short-term effects of SI upon a planktonic ecosystem, we will not speculate on longer-term repercussions of a SI-induced bloom involving other ecological mechanisms; these include shading of deeper phytoplankton by surface phytoplankton, the increased microzooplankton encounter rates with phytoplankton prey following reduced turbulent convection that may be important in the "Dilution-Recoupling Hypothesis" [*Boss and Behrenfeld*, 2010], etc.

4.3.4 Biological effects during nutrient limitation

The impact of SI upon a nutrient-limited ecosystem will depend upon the relative locations of the nutrient gradient and pycnocline. The initial along-isopycnal motions and subsequent mixing during SI seem to provide a potential mechanism of irreversible nutrient flux (Figure 4.5c). SI is a surface boundary layer phenomenon, and does not penetrate below the pycnocline. Without strong surface forcing, the mixed layer base is usually shallower than the base of the euphotic zone, which is collocated with the nutricline (region of rapid increase in inorganic nutrients) in most of the ocean [*Omand*

and Mahadevan, 2013]. As a result, in most conditions, SI would occur at a strong front and restratify water within the mixed layer without generating a significant nutrient input. Generally speaking, therefore, without a coincident pycnocline and nutricline, little new production is expected in the phytoplankton community during SI.

Additional biological impacts of SI in this context will be in the vertical and horizontal redistribution of phytoplankton communities that exist within the affected surface layer. Similar to the light-limited scenario, restratification implies subduction of dense water (negative buoyancy flux) and upwelling of less dense water (positive buoyancy flux). In the nutrient-limited scenario, then, the phytoplankton in the denser water of the instability region, possibly in the euphotic zone, will move deeper within the mixed layer, while some plankton in the less-dense oligotrophic waters will move closer to the surface. At the same time, the motions of SI will tend to homogenize the depth-stratified phytoplankton community along isopycnals in the euphotic zone before restratifying the local water column, thus acting as a biological disturbance (Figure 4.5c). Subsequently, the community will create new gradients, dependent upon light, local nutrient availability and microbial regeneration, and grazing pressure through the water column.

4.3.5 Forced SI

Once SI is exhausted, there is the potential for surface buoyancy forcing (heat flux) or down-front winds to create the conditions for continued SI. This is termed *forced symmetric instability*. The general idea is that surface forcing such as down-front winds can strengthen the horizontal density gradients necessary for SI to develop. *Thomas et al.*

[2013] stress that with horizontal density gradients marginally stable to SI, a relatively weak wind can cause forced SI by increasing the horizontal density gradients. If indeed forced SI is present, there is the potential for extensive, protracted mixing [*D'Asaro et al.*, 2011]. Within this context, our two biological scenarios can be modified as follows.

For light-limited phytoplankton, the re-initiation of SI and associated mixing should somewhat remove the beneficial effects of stratification induced by SI in the first place. However, remembering that it is the turbulent motions that cause the light-limitation, the actual phytoplankton response will depend on the balance between restratification and the mixing by forced SI and the surface forcing. Though forced SI might increase light limitation relative to unforced SI, the presence of forced SI will still reduce light-limitation compared to a scenario without any SI.

In our nutrient-limited scenario, forced SI's protracted mixing could cause the mixed layer to penetrate into the nutricline, driving a nutrient flux into the euphotic zone. With the right preconditions (i.e., sufficient horizontal buoyancy gradients, $\phi \sim \phi_{cr}$), surface forcing can bring about a disproportionate amount of turbulence through SI. Numerical simulations of forced SI have not been carried out for nutrient-limited phytoplankton scenarios, so whether the enhanced mixing could lead to extensive entrainment of nutrients from deeper in the water column is difficult to assess at present, limiting our ability to diagnose the net change in phytoplankton.

4.3.6 Strain and SI

Fronts in the ocean are often created by larger-scale mesoscale forcing, such as in the waters between two eddies whose boundaries create enhanced horizontal gradients. A

strengthening of the horizontal buoyancy gradient, known as *frontogenesis*, implies an increase of the horizontal density gradients and an acceleration of the geostrophic current, which is essentially a strain (a gradient of the velocity in the direction it is going). During frontogenesis, other second-order movements occur, known as ageostrophic secondary circulations (ASC), which act to both restore geostrophic balance and conserve vorticity [*Hoskins et al.*, 1978]. There are implied vertical dynamics in this adjustment process, though their general impact upon phytoplankton has been discussed elsewhere [*Nagai et al.*, 2009; *Klein and Lapeyre*, 2009]. For the sake of our exposition, we consider the impact of the frontogenesis-induced strain upon SI.

This section mostly communicates the results of *Thomas* [2012]. In this study, among other analyses Thomas explores the implications of including strain in a front unstable to SI. The overall conclusion from the analyses is that strain alters the growth rates of the perturbations responsible for SI, essentially damping them despite the increase in ambient vertical shear of the geostrophic current (SI's energy source). Indeed, SI will not grow at all given large strain rates. Additionally, the development of the secondary Kelvin-Helmholtz instabilities associated with SI are delayed and damped.

In light of the results of *Thomas* [2012], we find that SI is not only an instability that requires strong horizontal gradients, but that the processes that realistically create these gradients will tend to dampen SI's growth. Despite the damping effect of strain, evidence for SI's occurrence has been found in western boundary currents; these results emphasize that a strong front is required for SI, and that several other considerations and preconditions have to be met in order for it to occur.

4.4. Mixed Layer Instability

Mixed Layer Instability (MLI) occurs over longer timescales O(days) than SI, but results in greater restratification. Similarly, MLI occurs over larger spatial scales than SI, and can thus influence a larger area of the ocean (1-10's km). In essence, MLI is a type of baroclinic instability, the same mechanism known for eddy genesis. However, the motions associated with MLI are smaller in spatial scale than traditional baroclinic instability, and, as implied by the name, are localized to the upper ocean's mixed layer. These motions have been known for decades (e.g., *Stone*, [1966]; *Blumen*, [1980]; *Nakamura*, [1988]). *Boccaletti et al.* [2007], though, recently pointed out the role of MLI in restratification.

4.4.1 Conditions for MLI

Within the context of our metric ϕ, the specific scenario to pinpoint for MLI is somewhat ambiguous. Theoretically, any horizontal buoyancy gradient in geostrophic balance can produce baroclinic instability ($\phi < 0$) [*Haine and Marshall*, 1998]. However, for vanishing horizontal buoyancy gradients ($\phi \rightarrow 0$), the horizontal distance a perturbation parcel must move becomes large. The phenomenological scale separation between traditional baroclinic instability and MLI has to be treated on a case-by-case basis, and is ultimately a somewhat subjective distinction. Therefore, for our investigation we will follow the pragmatic classification suggested by *Boccaletti et al.* [2007]:

1. For ϕ <-90°, the water column is gravitationally unstable (heavy water over light water), and may also undergo SI. Convection and restratification brings the local ϕ to a more positive number.
2. For -90° < ϕ < ϕ_{cr} ~ -45°, the water column can undergo SI. This restratification occurs more quickly under SI than MLI and leads to a more positive value of ϕ.
3. For ϕ_{cr} ~ -45° < ϕ < 0°, baroclinic instability (MLI) is possible and will be the fastest-growing instability.

This is not to say that MLI does not happen for ϕ < -45°. It is possible, but SI will grow faster, moving ϕ back toward ~ -45°, allowing MLI to dominate [*Stone*, 1970]. This process is not necessarily unidirectional. *Thomas et al.* [2013] suggest that interacting baroclinic waves, such as dipole mesoscale eddies, could lead to local enhancements of horizontal buoyancy gradients, and trigger SI in its own right. This process, frontogenesis, introduces a large-scale strain that influences the instability conditions for SI, as was considered in Section 3.6.

In our current application, we highlight in figure 4.2 the maximum growth rate of MLI that is coincident with the ecologically relevant timescales of phytoplankton generation time, here placed at 0.7 d^{-1} and taken from a scenario motivated by a front in the California Current [*Barth*, 1994].

4.4.2 What happens during MLI

MLI is a mini-baroclinic instability relegated to the mixed layer, with a release of the potential energy present in the horizontal buoyancy gradient, leading to nonlinear

eddy formation (though for evidence that submesoscale baroclinic instabilities also extract kinetic energy, see *Grooms*, [2015]). The wave that grows into MLI oscillates in the same direction as the horizontal buoyancy gradient (Figures 4.7a, 4.8a). As these oscillations grow, water from the light side of the front moves over dense water and to a higher vertical position (local positive buoyancy flux), while the dense water generally moves to the light side of the front but at a deeper depth (local negative buoyancy flux), flattening the isopycnals and isolines of buoyancy (Figures 4.7c and 4.8b). The eddies that form are initially small relative to mesoscale eddies, with the minimum length scale, ~O(1-2) km, determined by the first internal Rossby radius of the water column, expressed as

$$L_R = \frac{NH}{f} \tag{14}$$

where H is the depth of the mixed layer. For example, with our light-limited N of 10^{-3} s^{-1}, f of 10^{-4} s^{-1}, and assuming an H of ~100 m, gives us an L_R of 1 km.

4.4.3 Biological effects during light limitation

The restratification by MLI is more intense than SI, though it takes days to develop (compare the changes in isopycnal distributions between Figures 4.5c and 4.7c). As previously noted, *Taylor and Ferrari* [2011b] show that MLI plays a role in alleviating light limitation, though in their simulations the changes due to SI resulted in a greater phytoplankton response.

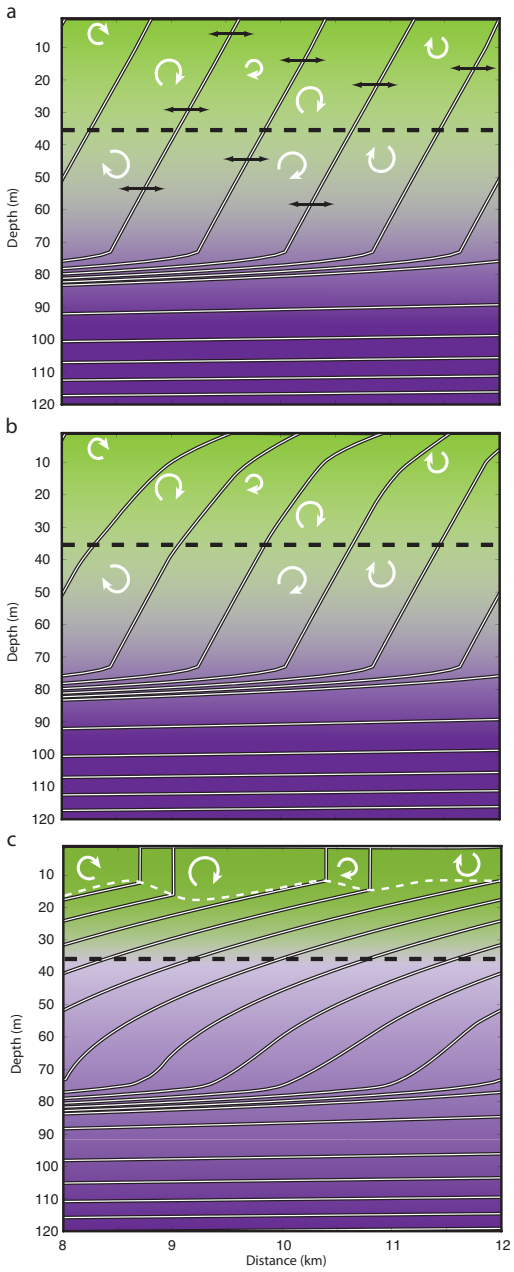

Figure 4.7. MLI for light-limitation. (a) Baroclinic wave perturbations (black arrows) move water in the direction of the horizontal buoyancy gradient. (b) MLI begins to restratify water in the mixed layer. (c) MLI has significantly restratified the mixed layer below the convective layer, resulting in less turbulent overturns. This reduces light limitation, and stimulates phytoplankton growth.

The way in which MLI restratifies a water column has a qualitatively different spatial structure than SI. Motions due to SI are cross-front, and the structure of these

motions are similar going along-front. After SI, the front's isopycnals will be relaxed away from the vertical direction, but the front will still look like a front. By contrast, the baroclinic motions due to MLI lead to cross-front motions that vary along-front. These along-front variations are the baroclinic wave, qualitatively similar to the mesoscale meandering of currents such as the Gulf Stream before forming eddies. Therefore, in order to resolve MLI, a three-dimensional perspective is necessary (for a visual reference, refer to Figure 4.8 in *Boccaletti et al.*, [2007]). The restratification due to MLI results in a shoaled mixed layer depth in the wintertime scenario much faster than what would be predicted by one-dimensional mixed layer models [*Haine and Marshall*, 1998], and as a result alleviates light limitation. Once created, the submesoscale eddies spawned by MLI begin to interact and grow in space and time, eventually becoming mesoscale in what is termed an inverse energy cascade [*Rhines*, 1979]. These familiar mesoscale eddies, too, have been implicated in alleviating light limitation [*Mahadevan et al.*, 2012], suggesting that MLI's impact upon light-limited assemblages may be long-lived. In summary, MLI, like SI, leads to restratification in the water column and enhanced primary production near the surface in light-limited phytoplankton. Unlike SI, the magnitude and spatial extent of the restratification is larger, takes longer to develop, and has a three-dimensional geometry reflected in the eddies it creates.

4.4.4 Biological effects for nutrient limitation

MLI, as previously mentioned, is restricted to motions in the mixed layer. As a result, all buoyancy fluxes will reorganize water above the pycnocline, and more importantly for our discussion, the nutricline. Whereas larger-scale baroclinic instability

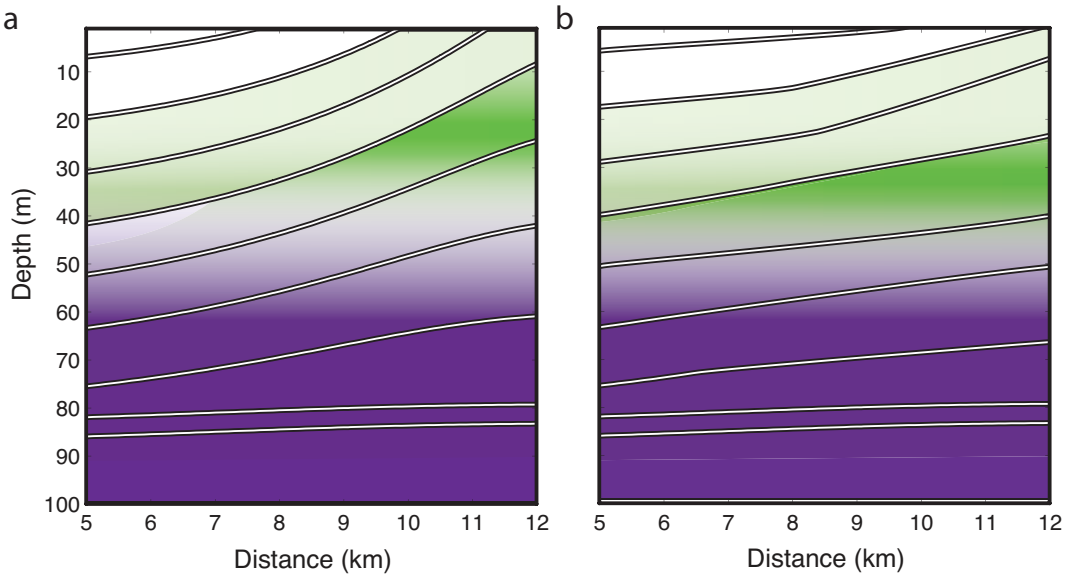

Figure 4.8. Impact of MLI upon the nutrient-limited ecosystem. (a) Starting with a density distribution with $\phi \sim$ -45, MLI restratifies the water column (b) with little impact upon nutrients at depth, while subducting (upwelling) phytoplankton on the eutrophic (oligotrophic) side of the front.

will influence isopycnals including those below the mixed layer, MLI will not do so initially. Therefore, for a nutrient-limited phytoplankton assemblage, MLI is unlikely to provide a nutrient flux from below; instead, it will vertically stratify the phytoplankton assemblages present at the front (Figure 4.8b). This point, whether a front vertically traverses the pycnocline (and the associated nutricline below it), has general consequences for biogeochemical cycling; a shallow front constrained to the mixed layer (as considered here) will not vertically flux nutrients to the surface, but a deep front will [*Ramachandran et al.* 2014]. Again, the restratification will tend to subduct (upwell) phytoplankton from the more (less) dense side of the front, affecting the light conditions for phytoplankton in the eutrophic (oligotrophic) assemblages (Figure 4.8c). However, once eddies are spawned by MLI, as previously mentioned in section 4.3 they will begin to undergo an inverse energy cascade [*Rhines*, 1979], creating larger and larger eddies

that will begin to interact with water below the pycnocline, providing nutrient flux for stimulating production [*Lévy et al.*, 2001; *Spall et al.*, 2000]. Additionally, the surface eddies created in this process will tend to be cyclonic, in part due to inertial instability curbing the formation of strong anticyclonic flows [*Munk et al.*, 2000]. Cyclonic eddies, with a characteristic doming of isopycnals, have been shown to contribute to localized nutrient inputs and lead to new production at the base of the euphotic zone [*McGillicuddy et al.*, 1998; *McGillicuddy et al.*, 2007; *Chenillat et al.*, 2015]. In summary, though MLI will initially provide negligible nutrient flux, subsequent dynamics initiated by MLI could ultimately contribute to new phytoplankton production.

4.5. Conclusions

A few core concepts are useful in understanding the dynamics and implications of both SI and MLI. First, the strength of a front can be quantified by measuring its horizontal and vertical density gradients, allowing the calculation of ϕ. The strength of the front is indicative of which instability will dominate and how it will influence subsequent dynamics. Second, both SI and MLI occur due to the potential and kinetic energy present within fronts. As the horizontal buoyancy gradients in a front strengthen, both the concentration of potential energy available for release, and the kinetic energy associated with the geostrophic current increase; SI primarily extracts its energy from the kinetic energy of the current, while MLI mostly feeds on the potential energy of the horizontal density gradients. Third, both instabilities have the net effect of restratifying a front, but do it in different ways:

- SI creates secondary instabilities that lead to stratified turbulence, mixing water from both the surface and below the instability. The resulting stratification can alleviate light limitation, and for nutrient-limited assemblages a nutrient flux may occur if the nutricline is shallow enough.
- MLI, on the other hand, restratifies the water column without mixing or initially repositioning water below the mixed layer. Therefore, MLI will have a greater biological impact in light-limited scenarios, reducing turbulence via restratification but without generating a nutrient flux from below. As eddies spawned by MLI grow and become mesoscale in nature, however, their nonlinear interactions can produce nutrient inputs and lead to new biological production [*Lévy et al.*, 2001; *Klein and Lapeyre*, 2009].

In order for new biological hypotheses to be correctly created, tested, critiqued, and added to by a broader group of scientists, the physical properties of submesoscale instabilities need to be communicated. The increasing interest in the role of submesoscale features in modulating biological productivity will lead to new insights regarding the magnitude and spatial and temporal scales of vertical fluxes of biogeochemical tracers between the surface and deep ocean. Incorporating submesoscale dynamics into modeling and field studies is starting to yield new and interesting conclusions.

Acknowledgements

Chapter 4, in part, is currently being prepared for submission for publication of the material. de Verneil, A. and Franks, P.J.S. Submesoscale Mixed Layer and Symmetric Instabilities: Physical Dynamics and Biological Responses. Progress in Oceanography. The dissertation author was the primary investigator and author of this paper.

References

Barth, J., 1994. Short-wavelength instabilities on coastal jets and fronts. Journal of Geophysical Research 99 (C8), 16,095-16,115, doi: 10.1029/94JC01270

Boss, E., Behrenfeld, M., 2010. In situ evaluation of the initiation of the North Atlantic phytoplankton bloom. Geophysical Research Letters 37, L18603, doi:10.1029/2010GL044174

Blumen, W.A., 1980. On the evolution and interaction of short and long baroclinic waves of the Eady type. Journal of Atmospheric Science 37, 1984-1983, doi: 10.1175/1520-0469(1980)037<1984:OTEAIO>2.0.CO;2.

Boccaletti, G., Ferrari, R., Fox-Kemper, B., 2007. Mixed Layer Instabilities and Restratification. Journal of Physical Oceanography 37, 2228-2250, doi: 10.1175/JPO3101.1.

Capet, X., McWilliams, J.C., Molemaker, M.J., Shchepetkin, A.F., 2008. Mesoscale to submesoscale transition in the California Current System. Part II: Frontal processes. Journal of Physical Oceanography, 38(1), 44-64. doi: 10.1175/2007JPO3671.1

Chenillat, F., Franks, P.J.S., Rivière, P., Capet, X., Grima, N., Blanke, B., 2015. Plankton dynamics in a cyclonic eddy in the Southern California Current System. Journal of Geophysical Research: Oceans. In review.

D'Asaro, E., Lee, C., Rainville, L., Harcourt, R., Thomas, L., 2011. Enhanced Turbulence and Energy Dissipation at Ocean Fronts. Science 332 (6027), 318-322, doi: 10.1126/science.1201515.

D'Ovidio, F., De Monte, S., Alvain, S., Dandonneau, Y., Lévy, M., 2010. Fluid dynamical niches of phytoplankton types. Proceedings of the National Academy of Sciences 107 (43), 18366-18370, doi: 10.1073/pnas.1004620107.

Emanuel, K.A., 1988. Observational Evidence of Slantwise Convective Adjustment. Monthly Weather Review 116, 1805-1816, doi: 10.1175/1520-0493(1988)116<1805:OEOSCA>2.0.CO;2.

Franks, P.J.S. and Franks, S.E.R., 2009. Mix it Up, Mix it Down: Intriguing Implications of Ocean Layering. Oceanography 22(1), 228-233, doi: 10.5670/oceanog.2009.27

Franks, P.J.S., 1992. Phytoplankton blooms at fronts: patterns, scales and physical forcing mechanisms. Reviews in Aquatic Sciences 6,121-137.

Franks, P.J.S., 2014. Has Sverdrup's critical depth hypothesis been tested? Mixed layers vs. turbulent layers. ICES Journal of Marine Science fsu175, doi: 10.1093/icesjms/fsu175

Gill, A.E., Green, J.S.A., Simmons, A.J., 1974. Energy partition in the large-scale ocean circulation and the production of mid-ocean eddies. Deep Sea Research and Oceanographic Abstracts 21(7), 499-528, doi:10.1016/0011-7471(74)90010-2

Grooms, I., 2015. Submesoscale baroclinic instability in the balance equations. *Journal of Fluid Mechanics* 762, 256-272, Doi: 10.1017/jfm.2014.657

Haine, T.W.N., and Marshall, J., 1998. Gravitational, symmetric, and baroclinic instability of the ocean mixed layer. Journal of Physical Oceanography 28(4), 634-658, doi: 10.1175/1520-0485(1998)028<0634:GSABIO>2.0.CO;2

Hoskins, B.J., 1974. The role of potential vorticity in symmetric stability and instability. Quarterly Journal of the Royal Meteorological Society 100(425), 480-482, doi: 10.1002/qj.49710042520

Hoskins, B.J., Draghici, I., Davies, H.C., 1978. A new look at the ω-equation. Quarterly Journal of the Royal Meteorological Society 104(439), 31-38, doi: 10.1002/qj.49710443903

Huisman, J.E.F., van Oostveen, P., Weissing, F.J., 1999. Critical depth and critical turbulence: two different mechanisms for the development of phytoplankton blooms. Limnology and Oceanography 44(7), 1781-1787, doi: 10.4319/lo.1999.44.7.1781

Jiao, Y., Dewar, W.K., 2015. The Energetics of Centrifugal Instability. Journal of Physical Oceanography 45, 1554-1573, doi: 10.1175/JPO-D-14-0064.1

Klein, P., and Lapeyre, G., 2009. The oceanic vertical pump induced by mesoscale and submesoscale turbulence. Annual Review of Marine Science 1, 351-375, doi: 10.1146/annurev.marine.010908.163704

Kloosterziel, R.C., Carnevale, G.F., Orlandi, P., 2007. Inertial instability in rotating and stratified fluids: barotropic vortices. Journal of Fluid Mechanics 583, 379-412, doi: 10.1017/S0022112007006325

Landry, M.R., Ohman, M.D., Goericke, R., Stukel, M.R., and Tsyrklevich, K., 2009. Lagrangian studies of phytoplankton growth and grazing relationships in a coastal upwelling ecosystem off Southern California. Progress in Oceanography 83(1), 208-216, doi: 10.1016/j.pocean.2009.07.026

Lévy, M., Klein, P., Treguier, A-M., 2001. Impact of submesoscale physics on production and subduction of phytoplankton in an oligotrophic regime. Journal of marine research 59(4), 535-565, doi: 10.1357/002224001762842181

Lévy, M., Doroteaciro, I., Resplandy, L., Klein, P., Gurvan, M., Tréguier, A-M., Masson, S., Takahashi, K., 2012. Large-scale impacts of submesoscale dynamics on phytoplankton: Local and remote effects. Ocean Modelling 43, 77-93. 10.1016/j.ocemod.2011.12.003

Mahadevan, A., Tandon, A., 2006. An analysis of mechanisms for submesoscale vertical motion at ocean fronts. Ocean Modelling 14(3), 241-256, doi: 10.1016/j.ocemod.2006.05.006

Mahadevan, A., D'Asaro, E., Lee, C., Perry, M.J., 2012. Eddy-driven stratification initiates North Atlantic spring phytoplankton blooms. Science 337(6090), 54-58, doi: 10.1126/science.1218740

McGillicuddy, D.J., Robinson, A.R., Siegel, D.A., Jannasch, H.W., Johnson, R., Dickey, T.D., McNeil, J., Michasel, A.F., Knap, A.H., 1998. Influence of mesoscale eddies on new production in the Sargasso Sea. Nature 394(6690), 263-266, doi: 10.1038/28367

McGillicuddy, D.J., Anderson, L.A., Bates, N.R., Bibby, T., Buesseler, K.O., Carlson, C.A., Davis, C.S., et al. 2007. Eddy/wind interactions stimulate extraordinary mid-ocean plankton blooms. Science 316(5827), 1021-1026, doi: 10.1126/science.1136256

Molemaker, M. J., McWilliams, J.C., Dewar, W.K., 2015. Submesoscale instability and generation of mesoscale anticyclones near a separation of the California Undercurrent. Journal of Physical Oceanography 45(3), 613-629, doi: 10.1175/JPO-D-13-0225.1

Moloney, C.L., Field, J.G., 1991. The size-based dynamics of plankton food webs. I. A simulation model of carbon and nitrogen flows. Journal of Plankton Research 13(5), 1003-1038, doi: 10.1093/plankt/13.5.1003

Munk, W., Armi, L., Fischer, K., Zachariasen, F., 2000. Spirals on the sea. Proceedings of the Royal Society of London A: Mathematical, Physical and Engineering Sciences 456(1997) 1217-1280, doi: 10.1098/rspa.2000.0560

Nagai, T., Tandon, A., Yamazaki, H., Doubell, M.J., 2009. Evidence of enhanced turbulence dissipation in the frontogenetic Kuroshio Front thermocline. Geophysical Research Letters 36(12), doi: 10.1029/2009GL038832

Nakamura, N., 1988. Scale selection of baroclinic instability – Effects of stratification and nongeostrophy. Journa of the atmospheric sciences 45(21), 3253-3268, doi: 10.1175/1520-0469(1988)045<3253:SSOBIO>2.0.CO;2

Niiler, P.P., Maximenko, N.A., McWilliams, J.C., 2003. Dynamically balanced absolute sea level of the global ocean derived from near-surface velocity observations. Geophysical Research Letters 30(22), 2164, doi:10.1029/2003GL018628

Olson, D.B., 1991. Rings in the ocean. Annual Review of Earth and Planetary Science, 19, 283-311, doi: 10.1146/annurev.ea.19.050191.001435

Olson, D.B., Hitchcock, G.L., Mariano, A.J., Ashjian, C.J., Peng, G., Nero, R.W., Podestra, G.P., 1994. Life on the edge: marine life and fronts. Oceanography 7(2), 52-60, doi: 10.5670/oceanog.1994.03

Olson, D.B., 2002. Biophysical dynamics of ocean fronts. Pages 187-218, in Robinson, A.R., et al. (eds). Biological-physical interactions in the sea (The Sea, 12). John Wiley and Son, New York. ISBN: 9780674017429

Omand, M.M., Mahadevan, A., 2013. Large-scale alignment of oceanic nitrate and density. Journal of Geophysical Research: Oceans 118, 5322-5332, doi: 10.1002/jgrc.20379

Omand, M.M., Mahadevan, A., 2015. The shape of the oceanic nitracline. Biogeosciences 12, 3273-3287, doi: 10.5194/bg-12-3273-2015

Owen, R.W., 1981. Fronts and eddies in the sea: mechanisms, interactions and biological effects. Pages 197-233, in Longhurst, A.R., editor. Analysis of marine ecosystems. Academic Press, New York. ISBN-13: 978-0124555600

Perruche, C., Rivière, P., Lapeyre, G., Carton, X., Pondaven, P., 2011. Effects of surface quasi-geostrophic turbulence on phytoplankton competition and coexistence. Journal of Marine Research 69(1), 105-135. Doi: 10.1357/002224011798147606

Ramachandran, S., Tandon, A., Mahadevan, A., 2014. Enhancement in vertical fluxes at a front by mesoscale-submesoscale coupling. Journal of Geophysical Research: Oceans 119, 8495-8511, doi: 10.1002/2014JC010211

Rhines, P.B., 1979. Geostrophic turbulence. Annual Review of Fluid Mechanics, 11(1), 401-441, doi: 10.1146/annurev.fl.11.010179.002153

Schultz, D.M., Schumacher, P.N., 1999. The use and misuse of conditional symmetric instability. Monthly Weather Review, 127(12), 2709-2732, doi: 10.1175/1520-0493(1999)127<2709:TUAMOC>2.0.CO;2

Sournia, A., 1994. Pelagic biogeography and fronts. Progress in Oceanography 34(2), 109-120, doi: 10.1016/0079-6611(94)90004-3

Spall, S.A., Richards, K.J., 2000. A numerical model of mesoscale frontal instabilities and plankton dynamics – I. Model formulation and initial experiments. Deep Sea Research Part I: Oceanographic Research Papers 47(7), 1261-1301, doi: 10.1016/S0967-0637(99)00081-3

Stammer, D., 1997. Global characteristics of ocean variability estimated from regional TOPEX/POSEIDON altimeter measurements. Journal of Physical Oceanography 27(8), 1743-1769, doi: 10.1175/1520-0485(1997)027<1743:GCOOVE>2.0.CO;2

Stommel, H., Veronis, G., 1980. Barotropic response to cooling. Journal of Geophysical Research: Oceans (1978-2012) 85(C11), 6661-6666, doi: 10.1029/JC085iC11p06661

Stone, P.H., 1966. On non-geostrophic baroclinic stability. Journal of the Atmospheric Sciences 23(4), 390-400, doi: 10.1175/1520-0469(1966)023<0390:ONGBS>2.0.CO;2

Stone, P.H., 1970. On non-geostrophic baroclinic stability: Part II. Journal of the Atmospheric Sciences 27(5), 721-726. Doi: 10.1175/1520-0469(1970)027<0721:ONGBSP>2.0.CO;2

Taylor, J.R., Ferrari, R., 2009. On the equilibration of a symmetrically unstable front via a secondary shear instability. Journal of Fluid Mechanics 622, 103-113, doi: 10.1017/S0022112008005272

Taylor, J.R., Ferrari, R., 2010. Buoyancy and wind-driven convection at mixed layer density fronts. Journal of Physical Oceanography 40(6), 1222-1242, doi: 10.1175/2010JPO4365.1

Taylor, J.R., Ferrari, R., 2011a. Shutdown of turbulent convection as a new criterion for the onset of spring phytoplankton blooms. Limnology and Oceanography 56(6), 2293-2307, doi: 10.4319/lo.2011.56.6.2293

Taylor, J.R., Ferrari, R., 2011b. Ocean fronts trigger high latitude phytoplankton blooms. Geophysical Research Letters 38(23), doi: 10.1029/2011GL049312

Thomas, L.N., Tandon, A., Mahadevan, A., 2008. Submesoscale processes and dynamics. In Ocean Modeling in an Eddying Regime, Eds. Hecht, M., Hasume, H., Geophysical Monograph Series 177 17-38, American Geophysical Union, Washington D.C.

Thomas, L.N., 2012. On the effects of frontogenetic strain on symmetric instability and inertia-gravity waves. Journal of Fluid Mechanics 711, 620-640, doi: 10.1017/jfm.2012.416

Thomas, L.N., Taylor, J.R. Ferrari, R., Joyce, T.M., 2013. Symmetric instability in the Gulf Stream. Deep Sea Research Part II: Topical Studies in Oceanography 91, 91-110, doi: 10.1016/j.dsr2.2013.02.025

Wang, P., Özgökmen, T.M., 2015. How do hydrodynamic instabilities affect 3D transport in geophysical votices? Ocean Modelling 87, 48-66, doi: 10.1016/j.ocemod.2015.01.002

Wyrtki, K., Magaard, L., Hager, J., 1976. Eddy energy in the oceans. Journal of Geophysical Research 81(15), 2641-2646, doi: 10.1029/JC081i015p02641

Yoder, J.A., Ackleson, S.G., Barber, R.T., Flament, P., Balch, W.M., 1990. A line in the sea. Nature 371(6499), 689-692, doi: 10.1038/371689a0

Chapter 5.

Conclusions

The overarching theme of my dissertation explores the flows at surface ocean fronts, and how these motions affect the phytoplankton community present within it. In each chapter, I utilize different aspects of the flow at a front to determine, respectively, the observed evolution of a biological tracer, the fine-scale distribution of phytoplankton embedded within a front, and the likely evolution of phytoplankton communities due to submesoscale instabilities. In the course of exploring these various aspects of phytoplankton dynamics, several findings and general observations emerge that both inform the conceptual picture of phytoplankton at fronts and delineate directions for future research. In this conclusion, I review the consequences of my thesis research within the context of previous studies and propose future areas of study that will build upon the work in this thesis.

Measuring biological rates in the ocean

Considering the short timescales of the biological sources and sinks of phytoplankton (e.g., growth, mortality, grazing, viral lysing, sinking of biomass), simply measuring the bulk concentrations of phytoplankton and zooplankton biomass, pigment concentrations, nutrient concentration, etc. is not very informative. In order to truly diagnose the state of an ecosystem, the rate of change in these bulk properties is required. Currently, growth and microzooplankton grazing is popularly determined by the dilution

method [*Landry and Hassett*, 1982]. Predation due to larger metazoans such as copepods is often estimated by gut fluorescence [*Mackas and Bohrer*, 1976; *Kiørboe et al.*, 1985] . Natural phytoplankton mortality is usually considered small relative to microzooplankton grazing, and grazing due to some metazoan taxa remains unresolved. Possible viral lysis is largely ignored, though it may be significant [*Fuhrman*, 1999]. Together, these rate measurements are patched together to estimate the cycling of biomass from phytoplankton to the immediately adjacent trophic levels. Theoretically, once all these fluxes have been accounted for, the temporal evolution of the bulk variables can be explained. Following this procedure, an investigator will be able to then diagnose the dynamics of the planktonic ecosystem.

The major limitation in this approach is the work required to arrive at these values, and the fact that these observations account for only one spatial and temporal location. The motion of this location with time is partially addressed by the use of quasi-Lagrangian platforms that follow the flow [*Landry et al.*, 2009]. By definition, however, this platform will not reflect a single location at all depths in a front, since the flow has a vertical shear; near the surface, the float will travel slower than the true water parcel, while at depth the float will move faster. The hope is that the biological assemblage embedded within the front is undergoing similar dynamics at spatial scales large relative to the misfit in float location and true Lagrangian position.

In Chapter 2, I developed a pseudo-Lagrangian method that incorporated the three-dimensional velocity field to advect chlorophyll-*a* fluorescence and calculate its net rate of change. While there are clearly assumptions and limitations to this method, its main advantages are: first, its accounting for depth-variable currents, second, the sheer

number of independent observations of rates, and third, its estimation of error. As mentioned in Chapter 2, the calculated rate does not resolve the rates of change due to the various mechanisms influencing chlorophyll-*a*. Hence, the traditional methods of measuring rates are still vital for future studies of planktonic ecosystems. However, here I suggest future applications of the pseudo-Lagrangian method as a complementary measurement to better understand phytoplankton dynamics.

First, the pseudo-Lagrangian method can be used to account for variability in spatial distribution and calculate correct rates of these features. While in Chapter 2 I utilized objectively mapped chlorophyll-*a* fluorescence to calculate net rates of change, the findings in Chapter 3 from the MVP surveys shows that this distribution is, in fact, inaccurate and smoothes over the fine structure in salinity and fluorescence that was present in E-Front. To resolve this problem in the future, one should instead use the tracer data in each profile directly, rather than the objectively mapped value. If fine-scale structure does indeed exist, and patches are contiguous between survey lines, their locations can perhaps be used as an independent validation technique in determining the error in the pseudo-Lagrangian position (i.e., the advection scheme should advect a patch to the same patch downstream). Interpolation should not be used in finding the final tracer value. Instead, the pseudo-Lagrangian method should proceed as follows: first, use the velocity field to identify data locations that are connected by streamlines, then second, find the timescale necessary for advection from one observation to the next. If the timescale necessary for advection is much different than the observation timescale (e.g., water would take 10 days to advect but the ship sampled these positions 2 days apart), then perhaps a threshold time difference may be used to only use data sampled close to

the advection timescale. The determination of error, in this case, would change so that now errors in the two tracer values only reflect observational noise. The Δt error, which was not previously considered, will now represent the advection error. Most likely, error from the fluorometer would be quite small in relation to error in advection time. Using the altered scheme, the pseudo-Lagrangian method should provide rates of change for even small-scale features; it is difficult to imagine how rates within these patches would be resolved experimentally without concentrated effort to sample and follow one specific feature.

Application of the pseudo-Lagrangian approach in Chapter 2 found that rate measurements require a downstream sampling strategy. Optimization of a survey to be Lagrangian is currently more art than precise science, though methods are being developed to increase the Lagrangian nature of ship sampling [*Doglioli et al.*, 2013]. Additionally, the method requires a well-characterized flow field, likely restricting its application to fronts and eddies – regions where geostrophic currents are the major components of flow. This limitation should not pose too much of a problem; evidence suggests that biogeochemical fluxes due to fronts and eddies are the unresolved gaps in global nutrient cycling budgets, and the need to investigate phytoplankton dynamics at these features is not likely to wane [*Thomas et al.*, 2008; *Oschlies*, 2002].

The extension of the pseudo-Lagrangian method to other tracers holds perhaps the most promise. Use of fluorescence data from different pigments can lead to rough taxon-resolved rates [*Chekalyuk and Hafez*, 2008]. Transmissometer data can track the evolution of particulate concentrations, and perhaps capture sinking of distinct features. Use of an oxygen sensor could be an additional biological constraint; oxygen should only

increase with active photosynthesis, and its relative change should track the balance of primary productivity and respiration. The oxygen rate can then be compared to the change in fluorescence. One would expect these rates to be different due to variable carbon to chlorophyll-*a* ratios (C:Chl-*a*) [*Geider et al*., 1997], as well as respiration due to heterotrophs. However, greater efforts are being made to parameterize phytoplankton models that incorporate C:Chl-*a* variability, as well as grazing functional response [*Li et al.*, 2010; 2011]. Comparing the modeled rate predictions with changes of oxygen and fluorescence could provide an additional test of the model's applicability, apart from more validation from traditional measurements. Finally, with the projected increased impact of ocean acidification upon the physiology of certain phytoplankton taxa, spatially resolved rates in changes of pH with recently developed sampling platforms [*Martz et al.*, 2010] could potentially identify the spatiotemporal variability of this physiological stress. In light of the potential applications, Chapter 2 hopefully marks only the first foray into rates resolved by Lagrangian survey data.

Recognizing fine-scale variability

In Chapter 3, I identified fine-scale layers of water with high salinity and chlorophyll-*a* fluorescence, and subsequently diagnosed their presence due to a cross-frontal shear flow that acted upon pre-existing gradients. While biological oceanographers have come to expect fine-scale variability and patchiness in plankton distributions, it is necessary to not only correctly identify patches, but also the mechanisms of their formation. Most studies focusing on the ageostrophic circulations at fronts highlight the vertical velocities that either provide nutrients through upwelling or

subduct phytoplankton biomass away from the euphotic zone. At E-Front, I found that the horizontal velocities associated with these cells are also important in altering horizontal gradients and converting them into vertical gradients.

The shearing of layers at a front has several biological consequences. First, the phytoplankton patch within a layer now extends over a greater horizontal area. The initial patch, immediately following frontogenesis, has a small horizontal extent. However, via this shear mechanism, plankton at depth are now no longer located beneath plankton at the surface. For layers with high concentrations of phytoplankton, this may result in a release of light limitation via self-shading [*Shigesada and Okubo*, 1981]. The increased areal coverage of a phytoplankton patch also impacts grazers. While microzooplankton embedded in a fluid will not be affected, vertical diel migrators such as copepods now have a greater probability of intercepting a patch of concentrated prey biomass. Additionally, the vertical layering of phytoplankton patches will alter the behavior of migrators. If grazers encounter one layer at depth, they may neglect to continue closer to the surface and graze upon a second, shallower layer [*Leising and Franks*, 2002]. Therefore, in effect, the cross-frontal shear may help select which populations of phytoplankton face grazing pressure.

Diagnosing short-term frontal dynamics

Possibly one of the most difficult aspects of sampling fronts is the short timescales over which they can evolve. Even demonstrating the biological impact of ageostrophic vertical velocities in nutrient delivery is difficult using field data, despite their clear role in modeling studies [*Oguz et al.*, 2014]. Due to the complex flows that

may develop at a front, a pragmatic guide to the possible dynamics, and potential biological impacts, is necessary.

In Chapter 4, I reviewed two submesoscale instabilities: symmetric instability (SI) and mixed layer instability (MLI). Both instabilities act to restratify the water column, relaxing the horizontal gradient of density. These two instabilities differ, however, in the prerequisite conditions for their existence and the motions they induce. A useful metric, ϕ, is used from *Thomas et al.* [2013] that diagnoses the strength of a front, and whether it will undergo SI. While most fronts in the ocean will have near-zero values of ϕ, it nevertheless may be a useful tool to characterize the strength of a front more generally. Since ϕ's definition stems from density distributions, it should be relatively simple to calculate, and may be a useful diagnostic for investigators at sea to determine whether one kind of submesoscale instability is favored over another.

Recapping the dynamics discussed in Chapter 4, SI leads to stratified turbulence, mixing waters with opposing Ertel potential vorticity (EPV) and quickly exhausts itself without continuing forcing, typically evolving over a day or two. For light-limited phytoplankton, the net restratification can relieve light limitation and allow for phytoplankton growth near the surface. In nutrient-limited phytoplankton, the impact of SI will depend on whether the base of the mixed layer at the front is sufficiently deep to upwell inorganic nutrients from depth. MLI, on the other hand, acts like a small-scale version of baroclinic instability, spawning eddies that rearrange isopycnals and quickly restratify the water column over the slightly longer timescale of ~10 days. For light-limited phytoplankton, like SI, MLI can lead to phytoplankton growth at the surface. For nutrient-limited phytoplankton, MLI is unlikely to stimulate phytoplankton production

until the eddies it creates begin to grow and interact with the pycnocline, whereupon isopycnal nutrient fluxes may occur and stimulate phytoplankton growth, similar to *Lévy et al.* [2001] and *Spall and Richards* [2000].

Since both instabilities occur over days to weeks, they will be difficult to observe *in situ*. Therefore, the hope is that with a larger community of ocean-going oceanographers equipped with the knowledge of how to diagnose these instabilities, and what biological dynamics to expect from their evolution, observational evidence for these submesoscale instabilities can be obtained – perhaps even unintentionally thanks to rapid recognition of their presence.

As a final note, even the physical modeling of these instabilities is far from exhaustive, and inclusion of biological models in these frontal dynamics is needed to either corroborate or reject the hypotheses laid out in this review. Therefore, more work is needed in this field of research to elucidate the possible large-scale impacts of these small-scale features in the ocean.

References

Anderson, G.C., 1969. Subsurface chlorophyll maximum in the northeast Pacific Ocean. Limnology and Oceanography 14 (3), 386-391.

Chekalyuk, A. M., Hafez, M.A., 2008. Advanced laser fluorometry of natural aquatic environments. *Limnology and Oceanography: Methods*, *6*, 591. doi: 10.4319/lom.2008.6.591.

Doglioli, A. M., Nencioli, F., Petrenko, A.A., Rougier, G., Fuda, J.L., Grima, N., 2013. A software package and hardware tools for in situ experiments in a Lagrangian reference frame. *Journal of Atmospheric and Oceanic Technology*, *30*(8), 1940-1950. doi: 10.1175/JTECH-D-12-00183.1.

Fuhrman, J.A., 1999. Marine viruses and their biogeochemical and ecological effects. Nature 399 (6736), 541-548.

Geider, R.J., MacIntry, H.L., Kana, T.M., 1997. Dynamic model of phytoplankton growth and acclimation: responses of the balanced growth rate and the chlorophyll a: carbon ratio to light, nutrient-limitation and temperature. Oceanographic Literature Reivew 9 (44), 974.

Kiørboe, T., Møhlenberg, F., Riisgård, H.U., 1985. In situ feeding rates of planktonic copepods: a comparison of four methods. *J. exp. mar. Biol. Ecol., 88,* 67-81. doi: 10.1016/0022-0981(85)90202-3.

Landry, M.R., Hassett, R.P., 1982. Estimating the Grazing Impact of Marine Micro-zooplankton. *Marine Biology, 67,* 283-288. doi: 10.1007/BF00397668.

Landry, M. R., Ohman, M.D., Goericke, R., Stukel, M.R., Tsyrklevich, K., 2009. Lagrangian studies of phytoplankton growth and grazing relationships in a coastal upwelling ecosystem off Southern California. *Progress in Oceanography*, *83*(1), 208-216. doi: 10.1016/j.pocean.2009.07.026.

Leising, A.W., Franks, P.J.S., 2002. Does Acartia clausi (Copepoda: Calanoida) use an area-restricted search foraging strategy to find food? Hydrobiologia, 480 (1-3), 193-207.

Lévy, M., Klein, P., Tréguier, A.M., 2001. Impact of sub-mesoscale physics on production and subduction of phytoplankton in an oligotrophic regime. Journal of Marine Research 59, 535-565.

Li, Q. P., Franks, P.J.S., Landry, M.R., Goericke, R., Taylor, A.G., 2010. Modeling phytoplankton growth rates and chlorophyll to carbon ratios in California coastal and pelagic ecosystems. *Journal of Geophysical Research: Biogeosciences (2005–2012)*, *115*(G4). doi: 10.1029/2009jg001111.

Li, Q. P., Franks, P.J.S., Landry, M.R., 2011. Microzooplankton grazing dynamics:-parameterizing grazing models with dilution experiment data from the California Current Ecosystem. *Marine Ecology Progress Series*, *438*, 59-69. doi: 10.3354/meps09320.

Mackas, D., Bohrer, R., 1976. Fluorescence analysis of zooplankton gut contents and an investigation of diel feeding patterns. *J. exp. mar. Biol. Ecol., 25,* 77-85. doi: 10.1016/0022-0981(76)90077-0.

Martz, T. R., J.G. Connery, Johnson, K.S., 2010. Testing the Honeywell Durafet® for seawater pH applications. *Limnol Oceanogr Methods*, *8*, 172-184. doi: 10.4319/lom.2010.8.172.

Oschlies, A., 2002. Can eddies make ocean deserts bloom? Global Biogeochemical Cycles 16 (4), 53-1.

Oguz, T., Macias, D., Garcia-Lafuente, J., Pascual, A., Tintoré, J., 2014. Fueling Plankton production by a meandering frontal jet: A case study for the Alboran Sea (Western Mediterranean). PLoS ONE 9 (11): e111482.

Shigesada, N., Okubo, A., 1981. Analysis of the self-shading effect on algal vertical distribution in natural waters. Journal of Mathematical Biology 12 (3), 311-326.

Spall, S.A., Richards, K.J., 2000. A numerical model of mesoscale frontal instabilities and plankton dynamics – I. Model formulation and initial experiments. Deep Sea Research Part I: Oceanographic Research Papers 47(7), 1261-1301, doi: 10.1016/S0967-0637(99)00081-3

Thomas, L.N., Tandon, A., Mahadevan, A., 2008. Submesoscale processes and dynamics. In Ocean Modeling in an Eddying Regime, Eds. Hecht, M., Hasume, H., Geophysical Monograph Series 177 17-38, American Geophysical Union, Washington D.C.

Thomas, L.N., Taylor, J.R. Ferrari, R., Joyce, T.M., 2013. Symmetric instability in the Gulf Stream. Deep Sea Research Part II: Topical Studies in Oceanography 91, 91-110, doi: 10.1016/j.dsr2.2013.02.025

Wiebe, P.H., Morton, A.W., Bradley, A.M., Backus, R.H., Craddock, J.E., Barber, V., Cowles, T.J., Flierl, G.R., 1985. New development in the MOCNESS, an apparatus for sampling zooplankton and micronekton. Marine Biology 87 (3), 313-323.